QA: QA

Model
Administrative Change Notice

Complete only applicable items.

1. Document Number:	MDL-NBS-HS-000006	2. Revision:	03/AD 01	3. ACN:	01
4. Title:	UZ Flow Models and Submodels				
5. No. of Pages Attached	86 91	1-7-08			

6. Approvals:		
Preparer:	Yu-Shu Wu Print name and sign	12/14/07 Date
Checker:	Shaoping Chu Print name and sign	12/18/2007 Date
QCS/Lead Lab QA Reviewer:	Charles Beach Print name and sign	12-18-07 Date
Independent Technical Reviewer:	Susan Altman Print name and sign	12/18/2007 Date
Responsible Manager: 1-7-08	M. KATHRYN KNOWLES ~~Geoff Freeze~~ Print name and sign	1/7/08 Date

7. Affected Pages	8. Description of Change:
ix	Listing for Section 7.4.1: Changed listing to "Validation of the UZ Model for the Scenario of the 10th-Percentile Infiltration Map" to reflect corresponding section heading change (see entry for p. 7-9 below).
xiv	Listing for Figure 6.4-3: Changed listing to "Comparison of Simulated (solid line) and Observed (solid dots) Gas Pressures at Borehole UZ-7a during the First 30-day Period" to reflect corresponding figure caption change (see entry for p. 6-62 below). Listing for Figure 6.6-2: Changed listing to "Simulated Percolation Fluxes at the Repository Horizon under the Monsoon, 10th Percentile Infiltration Scenario" to reflect corresponding figure caption change (see entry for p. 6-83 below).
xvi	Listing for Figure 7.5-1: Changed listing to "Simulated Solute Travel Time of the Matrix Pore Water with Three-dimensional Simulation for Borehole UZ-1 Compared to the Measured ^{14}C Age" to reflect corresponding figure caption change (see entry for p. 7-16 below). Listing for Figure 7.5-2: Changed listing to "Simulated Solute Travel Time of the Matrix Pore Water with Three-dimensional Simulation for Borehole SD-12 Compared to the Measured ^{14}C Age" to reflect corresponding figure caption change (see entry for p. 7-17 below).
xvii	Listing for Figure 7.5-3: Changed listing to "Simulated Solute Travel Time of the Matrix Pore Water with One-dimensional Simulation for Borehole UZ-1 Compared to the Measured ^{14}C Age" to reflect corresponding figure caption change (see entry for p. 7-19 below). Listing for Figure 7.5-4: Changed listing to "Simulated Solute Travel Time of the Matrix Pore Water with One-dimensional Simulation for Borehole SD-12 Compared to the Measured ^{14}C Age" to reflect corresponding figure caption change (see entry for p 7-20 below).

1. Document Number: MDL-NBS-HS-000006 **2. Revision**: 03 **3. ACN**: 01

4. Title: UZ Flow Models and Submodels

xxi	Listing for Table 6.4-3: Changed listing to “Modifications to Fracture Permeability Resulting from Three-Dimensional Calibration (30% scenario)” to reflect corresponding figure caption change (see entry for p. 6-61 below). Listing for Table 6.5-2: Changed listing to “Present-Day Chloride Recharge Fluxes and Precipitation, Runon, and Runoff Rates for Different Scenarios (Averaged over Model Domain)” to reflect corresponding figure caption change (see entry for p. 6-67 below). Listing for Table 6.6-1: Changed listing to “Comparison of the Water Flux through Matrix, Fractures of Non-fault Zones, and Faults as a Percentage of the Total Flux over the Entire Model Domain and within the Repository Footprint at the TCw/PTn Interface for the 16 Flow Fields” to reflect corresponding table caption change (see entry for p. 6-91 below). Changed the word “water” to “Water” (Listing for Tables 6.2-2 through 6.2-5).
xxii	Listing for Table 6.6-2: Changed listing to “Comparison of the Water Flux through Matrix, Fractures of Non-fault Zones, and Faults as a Percentage of the Total Flux over the Entire Model Domain and within the Repository Footprint at the Repository Level for the 16 Flow Fields” to reflect corresponding table caption change (see entry for p. 6-92 below). Listing for Table 6.6-3: Changed listing to “Comparison of the Water Flux through Matrix, Fractures of Non-fault Zones, and Faults as a Percentage of the Total Flux over the Entire Model Domain and within the Repository Footprint at the Water Table for the 16 Flow Fields” to reflect corresponding table caption change (see entry for p. 6-93 below).
5-1	Last paragraph, first sentence: Changed “past Modern Interglacial Climate” to “present-day interglacial climate”.
6-2	Last sentence: Inserted “(CFu)” after “Crater Flat undifferentiated unit”.
6-3 and 6-4	Table 6.1-1: In the “Lithostratigraphic Nomenclature” column, merged blank cells under the cells listing the “Tptrn” and “Tptpln” units; in the “UZ Model Grid Unit/Layer” column, merged blank cells under “tcw12”, “ptn22”, “ptn24”, “tsw31,” and “tsw33”; in “Hydrogeologic Unit” column, merged blank cells under “CUL, CW”, “BT4”, “BT3”, “TC”, and “TUL”; carried last row on page 6-3 onto page 6-4 to merge blank cells under “pp2” and “PP2 (devitrified)”.
6-7	Last paragraph, 4th line from bottom: Inserted “model,” before “the gas flow model”.
6-8	First paragraph: Inserted “the” before “fracture and matrix continuum” in two instances. Last sentence: Changed “Darcy’s velocity” to “Darcy velocity”.
6-10	Second paragraph, 7th line: Replaced “becoming earlier” with “occurring sooner”.
6-11	Second paragraph, 7th line from bottom: Split sentence into two separate sentences by deleting “even though” and ending the first sentence after “lateral diversions”. Second sentence now begins with “The degree or scale . . .”.
6-15	Figure 6.1-2: Replaced figure to correct misspelling of “infiltration” in figure heading.
6-16	Figure 6.1-3: Replaced figure to correct misspelling of “infiltration” in figure heading.
6-17	Figure 6.1-4: Replaced figure to correct misspelling of “infiltration” in figure heading.
6-18	Last paragraph, 4th line from bottom: Changed “flow field” to “flow fields”.
6-19	Table 6.1-3: Changed “percentiles” to “percentile” in 4th row under “Scenario” column.
6-20	Figure 6.1-5: Replaced figure to correct misspelling of “infiltration” in figure heading.
6-22	Third paragraph, 3rd line: Deleted “of” before “the important iterative processes”. Last paragraph, 2nd sentence: Added missing “*Analysis of*” to title of DIRS 170038.

1. Document Number: MDL-NBS-HS-000006 **2. Revision**: 03 **3. ACN**: 01

4. Title: UZ Flow Models and Submodels

6-25	First paragraph, 6th line: Deleted the phrase “and it is even thicker to the north of the repository”.
6-26	First paragraph, 4th line: Inserted “a” before “reasonable”.
6-29 and 6-30	Tables 6.2-2 through 6.2-5: Capitalized the “w” in “water” in the table captions.
6-33	Last paragraph, 5th line from bottom: Changed “source” to “sources”. Last paragraph, 3rd and 4th lines from bottom: Revised “Only in situ measurement of water potentials are used among the water-potential data” to read “Only in situ measurements of water-potential are used in this analysis.” Also, deleted “simulation” before “results”. Last paragraph, 3rd line: Changed “other seven” to “seven other”.
6-34	Last paragraph: add to the end of the paragraph: “In Figures 6.2-2 and 6.2-3, saturations simulated for the lower portion of the TSw with the pd_90 scenario are lower than the rest of the lower infiltration scenarios. This is because the simulations for each infiltration scenario use different parameter sets. Nevertheless, simulation results are still within ranges of measured saturation data.”
6-38	Table 6.2-8, last column, 1st row, 5th line: Changed “averaged” to “average”.
6-43	First paragraph, lines 9 through 11: Deleted sentence “As discussed in Section 6.3.4, percolation flux (or infiltration rate) is one of the factors that control thermal conditions.”
6-45	Last paragraph, 2nd and 4th lines: Inserted “a” before “multiple-year temperature data set” and inserted “the” before “model bottom temperature boundary”.
6-46	First paragraph, 2nd line: Replaced “against” with “when compared to”. Second paragraph, 3rd line: Changed “condition” to “conditions”. Fourth paragraph, 4th line: Inserted “the” before “top”.
6-48	Second paragraph, line 22: Changed the range of percolation flux from “−3.4 to 7.3 mm/yr” to “3.4 to 7.3 mm/yr”. Second paragraph, line 24: Changed “are” to “have”.
6-57	Table 6.4-1, NOTE: Changed “30-day data” to “30 days of the data set” in two places. Second paragraph from bottom, 1st line: Inserted “the” before “given infiltration scenario”. Last paragraph, 1st line: Changed “cells” to “cell”.
6-58	Last paragraph of Section 6.4.1, 2nd sentence: Replaced “to” with “on”. Sentence now reads: “The impact of liquid-phase flow on the gas flow system …”. First paragraph of Section 6.4.2, third sentence: Changed “tsw” to “TSw” and deleted “nearby”.
6-59	Figure 6.4-1: Replaced figure to correct the UZ model grid unit labeling on the curves (e.g., “tcw 12”, “tsw 32”, etc.) and to change the units on the y-axis label from “KPa” to “kPa”. Figure 6.4-1, NOTE: Added “The hydrogeologic units shown on the figure (e.g., tcw12) are determined from a comparison of the borehole location and measurement depth with the spatial data for the hydrogeolgic units available from the UZ model grid.”
6-60	Figure 6.4-2: Replaced figure to correct the UZ model grid unit labeling on the curves (e.g., “tcw 12”, “tsw 35”, etc.) and to change the units on the y-axis label from “KPa” to “kPa”. Figure 6.4-2, NOTE: Added “The hydrogeologic units shown on the figure (e.g., tcw12) are determined from a comparison of the borehole location and measurement depth with the spatial data for the hydrogeolgic units available from the UZ model grid.”

1. Document Number: MDL-NBS-HS-000006 **2. Revision**: 03 **3. ACN**: 01

4. Title: UZ Flow Models and Submodels

6-61	First paragraph, 12th line, deleted “nearby”. Table 6.4-3: Changed table caption to “Modifications to Fracture Permeability Resulting from Three- Dimensional Calibration (30% scenario)”.
6-62	Figure 6.4-3: Replaced figure to correct the UZ model grid unit labeling on the curves (e.g., “tcw 12”, “tsw 32”, etc.) and to change the units on the y-axis label from “KPa” to “kPa”. Also changed “UZ-71” to “UZ-7a” in figure caption. Figure 6.4-3, NOTE: Added “The hydrogeologic units shown on the figure (e.g., tcw12) are determined from a comparison of the borehole location and measurement depth with the spatial data for the hydrogeolgic units available from the UZ model grid.”
6-63	Figure 6.4-4: Replaced figure to correct the UZ model grid unit labeling on the curves (e.g., “tcw 12”, “tsw 35”, etc.) and to change the units on the y-axis label from “KPa” to “kPa”. Figure 6.4-4, NOTE: Added “The hydrogeologic units shown on the figure (e.g., tcw12) are determined from a comparison of the borehole location and measurement depth with the spatial data for the hydrogeolgic units available from the UZ model grid.”
6-64	First paragraph, 2nd line: Changed “case” to “cases”. Second paragraph, 4th line: Changed “This” to “These”. Third paragraph, 4th line: Added closing parenthesis after “(compared to the modern climate” and inserted “before present” after second “10,000 years”. Last paragraph: Combined the second and third sentences.
6-65	Table 6.5-1: Added missing note “H” after entry for DTN: LAJF831222AQ98.011 in 3rd row of 2nd column (entry for SD-9).
6-66	First paragraph: Changed “28,000 years” to “21,000 years” and the sentence to: “The present-day mean infiltration rate estimated from the chloride data is approximately 5 mm/yr, and the glacial maximum infiltration rate at 21,000 years ago was about 28 mm/yr” Third paragraph, 1st line: Changed “particulate” to “particulates”. Last paragraph, 3rd line: Inserted “the” before “TOUGH2”.
6-67	Table 6.5-2: Changed caption to ““Present-Day Chloride Recharge Fluxes and Precipitation, Runon, and Runoff Rates for Different Scenarios (Averaged over Model Domain)”. Last paragraph, 10th line: Deleted “in” before “part”. Last paragraph, 8th line from bottom: Deleted “this” before “variation”. Last paragraph, 3rd line from bottom: Inserted “and” before “applied”.
6-83	Figure 6.6-2: Removed superscripting from “th” in “10th” in caption. Figure caption now reads: “Simulated Percolation Fluxes at the Repository Horizon under the Monsoon, 10th Percentile Infiltration Scenario”.

1. Document Number: MDL-NBS-HS-000006 **2. Revision**: 03 **3. ACN**: 01

4. Title: UZ Flow Models and Submodels

6-91	First paragraph, 1st line: Changed “6.6-22” to “6.6-2”. First paragraph, 6th and 7th lines: Changed “where as” to “whereas”. Second paragraph, 1st line: Deleted “A” and capitalized “statistical”. Second paragraph, 6th line: Inserted “(Table 6.6-3)” after “reaching 44% to 65% at the water table”. Table 6.6-1: Changed caption to “Comparison of the Water Flux through Matrix, Fractures of Non-fault Zones, and Faults as a Percentage of the Total Flux over the Entire Model Domain and within the Repository Footprint at the TCw/PTn Interface for the 16 Flow Fields”.
6-92	Table 6.6-2: Changed caption to “Comparison of the Water Flux through Matrix, Fractures of Non-fault Zones, and Faults as a Percentage of the Total Flux over the Entire Model Domain and within the Repository Footprint at the Repository Level for the 16 Flow Fields”. Table 6.6-2: Changed heading in 1st row, 2nd column to “Flux at Repository Horizon over Entire Model Domain (%)”.
6-93	Table 6.6-3: Changed caption to “Comparison of the Water Flux through Matrix, Fractures of Non-fault Zones, and Faults as a Percentage of the Total Flux over the Entire Model Domain and within the Repository Footprint at the Water Table for the 16 Flow Fields”. Table 6.6-3: Changed heading in 1st row, 2nd column to “Flux at Water Table over Entire Model Domain (%)”.
6-96	Last paragraph, 3rd line: Added missing period after first sentence.
6-97	First paragraph, 1st line: Inserted new sentence before 1st full sentence. New sentence reads: “Note that the conservative component is used to represent a radionuclide, which typically has a small diffusion coefficient due to heavy molecular weight and large size.” First paragraph, 4th and 5th lines: Placed parentheses around the diffusion coefficient ranges cited for both anions and cations.
6-99	Second paragraph: Changed “Tables 6.7-3 and 6.7-5” to “Table 6.7-3”.
6-110	First paragraph, 8th line: Changed “distribution” to “distributions”. Second paragraph, 4th line: Changed “tunnel horizontal tunnels ECRB and ESF,” to “horizontal tunnels, the ECRB and ESF,”. Second paragraph, 6th line: Changed “boreholes” to “borehole”.
6-114	Paragraph for third likelihood function: Added the following after Equation 6.8-4: “This is a pseudo-maximum likelihood function. It is similar to maximum likelihood in a way that in its formulation more observation data (either data points or data types) will accentuate the better simulations, which means greater reduction of uncertainty. This function can be an alternative when measurement errors are not available.” Paragraph for fourth likelihood function: Changed “location” to “locations” in 3rd line after Equation 6.8-5.
6-115	Third paragraph, 8th line: Inserted “the” before “contribution”. Third paragraph, 10th line: Inserted “the” before “likelihood”.
6-117	Last paragraph: Replaced first three sentences with “Figure 6.8-2 shows the final likelihood of each infiltration map. Four bars represent the four infiltration maps. The weights for each map using an individual likelihood value correspond to the y-axis value for that individual likelihood function times its prior weights.”

1. Document Number: MDL-NBS-HS-000006 **2. Revision**: 03 **3. ACN**: 01

4. Title: UZ Flow Models and Submodels

6-118	Figure 6.8-2: Replaced figure to make the plotting symbols visible in the shaded portions of the figure. Figure 6.8-2, NOTE: Placed figure note on separate line from DTN listing.
7-1	First paragraph, 9th line from bottom: Changed “include” to “includes”. Second bullet, 2nd line: Inserted “water” after “perched”.
7-2	Third bullet, 2nd line: Deleted “mineral”. Last bullet, 9th line: Deleted “again”.
7-3	First paragraph, 2nd line: Changed “wase” to “case”. Second paragraph, 4th line: Added two commas. Second paragraph, next to last line: Added “hydrologic,” before “temperature,”.
7-4	Second paragraph, last sentence: Replaced “model is” with “model’s”.
7-9	Heading for Section 7.4.1: Added a “th” after “10”. Heading now reads: “Validation of the UZ Model for the Scenario of the 10th-Percentile Infiltration Map”. Figure 7.4-1: Replaced figure to correct the UZ model grid unit labeling on the curves (e.g., “tcw 12”, “tsw 32”, etc.) and to change the units on the y-axis label from “KPa” to “kPa”. Figure 7.4-1, NOTE: Added “The hydrogeologic units shown on the figure (e.g., tcw12) are determined from a comparison of the borehole location and measurement depth with the spatial data for the hydrogeolgic units available from the UZ model grid.”
7-10	Figure 7.4-2: Replaced figure to correct the UZ model grid unit labeling on the curves (e.g., “tcw 12”, “tsw 35”, etc.) and to change the units on the y-axis label from “KPa” to “kPa”. Figure 7.4-2, NOTE: Added “The hydrogeologic units shown on the figure (e.g., tcw12) are determined from a comparison of the borehole location and measurement depth with the spatial data for the hydrogeolgic units available from the UZ model grid.”
7-11	Figure 7.4-3: Replaced figure to correct the UZ model grid unit labeling on the curves (e.g., “tcw 12”, “tsw 32”, etc.) and to change the units on the y-axis label from “KPa” to “kPa”. Figure 7.4-3, NOTE: Added “The hydrogeologic units shown on the figure (e.g., tcw12) are determined from a comparison of the borehole location and measurement depth with the spatial data for the hydrogeolgic units available from the UZ model grid.”
7-12	Figure 7.4-4: Replaced figure to correct the UZ model grid unit labeling on the curves (e.g., “tcw 12”, “tsw 35”, etc.) and to change the units on the y-axis label from “KPa” to “kPa”. Figure 7.4-4, NOTE: Added “The hydrogeologic units shown on the figure (e.g., tcw12) are determined from a comparison of the borehole location and measurement depth with the spatial data for the hydrogeolgic units available from the UZ model grid.”
7-14	Second paragraph, 3rd line form bottom: Inserted “because” before “the boreholes”.
7-15	First paragraph, 4th line: Uncapitalized the “b” in “Boreholes”.
7-16	Figure 7.5-1: Changed “UZ-1 Borehole” to “Borehole UZ-1” in figure caption.
7-17	Figure 7.5-2: Changed “SD-12 Borehole” to “Borehole SD-12” in figure caption.
7-18	Second paragraph, 5th line: Inserted “the” before “10th and 30th”.
7-19	Figure 7.5-3: Changed “UZ-1 Borehole” to “Borehole UZ-1” in figure caption.
7-20	Figure 7.5-4: Changed “SD-12 Borehole” to “Borehole SD-12” in figure caption.

1. Document Number: MDL-NBS-HS-000006 **2. Revision**: 03 **3. ACN**: 01

4. Title: UZ Flow Models and Submodels

7-25	Last paragraph, 4th line: Changed “but not to a small value as those measured in zeolitic rocks” to “but not as small a value as those measured in zeolitic rocks.”
7-29	First paragraph, 6th line from bottom: Changed “content have” to “content has”. Second paragraph, 5th line from bottom: Changed “is not possible” to “are not possible”.
7-30	Second paragraph, added “The comment paper contended that the calcite was formed by upwelling hydrothermal waters and that the original journal article considered a constant ambient geothermal gradient for the approximately 10 million-year period, rather than a higher gradient which has been inferred from fluid inclusions.” Following the first sentence. Third paragraph, last sentence: Changed “primary” to “primarily”. Last paragraph, 2nd line from top: Revised sentence to “Pore waters extracted from Yucca Mountain rock matrix collected from deep locations are close to equilibrium with respect to calcite (BSC 2004 [DIRS 169734], Section 7.7.1), . . .”.
7-31	Second paragraph, 6th line: Changed “solve” to “solves”.
7-32	First paragraph, 9th and 10th lines: Added “Table 7.7-1 describes three of the five units, each of which is further divided . . .”. First paragraph, 5th line from bottom: Inserted “values” after “permeability”.
7-43	Third paragraph, 2nd line: Deleted “the” before “Yucca Mountain”.
7-44	First paragraph, the last sentence changed to: “The new results are within the spread of the measured calcite abundances, and therefore the variable geothermal gradient did not change the conclusions of the first paper. Thus, the results with variable temperature boundary do not change the conclusions made above.”
7-47	Figure 7.8-3: Deleted the phrase “(called distance from collar)” in figure NOTE.
7-51	First paragraph, 6th line: Removed parenthesis after “fault”.
7-54	Second paragraph, 7th line from bottom: Inserted “so” before “simulated flow field”.
8-7	First paragraph, last sentence: Deleted “in the CHn unit”.
8-8	Third paragraph, last line: Changed “range of flow field generated” to “range of the flow fields generated”.
H-2	Second paragraph, 5th line: Changed “6.2.12” to “6.2.12[a]”.
H-12	Table H-2, 4th row of last column: Changed “Table 6.8-1” to “Table 6.8-1 of Section 6” and changed “Table 6.2-5” to “Table 6.2-5[a]”.

CONTENTS (Continued)

Page

FIGURES (Continued)

Page

FIGURES (Continued)

Page

FIGURES (Continued)

Page

TABLES

Page

TABLES (Continued)

Page

5. ASSUMPTIONS

Assumptions are listed in this section only if they are necessitated by lack of data in the development of the UZ flow model and its submodels. Several approximations and idealizations are used for model development, such as selection of hydrogeological conceptual models, use of numerical modeling approaches, and specification of model boundary conditions. These are discussed and justified as appropriate in Section 6. In particular, modeling idealizations and approximations used for specific modeling studies are appropriately discussed in Section 6.

This section presents the rationale and justification for assumptions, discusses whether further confirmation is needed, and references the sections in the report where these assumptions are used. The assumptions used in developing the UZ flow models and submodels are as follows:

1. In the UZ flow model, faults are assumed to be vertical or inclined 30 m wide zones, crossing the entire unsaturated zone thickness from the surface to the water table. This assumption is used for the three-dimensional UZ flow model (Sections 6.1, 6.2, 6.5, 6.6, and 6.7) and three-dimensional ambient thermal model (Sections 6.3 and 6.4).

   Basis: This assumption is consistent with the assumptions and approximations used in designing the three-dimensional UZ model grid (BSC 2004 [DIRS 169855]). Considering the large-scale averaging performed by the three-dimensional mountain-scale UZ model, in which horizontal grid spacings are typically on the order of 100 m, a 30 m width is compatible with a spatial discretization of 100 m lateral spacing in the adjacent, nonfault gridblocks. The impact of fault widths or cross-sectional areas on results of steady-state flow simulation in the unsaturated zone is equivalent to that of variation in fault permeability. The sensitivity modeling analysis (BSC 2005 [DIRS 174191]) showed that three-orders-of-magnitude variations in fault transmissivity had very small impact on UZ flow and tracer transport from the repository to the water table. Therefore, this assumption is considered adequate and requires no further confirmation.

2. In describing the top temperature boundary condition, the ambient thermal model (Section 6.3) assumes that the average surface temperature is a linear function of surface elevation. Therefore, the entire temperature ranges along the top model boundary can be determined using a linear equation whose coefficients are estimated using average annual temperature data measured from two boreholes.

   Basis: The surface temperature is controlled by the local atmosphere conditions, while variations in the mean atmospheric temperature are dependent primarily on elevation, which are handled as linear functions of elevation. Therefore, this assumption is considered reasonable and adequate, and requires no further confirmation.

3. In describing infiltration, the uncertainty distribution for the present-day interglacial climate is fully correlated with theuncertainty distribution for the future Monsoon Climate and the future Glacial Transition Climate.

- The possible flow diversion in the PTn
- The perched water zones and associated flow barriers
- The probable flow paths from the repository to the water table
- Tracer transport times and paths from the repository to the water table, and breakthrough curves and areas of tracers at the water table.

The UZ flow model described here provides a defensible and credible UZ model for evaluation of Yucca Mountain as an underground radioactive waste repository. Major activities accomplished in this revision include incorporation of updated net infiltration maps for present-day, monsoon, glacial transition, and post-10k-yr climates; updated model calibrated property sets; updated model calibration studies of three-dimensional UZ flow; evaluation of the effects of PTn and perched water; updated geochemical and geothermal conditions; updated estimates of tracer and radionuclide transport times; estimates of UZ flow weighting factors; and intensive model validation efforts.

Other activities have involved generating 16 three-dimensional flow fields (Sections 6.2 and 6.7) to evaluate the uncertainties and sensitivity of the UZ model relative to fracture and matrix parameters and infiltration rates of four climates over the mountain by using four sets of model parameters, and sixteen infiltration scenarios. A total of 16 flow fields have been submitted to the TDMS as output DTNs. The sixteen flow fields are provided for use in TSPA calculations of radionuclide transport through the unsaturated zone system, and for other activities such as drift seepage abstraction.

FEPs included through this report are discussed in Section 6.2.6 and in Table 6.2-8.

6.1 MODEL DESCRIPTION

The conceptual and numerical models used for the modeling studies are documented in this report as well as in *Conceptual Model and Numerical Approaches for Unsaturated Zone Flow and Transport* (BSC 2004 [DIRS 170035]). The conceptual and numerical models are presented in this section so that a complete discussion of the models can be made.

6.1.1 Geological Model and Numerical Grids

The geologic framework model (GFM2000) (DTN: MO0012MWDGFM02.002 [DIRS 153777]) is used for incorporating geological features into the UZ flow model and its submodels. The development and features of the three-dimensional model grids are documented in *Development of Numerical Grids for UZ Flow and Transport Modeling* (BSC 2004 [DIRS 169855]). Table 6.1-1 lists the geological units/layers for different hydrogeologic units and the associated UZ model numerical grid-layer information. These geological formations have been organized into layered hydrogeologic units based primarily on the degree of welding (Montazer and Wilson 1984 [DIRS 100161]). These are the Tiva Canyon welded hydrogeologic unit (TCw), the Paintbrush nonwelded hydrogeologic unit (PTn), the Topopah Spring welded unit (TSw), the Calico Hills nonwelded hydrogeologic unit (CHn), and the Crater Flat undifferentiated unit (CFu).

Table 6.1-1. GFM2000 Lithostratigraphy, UZ Model Layer, and Hydrogeological Unit Correlation Used in the UZ Flow Model and Submodels

Major Unit[a]	Lithostratigraphic Nomenclature[b]	UZ Model Grid Unit/Layer[c]	Hydrogeological Unit [d]
Tiva Canyon welded (TCw)	Tpcr	tcw11	CCR, CUC
	Tpcp	tcw12	CUL, CW
	TpcLD		
	Tpcpv3	tcw13	CMW
	Tpcpv2		
Paintbrush nonwelded (PTn)	Tpcpv1	ptn21	CNW
	Tpbt4	ptn22	BT4
	Tpy (Yucca)		
		ptn23	TPY
		ptn24	BT3
	Tpbt3		
	Tpp (Pah)	ptn25	TPP
	Tpbt2	ptn26	BT2
	Tptrv3		
	Tptrv2		
Topopah Spring welded (TSw)	Tptrv1	tsw31	TC
	Tptrn		
		tsw32	TR
	Tptrl, Tptf	tsw33	TUL
	Tptpul, RHHtop		
	Tptpmn	tsw34	TMN
	Tptpll	tsw35	TLL
	Tptpln	tsw36	TM2 (upper 2/3 of Tptpln)
		tsw37	TM1 (lower 1/3 of Tptpln)
	Tptpv3	tsw38	PV3
	Tptpv2	tsw39 (vit, zeo)	PV2
Calico Hills nonwelded (CHn)	Tptpv1	ch1 (vit, zeo)	BT1 or BT1*a* (altered)
	Tpbt1		
	Tac (Calico)	ch2 (vit, zeo)	CHV (vitric) or CHZ (zeolitic)
		ch3 (vit, zeo)	
		ch4 (vit, zeo)	
		ch5 (vit, zeo)	
	Tacbt (Calicobt)	ch6 (vit, zeo)	BT
	Tcpuv (Prowuv)	pp4	PP4 (zeolitic)
	Tcpuc (Prowuc)	pp3	PP3 (devitrified)

Table 6.1-1. GFM2000 Lithostratigraphy, UZ Model Layer, and Hydrogeological Unit Correlation Used in the UZ Flow Model and Submodels (Continued)

Major Unit[a]	Lithostratigraphic Nomenclature[b]	UZ Model Grid Unit/Layer[c]	Hydrogeological Unit [d]
Calico Hills nonwelded (CHn) (Continued)	Tcpmd (Prowmd)	pp2	PP2 (devitrified)
	Tcplc (Prowlc)		
	Tcplv (Prowlv)	pp1	PP1 (zeolitic)
	Tcpbt (Prowbt)		
	Tcbuv (Bullfroguv)		
Crater Flat undifferentiated (CFu)	Tcbuc (Bullfroguc)	bf3	BF3 (welded)
	Tcbmd (Bullfrogmd)		
	Tcblc (Bullfroglc)		
	Tcblv (Bullfroglv)	bf2	BF2 (nonwelded)
	Tcbbt (Bullfrogbt)		
	Tctuv (Tramuv)		
	Tctuc (Tramuc)	tr3	Not Available
	Tctmd (Trammd)		
	Tctlc (Tramlc)		
	Tctlv (Tramlv)	tr2	Not Available
	Tctbt (Trambt) and below		

Sources: [a]Montazer and Wilson 1984 [DIRS 100161]; [b]BSC 2004 [DIRS 170029]; [c]BSC 2004 [DIRS 169855]; [d]Flint 1998 [DIRS 100033].

NOTES: [c]Defined by the rock material type, represented by the code name, for grid layers or blocks belonging to the same rock unit. [d]Hydrogeologcal units or layers defined for the UZ model exclude alluvial covers. The top model boundary is at the ground surface of the mountain (or the tuff-alluvium contact in areas of significant alluvial covers).

UZ = unsaturated zone.

The three-dimensional UZ model domain, as well as the numerical grid for this study (DTN: LB03023DKMGRID.001 [DIRS 162354]), is shown in plan view in Figure 6.1-1**,** encompassing approximately 40 km^2 of the area over the mountain. The UZ model grid, shown in Figure 6.1-1, is referred to as the TSPA-LA grid. It is primarily designed for model calibration and simulations of three-dimensional flow fields used in TSPA-LA calculations. As shown in Figure 6.1-1, this three-dimensional model grid uses a refined mesh in the vicinity of the repository, located near the center of the model domain, covering the region from the Solitario Canyon fault to Ghost Dance fault in the west-east direction, and from borehole G-3 in the south to beyond Sever Wash fault in the north (SNL 2007 [DIRS 179466]). Also shown in Figure 6.1-1 are the locations of several boreholes used in model calibrations and analyses. The model domain is selected to focus on the study area of the repository and to investigate the effects of different infiltration scenarios and major faults on moisture flow around and below the repository. In the model grid, faults are represented in the model by vertical or inclined 30 –m wide zones (Section 5). The top model boundary is set at the ground surface or the tuff–alluvium interface; the bottom model boundary is set to the water table. The water table is set to the average water table elevation across the model domain, fully supported by borehole water table measurement data. The water table, which is the bottom boundary of the UZ model, is shown to be a relatively flat, stable surface in most of the model domain, increasing its elevation only in the north (BSC 2004 [DIRS 169855]). This rise has little effect on flow simulation results within

three-dimensional TSPA-LA flow fields. For gas flow simulation and ambient temperature calibration, the TOUGH2 V1.6 (2003 [DIRS 161491]) EOS3 module was used. Tracer transport and chloride studies were performed using the decoupled module of T2R3D V1.4 (1999 [DIRS 146654]) with flow fields generated by the EOS9 module. TOUGH2 V1.6 (2003 [DIRS 161491]) and T2R3D V1.4 (1999 [DIRS 146654]) were selected because they have been qualified and baselined for modeling flow and transport in heterogeneous fractured rock (e.g., Wu et al. (2002 [DIRS 160195]). These numerical codes were used for this work because they were qualified and baselined for use in this report, and they have the generalized capability of handling fractured rock with local and global fracture–matrix interaction, which was required for modeling studies of this report.

To model unsaturated flow and transport processes in the unsaturated zone system at Yucca Mountain, mathematical models or governing equations are needed to describe the physical processes quantitatively. The physical processes associated with flow and transport in porous media are governed by the fundamental conservation laws (i.e., conservation of mass, momentum, and energy), which govern the behavior of fluid flow, chemical migration, and heat transfer through unsaturated fractured porous media. The macroscopic continuum approach has been most commonly used in practical applications (Bear 1972 [DIRS 156269]). In this approach, the physical laws governing flow of several fluids, transport of multicomponents, and heat transfer in porous media are represented mathematically on the macroscopic level by a set of partial differential or integral equations. Fluid and heat flow and chemical-transport processes in fracture and matrix systems in the unsaturated zone are described using a macroscopic, dual-permeability continuum approach.

In addition to the conservation or continuity equations of mass and thermal energy in fracture and matrix systems, specific relationships or *mechanisms* are needed that describe how fluid flow, solute/tracer transport, and heat transfer occur in porous and fractured media. The following specific laws and constitutive relationships act as such mechanisms by governing local fluid flow, component transport, and heat-transfer processes in porous and fractured media:

1. The governing equation for describing isothermal, unsaturated liquid flow is the Richards equation (Richards 1931 [DIRS 104252]; Pruess et al. 1999 [DIRS 160778], Equation A-17, p. 146), based on the conservation of mass and Darcy's law (Bear 1972 [DIRS 156269]) with flux driven by gravity and capillary pressure gradient. The unsaturated flux is a product of the unsaturated hydraulic conductivity and the driving gradient. Hydraulic conductivity is proportional to effective permeability and fluid density, and inversely proportional to fluid viscosity. Rock and fluid properties can be treated as constants under isothermal conditions. The effective permeability (relative permeability times absolute permeability or saturated permeability) is related to water content (saturation times porosity) and capillary pressure, as described by the van Genuchten model (1980 [DIRS 100610]). The governing equations for unsaturated flow under isothermal conditions are given in Appendix A. Exceptions to the use of the Richards equation are the ambient temperature model, the gas flow model, and the calcite model, which use the two-phase (water and air, TOUGH2 EOS3 module) flow equation instead of Richards equation for the isothermal or nonisothermal water and airflow flow.

The UZ flow model and its submodels adopt the dual-continuum approach for modeling flow through fractures and the matrix. The Richards equation is applied to the fracture and matrix continuum for unsaturated flow under isothermal conditions. Fluid exchange between the fracture continuum and matrix continuum is the fracture–matrix interaction, which is simulated by the dual-permeability concept, and is further modified by an active fracture model (AFM) (Liu et al. 1998 [DIRS 105729]) in the UZ flow model.

The active fracture model (AFM) was developed within the context of the dual-continuum approach (Liu et al. 1998 [DIRS 105729]). It is based on the reasoning that, on account of fingering flow, only a portion of fractures in a connected, unsaturated fracture network contribute to liquid water flow, while other fractures are simply bypassed. The portion of the connected fractures that actively conduct water are called active fractures. Thus, the AFM uses a combination of a continuum approach and a simple filtering concept to model fracture flow. Inactive fractures are filtered out in modeling fracture–matrix interaction and flow in the fracture continuum.

Darcy's law (Appendix A) and the van Genuchten model can be generalized for multiphase flow under nonisothermal conditions. The governing equations for gas and liquid flow and heat flow are based on conservation of mass for fluid phases, and on conservation of energy for conductive and convective heat transfer processes, respectively. The full set of equations for nonisothermal, two-phase flow of gas and water in fractures and matrix are presented in a report by Pruess et al. (1999 [DIRS 160778], Appendix A).

In solving the governing equations (Appendix A), a number of known parameters are given as input to the UZ flow model. Some of those variables are treated as constants—for example, fluid viscosity under isothermal conditions. Others are provided as known parameters measured either in the laboratory or in field tests, and/or further calibrated. Examples of known parameters are rock density, porosity, and absolute permeability. Input parameters are further discussed in Section 6.1.5. In addition, boundary conditions are needed to solve governing equations (Section 6.1.3). The top boundary for the UZ flow model is subject to net infiltration from the land surface (Section 6.1.4). With these input parameters and boundary conditions, the solving of the full set of equations (Pruess et al. 1999 [DIRS 160778]) in the UZ flow model provides outputs for variables such as liquid saturation, phase pressures, capillary pressure, mass or percolation flux, and Darcy velocity, in addition to temperatures in the thermal model.

surfaces become minimal, and the one block matrix-fracture representation is expected to produce accurate solutions (Doughty 1999 [DIRS 135997]).

The utility and appropriateness of conceptual and numerical approach of dual-permeability for modeling several flow and transport processes has been discussed by Doughty (1999 [DIRS 135997]) through a one-dimensional column extracted from a three-dimensional UZ site-scale model of the unsaturated zone at Yucca Mountain, NV. Within the dual-continua models, the formulation for fracture–matrix (F–M) interface area can have a major effect on the hydrodynamic response to an infiltration pulse and tracer arrival at various horizons, with fracture responses occurring sooner as F–M interface area decreases. The number of matrix blocks also has a significant effect on response time, with the more accurate multi-matrix-gridblock models yielding slower fracture response times. For steady-state moisture flow, most of the numerical and conceptual models provide similar results for saturation and fracture flow profiles. When advection and diffusion play a significant role in tracer transport, the arrival time of tracer fronts is strongly dependent on the choice of F–M interface area formulation, as this area controls the magnitude of F–M diffusion in addition to F–M fluid flow. In general, as F–M interface area decreases, tracer travel time through the fractures decreases. For the cases studied, considering a uniform, relatively small infiltration rate, tracer front arrival time is somewhat sensitive to the choice of one or more matrix blocks, with dual-permeability models predicting earlier fracture arrival times for cases in which F–M interface area is reduced. For thermal loading, preliminary studies indicate that the dual-permeability model does capture all the significant physical processes, in which rapid fluid and heat flow occurs in the fractures before the matrix has a chance to equilibrate.

As applied in this report, the traditional dual-permeability concept is further modified using an AFM (Liu et al. 1998 [DIRS 105729]) to represent fingering effects of liquid flow through fractures and to limit flow into the matrix system. The active fracture concept has been evaluated in *Conceptual Model and Numerical Approaches for Unsaturated Zone Flow and Transport* (BSC 2004 [DIRS 170035]) and further sensitivity analyses are provided in Section 6.8. The dual-permeability conceptual model is used for describing fracture–matrix interaction with all geological units as well as faults.

As an alternative modeling approach, the discrete-fracture or “weeps” type model have extremely high uncertainties with respect to fracture distribution data within the mountain, as well as an extensive computational burden that cannot be solved currently or in the near future. On the other hand, the effective-continuum approach, although the most computationally efficient, may not capture important, nonequilibrium interaction in flow and transport between fractures and matrix in the unsaturated zone. Therefore, it may also not be appropriate for use in modeling UZ flow and transport at Yucca Mountain.

In model calibration of moisture flow and tracer transport, ambient, variably saturated flow in the unsaturated zone underlying Yucca Mountain is treated as an isothermal, steady-state flow system. This is considered to be a good approximation of the unsaturated zone below the PTn unit, because the relatively unfractured nonwelded PTn unit is expected to damp and homogenize downward-moving transient pulses arising from episodic surface infiltration events (Wu et al. 2000 [DIRS 154918]; Wu et al. 2002 [DIRS 161058]; Flint et al. 2001 [DIRS 164506]; Zhang et al. 2006 [DIRS 180273]). Additional analyses of PTn damping effects using the updated UZ model are presented in Section 6.9, to show the effectiveness of the PTn unit in redistributing

percolation flux for the units below. Therefore, estimated surface net infiltration rates may effectively be described as steady-state water recharge (Section 6.1.4).

In the development of the UZ flow model and its submodels over the past decade, the steady-state nature of the flow fields and the damping of transient pulses were evaluated in different studies. Wu et al. (1999 [DIRS 117161], p. 186) referred to the early work of Wang and Narasimhan (1985 [DIRS 108835]; 1993 [DIRS 106793], Figure 7.4.7), which suggested that effects of infiltration pulses at the surface are damped by the underlying tuff units, especially the PTn. The welded tuff of the repository horizon exhibited only small changes in saturations, pressures, and potentials from steady-state values in response to the transient pulses. Pan et al. (1997 [DIRS 164181]) investigated transient flow behavior for downward water flow through sloping layers in the vadose zone, with up-slope flow developed during heavy rain, likely enhancing the downward flow. Wu et al. (2002 [DIRS 161058], pp. 35-1 to 35-12) analyzed the capillary barrier capacities in unsaturated units and indicated that, on average, it took several thousands years for water to travel through the PTn. Wu et al. (2000 [DIRS 154918], 2002 [DIRS 161058]) and Flint et al. (2003 [DIRS 163967]) analyzed the implications of capillary barrier development in subunits of the PTn for lateral diversion of flow in the PTn. Along sloping layers, strong capillary barriers, if formed, will promote lateral diversions. The degree or scale of lateral diversion can be evaluated by: (1) comparative sensitivity studies, (2) detailed analysis of field data including geochemical evidences, and (3) long-term controlled field tests. A more recent study, conducted by Zhang et al. (2006 [DIRS 180273]) using three-dimensional and one-dimensional model results, shows that the PTn can attenuate episodic infiltration pulses significantly, most percolating water is damped by the subunits at the top of the PTn, and a small percentage of percolation flux is diverted into faults.

6.1.3 Model Boundary Conditions

The ground surface of the mountain (or the tuff-alluvium contact in areas of significant alluvial cover) is taken as the top model boundary; the water table is treated as the bottom model boundary. The top and bottom boundaries of the model are treated as Dirichlet-type conditions with specified constant, but spatially varying temperature and gas pressure. For flow simulations using the EOS9 module, only water pressure or saturation values are needed along the top and bottom model boundaries. Surface infiltration, as discussed below in Section 6.1.4, is applied using a source term in the fracture gridblocks within the second grid layer from the top. This method was adopted because the first layer is treated as a Dirichlet-type boundary, with constant pressure, saturation, and temperature to represent average atmospheric conditions at the mountain.

The water table is used as the bottom model boundary, a surface where the water pressure is a single, fixed value. Within the numerical models, only one set of model primary variables for solving Richards' equations is specified for the bottom boundary, equivalent to specifying a constant saturation. For gas and/or heat flow simulations, the bottom model boundary representing the water table is subject to fixed gas pressure, equal to the atmospheric pressure at that elevation (Sections 6.3.3 and 6.4.1). Lateral boundaries, as shown in Figure 6.1-1, are treated as no-flow (closed) boundaries, which allow flow to occur exclusively along the vertical plane. This treatment is reasonable for the eastern boundary, which is along or near the Bow Ridge fault, because high vertical permeability and lower capillary forces are expected within the faults (see fault properties estimated in *Calibrated Unsaturated Zone Properties* (SNL 2007

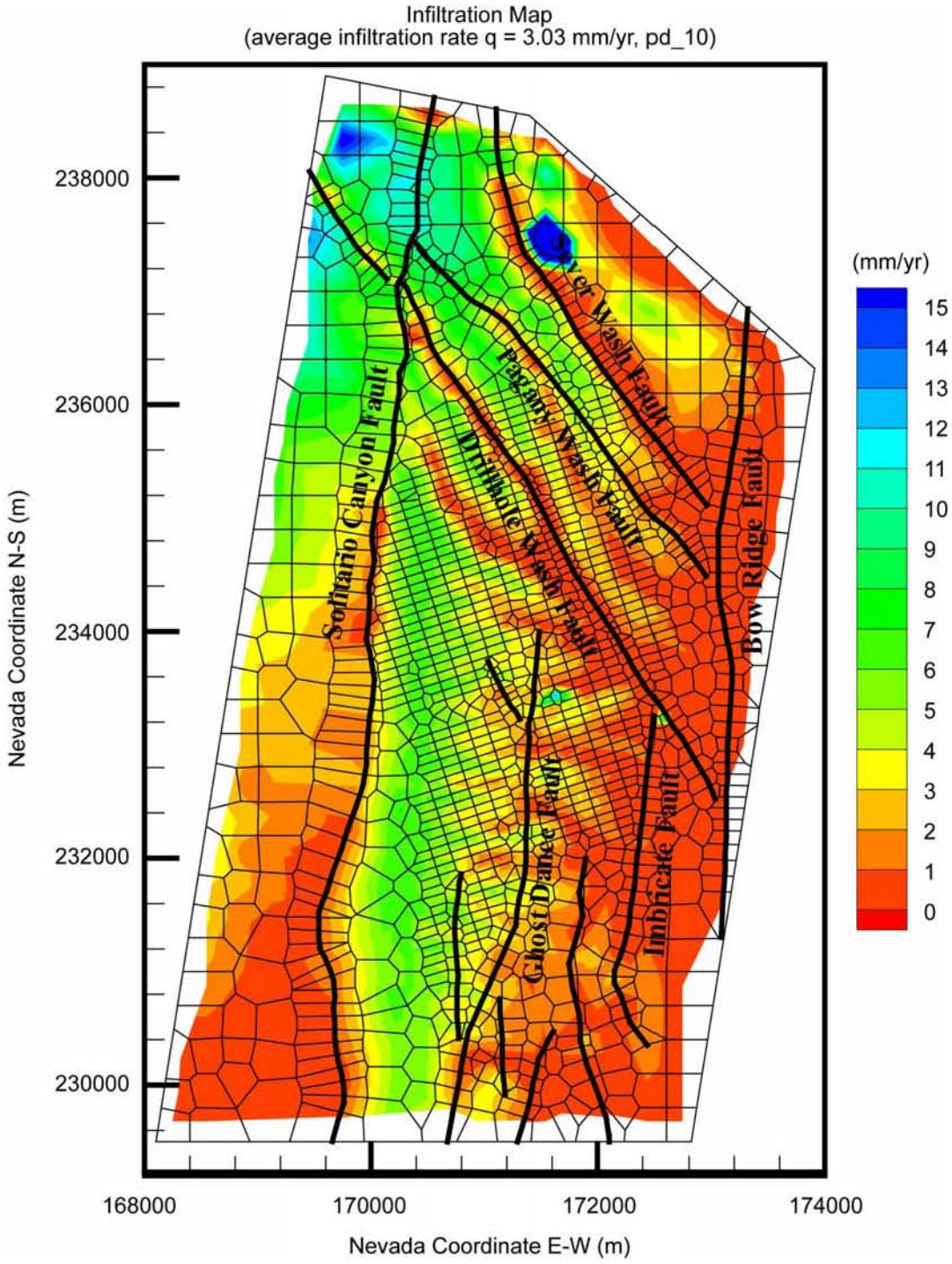

Source: DTN: SN0609T0502206.028 [DIRS 178753].

Output DTN: LB06123DPDUZFF.001.

Figure 6.1-2. Plan View of Net Infiltration Distributed over the Three-Dimensional Unsaturated Zone TSPA-LA Model Grid for the Present-Day 10th Percentile Infiltration Scenario

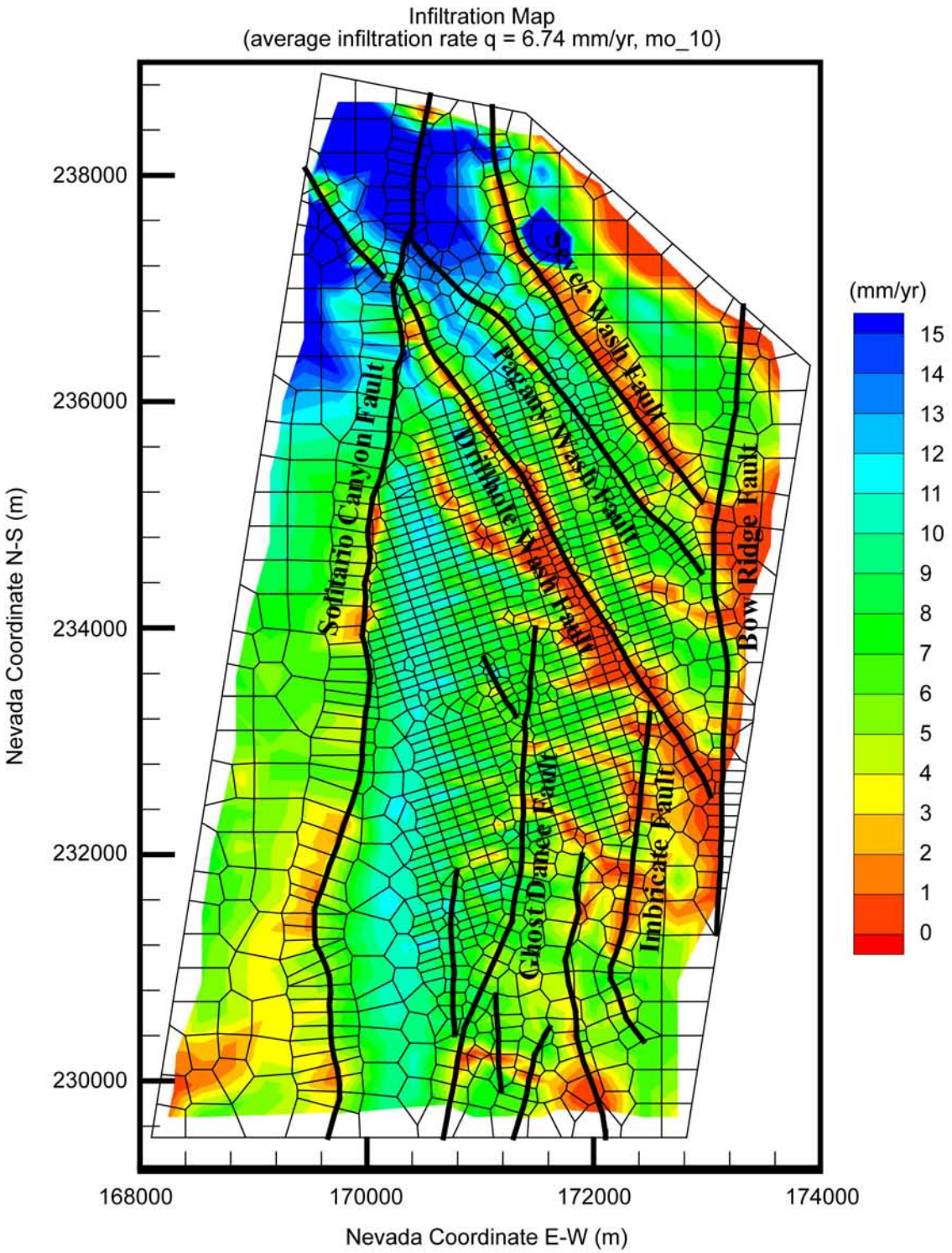

Source: DTN: SN0609T0502206.028 [DIRS 179063].
Output DTN: LB07013DMOUZFF.001.

Figure 6.1-3. Plan View of Net Infiltration Distributed over the Three-Dimensional Unsaturated Zone TSPA-LA Model Grid for the Monsoon 10th Percentile Infiltration Scenario

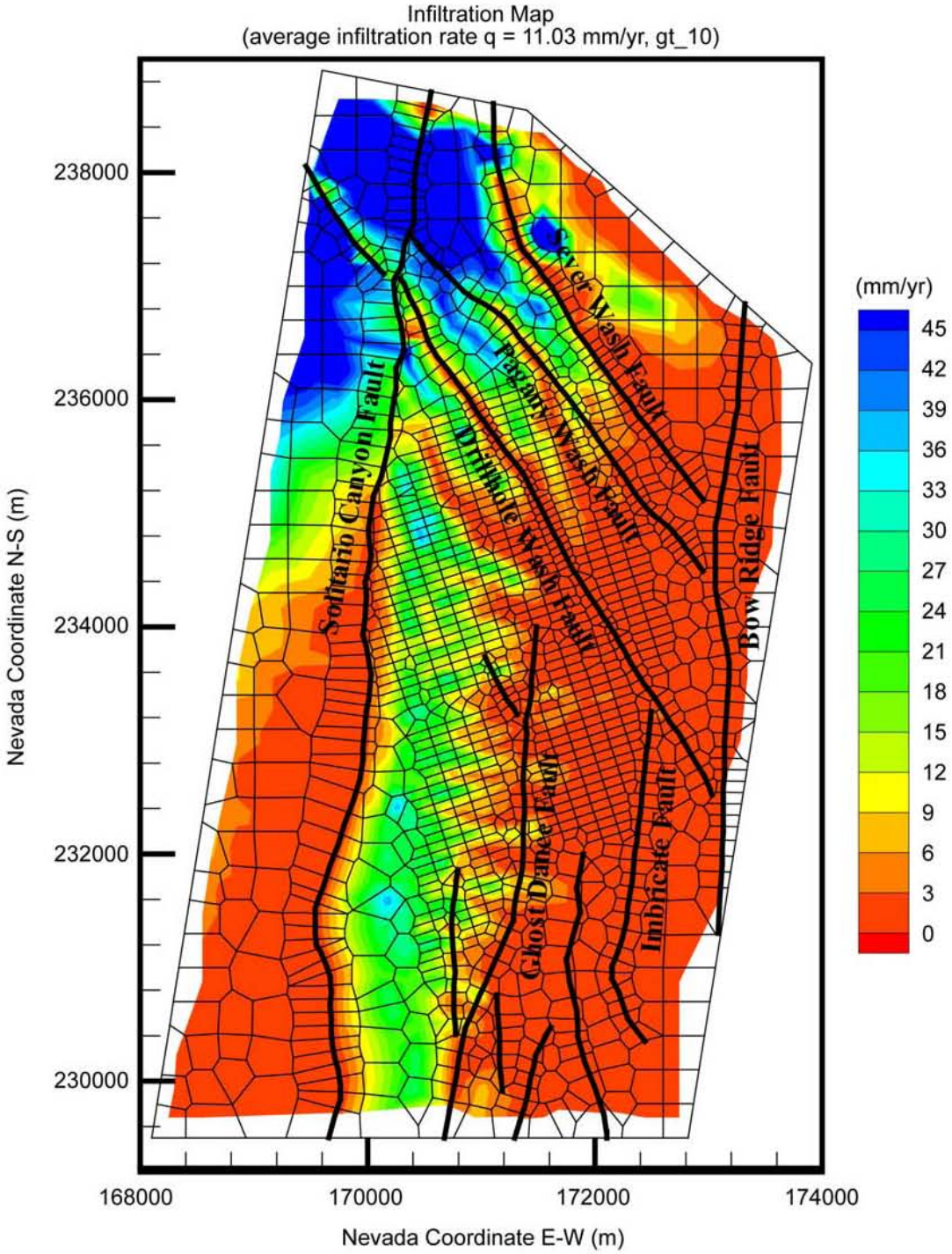

Source: DTN: SN0609T0502206.029 [DIRS 178862].

Output DTN: LB07013DGTUZFF.001.

Figure 6.1-4. Plan View of Net Infiltration Distributed over the Three-Dimensional Unsaturated Zone TSPA-LA Model Grid for the Glacial Transition 10th Percentile Infiltration Scenario

One additional climate scenario for the post-10,000-year period (post-10k-yr) was considered, using the average percolation flux ranges specified by the U.S. Nuclear Regulatory Commission (NRC) (BSC 2006 [DIRS 177465]). The stipulated distribution of average percolation flux to the repository is given as a log-uniform distribution ranging from 13 to 64 mm/yr, according to the NRC-proposed rule ([DIRS 178394], 10 CFR 63.342(c), p. 53,320). The NRC directs the Department of Energy to accordingly consider the dose calculations during the post-10k-yr time period.

Because the UZ flow model specifies flux at the upper boundary, not at an interior surface such as the repository, the appropriate flux is specified in the repository footprint projected up to the ground surface. Computations have shown that the average flux flowing to the repository is within three percent of the average flux specified at the ground surface over the projected repository area. The values for average water flux are taken to be at the same four probabilities used for present day, monsoon, and glacial transition climates. This is discussed in Section 6.8, where the calibrated probabilities for 10th, 30th, 50th, and 90th scenarios are developed. The adjusted probabilities for these cases are found to be (Table 6.8-1) 62%, 16%, 16%, and 6%, respectively. The midpoints of these probability ranges for a cumulative probability distribution are at 31%, 70%, 86%, and 97%, respectively. Using these percentiles and the log-uniform percolation flux distribution gives the values shown in Table 6.1-3, averaged over the repository footprint. An infiltration map must be developed to spatially distribute infiltration for a given average infiltration rate.

For the available 12 infiltration maps implemented for the pre-10k-yr period (10th, 30th, 50th, and 90th scenarios for each of present-day, monsoon, and glacial transition) (Table 6.1-2), the average infiltration rates through the repository footprint were first calculated. The infiltration map with a calculated average infiltration rate that most closely matches the first of the four target values (21.29, 39.52, 51.05, and 61.03 mm/yr in Table 6.1-3) for the post-10k-yr period was selected. This selection process was repeated for maps for the second through the fourth target. Then the infiltration rates for that map were scaled such that the target value for the average infiltration through the repository footprint is obtained to meet the NRC requirement. Specifically, the infiltration rates for the maps of present-day 90th percentile, glacial transition 50th percentile, glacial transition 90th percentile, and monsoon 90th percentile infiltration scenarios were then scaled such that the average infiltration flux through the repository footprint closely matched the target value. This scaled infiltration map was then used as the infiltration boundary condition for the UZ flow model to generate the post-10k-yr flow field. With the infiltration boundary condition specified, computing the post-10k-yr UZ flow fields was the same as computing the pre-10k-yr flow fields. The resulting percolation fluxes over the UZ model domain, as well as through the repository footprint for the post-10k-yr climate, are shown in Table 6.1-3. Figure 6.1-5 shows UZ flow model results for the case of the 10th percentile post-10k-yr climate.

Table 6.1-3. Average and Target Infiltration Rates for Four Selected Maps over the UZ Model Domain and within Repository Footprint for Post-10k-year Climate

Scenario	Percentile	Average Infil of Selected Map Over UZ Model Domain		Target Average Infil within Repository Footprint	
		Average (mm/yr)	Scenario	Rate (mm/yr)	Mid-point Cumulative Probability
pkd_q1	10	16.89	present-day 90th percentile	21.29	0.3096
pkd_q2	30	28.99	glacial transition 50th percentile	39.52	0.6975
pkd_q3	50	34.67	glacial transition 90th percentile	51.05	0.8582
pkd_q4	90	48.84	monsoon 90th percentile	61.03	0.9702

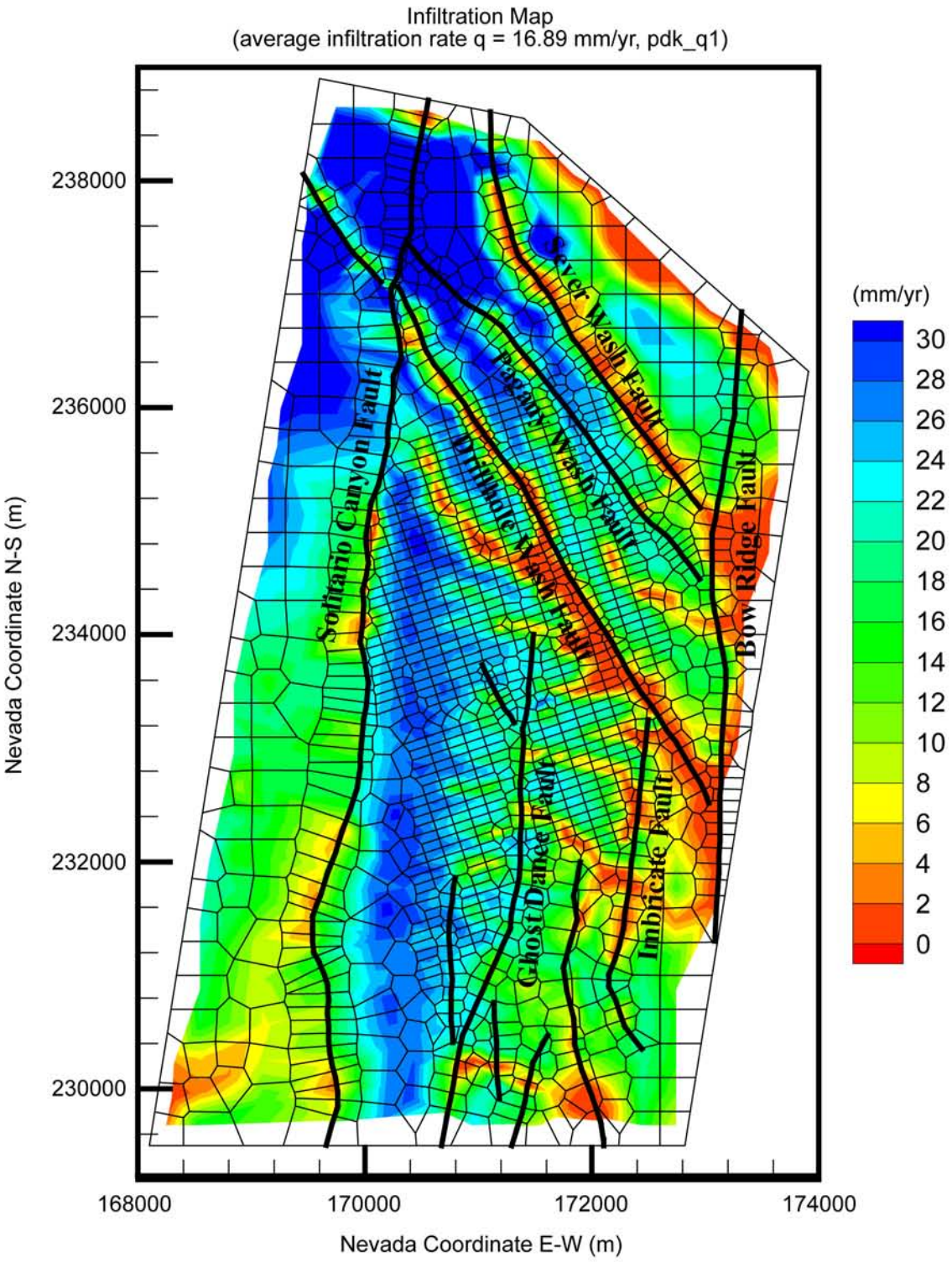

Output DTN: LB0702UZP10KFF.002.

Figure 6.1-5. Plan View of Net Infiltration Distributed over the Three-Dimensional Unsaturated Zone TSPA-LA Model Grid for the Post-10,000-yr Period Climate, 10th Percentile Infiltration Scenario

systems using a dual-permeability approach. In addition, the van Genuchten relative permeability and capillary pressure functions (van Genuchten 1980 [DIRS 100610]) are used to describe flow in fractures and matrix.

In addition to fracture and matrix properties, lithophysal cavities are found in several hydrogeological layers of upper lithophysal (tsw33) and lower lithophysal (tsw35) units. These cavities, according to their local association with fractures or matrix blocks, mainly contribute storage space to fracture or matrix systems in terms of impact on flow and transport through these tuff layers. Lithophysal cavities can be considered as part of fracture or matrix porosity, but the effect of these cavities on tracer transport from the repository to the water table is expected to be small and are not explicitly incorporated into the UZ flow model. Under steady-state flow conditions, fracture or matrix porosity does not affect UZ flow fields. This is commensurate with the main objective of the UZ flow model—development of three-dimensional steady-state UZ flow fields, which are independent of the values of fracture or matrix porosity used under steady-state flow condition. In addition, porosity has little effect on pneumatic flow, which is largely controlled by fracture properties and only negligibly by matrix porosity. However, porosity has a certain influence on transient transport. The geological layers with cavities are located either higher than or at the repository horizon, and cavities will remain dry. Little water is expected to flow through cavities, owing to the strong capillary barrier effect on seepage into cavities. Therefore, the existence of these lithophysal cavities has virtually no impact on the calibration and simulation results of the UZ flow model (Section 6.10.2).

6.2 THREE-DIMENSIONAL UZ FLOW MODEL CALIBRATION

A critical step in developing the three-dimensional UZ flow model was to use field-measured liquid saturation, water potential, perched water, and pneumatic data to calibrate the three-dimensional model. This calibration is essential for the important iterative processes of model verification, which increase confidence in model predictions for the site conditions. A detailed model-calibrating investigation is reported in *Calibrated Unsaturated Zone Properties* (SNL 2007 [DIRS 179545]), using one- and two-dimensional models for estimating model parameters with water potential, and saturation. However, these one-dimensional models cannot predict whether lateral flow or perched water occurs in several hydrogeological units of the unsaturated zone below the repository level. This section documents a further model calibration effort, focusing on three-dimensional flow patterns: perched water calibrations using the three-dimensional model grid (Figure 6.1-1).

The three-dimensional flow model calibration is conducted using the four sets of parameters of one-dimensional site-scale calibrated properties (SNL 2007 [DIRS 179545]); DTNs: LB0611MTSCHP10.001 [DIRS 178586], LB0611MTSCHP30.001 [DIRS 180293], LB0612MTSCHP50.001 [DIRS 180294], LB0612MTSCHP90.001 [DIRS 180295]), two-dimensional site-scale calibrated fault properties (DTN: LB0612MTSCHPFT.001 [DIRS 180296]), three present-day infiltration rates (see Table 6.1-2), and the geological model and numerical grid for calibration (BSC 2004 [DIRS 169855]). In addition, previously developed three-dimensional properties for the perched water zone unit (DTN: LB03013DSSCP3I.001 [DIRS 162379]) developed from *Analysis of Hydrologic Properties Data* (BSC 2004 [DIRS 170038]) and based on information from the previous version

of this report (BSC 2004 [DIRS 169861]) are adopted in this report. As shown in Section 6.2.2.2, even with

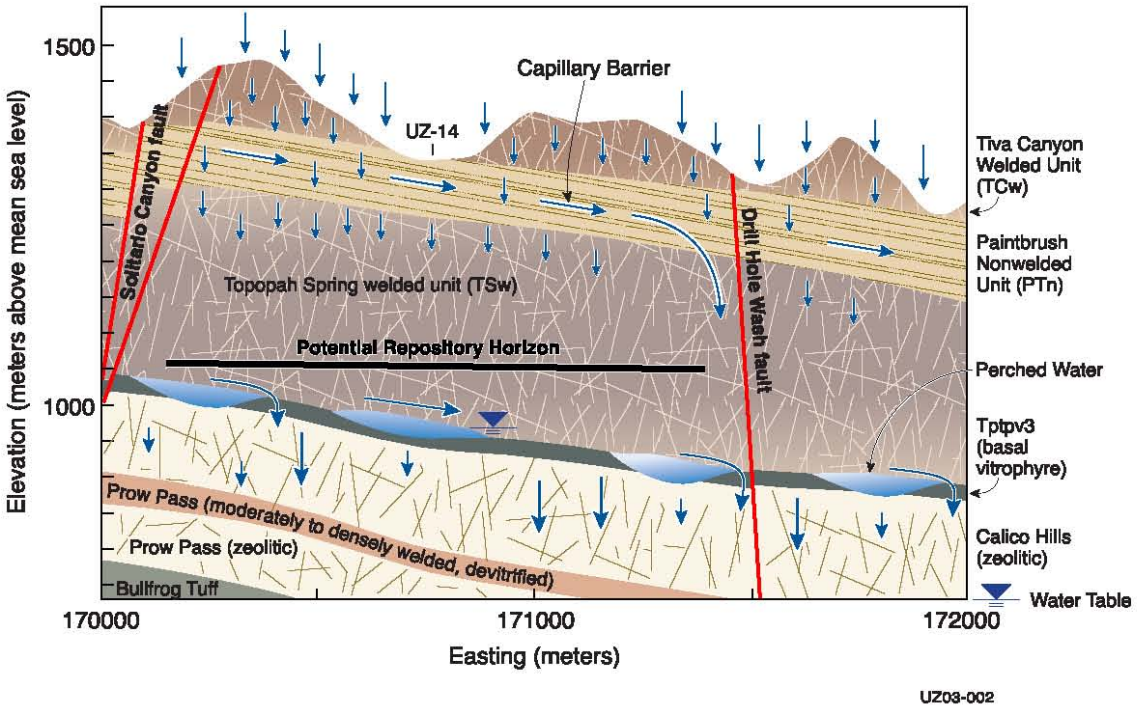

Source: For illustration purposes only.

Figure 6.2-1. Schematic Showing the Conceptualized Flow Processes and Effects of Capillary Barriers, Major Faults, and Perched Water Zones within a Typical Cross Section of the Unsaturated Zone Flow Model Domain in the East-West Direction

The PTn unit, as described by the current geological model, consists primarily of non- to partially welded tuffs. The dip of these layers is generally less than 10° to the east or southeast. The combined thickness of the PTn layers ranges from 150 m in the north of the model area to 30 m or less, even completely disappearing in several areas of the south. However, the PTn unit is present over the entire repository area, where the thickness of the PTn unit ranges from approximately 30 to 60 m. The PTn unit as a whole exhibits very different hydrogeologic properties from the TCw and TSw units that bound it above and below. The TCw and TSw units have low porosity and intense fracturing typical of the densely welded tuffs at Yucca Mountain. In contrast, the PTn has high porosity and low fracture intensity, and its matrix system has a large capacity for storing groundwater. It has been shown to effectively damp spatial and temporal variations in percolation flux (Wu et al. 2000 [DIRS 154918], pp. 30 to 32 and 39 to 41; Zhang et al. 2006 [DIRS 180273]). Therefore, water flow through the unsaturated zone is modeled to occur under steady-state conditions, while the temporal damping effect of episodic flux is studied in Section 6.9.

6.2.2.1 Capillary Barriers

The concept of capillary barriers has been advanced to explain flow behavior within the PTn at Yucca Mountain (Montazer and Wilson 1984 [DIRS 100161], pp 26 to 30). These capillary barriers are due to the large contrast in rock properties across predominantly horizontal interfaces within the PTn unit. The presence of faults and larger fractures prevents development of

extensive lateral flow or laterally extensive or continuous capillary barriers. Field data obtained from tens of boreholes have been used to characterize the distribution of rock properties within the PTn unit. In general, field data indicate that the Yucca Mountain formation is more heterogeneous vertically than horizontally, so that layer-wise representations provide a reasonable approximation of the complex geological system. Calibration using this conceptual model matches different types of observation data, as further demonstrated in the following sections. However, characterizing general flow behavior within the unsaturated zone system is complicated by the presence of faults, which interrupt the lateral continuity in the rock matrix properties of sloping layers.

The key conceptualizations made in the UZ flow model concerning lateral flow above the repository horizon are as follows: (1) the hydrogeological units/layers are internally homogeneous, and the material properties of each unit are continuous throughout each layer (Table 6.1-1) unless interrupted by faults; (2) ambient water flow in the system is at a steady-state condition; and (3) faults are represented by vertical or inclined columns of gridblocks having finite or small width. The flow patterns associated with capillary barriers within the PTn are studied in the following sections using this conceptual model.

6.2.2.2 Perched Water

Conceptual models of perched water occurrence are of particular interest in assessing the system performance of the repository and UZ flow patterns below the repository. Waste-isolation strategies and unsaturated zone natural barrier capability depend, in part, on sorption within the zeolitic portions of the CHn and on tracer transport times between the repository horizon and the water table. Several conceptual models have been proposed for the genesis of perched water at Yucca Mountain (e.g., Wu et al. 1999 [DIRS 117167]; Wu et al. 2004 [DIRS 173953]).

Perched water may occur where percolation flux exceeds the capacity of the geological media to transmit vertical flux in the unsaturated zone. Perched water has been encountered in a number of boreholes at Yucca Mountain, including UZ-14, SD-7, SD-9, SD-12, NRG-7a, G-2, and WT-24. These perched water occurrences are found to be associated with low-permeability zeolites in the CHn or the densely welded basal vitrophyre (Tptpv3, Table 6.1-1) of the TSw unit. Some possible mechanisms of water perching in the unsaturated zone of Yucca Mountain may be permeability or capillary barrier effects at faults, or a combination of both.

The permeability-barrier conceptual model for perched water occurrence has been used in UZ flow modeling studies since 1996 (Wu et al. (1999 [DIRS 117167]; Wu et al. 2004 [DIRS 173953]). In this model, perched water bodies in the vicinity of the ESF North Ramp (near Boreholes UZ- 14, SD-9, NRG-7a, G-2, and WT-24) are observed to occur above the base of the TSw, underlain by a zone of low-permeability, zeolitized rock. The perched water bodies in this northern area of the repository may be interconnected. However, the perched water zones at Boreholes SD-7 and SD-12 are considered here as local, isolated bodies. In this conceptual model, vertical and lateral water movement in the vicinity of the perched zones is considered to be controlled mainly by the fracture and matrix permeability distribution in these areas. The major aspects of the permeability-barrier conceptual model are: (1) no large-scale, vertically connected, potentially fluid-conducting fractures transect the underlying low-permeability units; (2) vertical and horizontal permeabilities within and below the perched water zone are small

- Near borehole SD-7, properties for the gridblocks in grid columns q45, i80, i81, i84, i87, o92, and o95, over grid layers of ch5z (ch5Fz/ch5Mz), ch6z (ch6Fz/ch6Mz) and pp4 (pp4Fz/pp4Mz) are replaced by (pcF5z/pcM5z), (pcF6z/pcM6z), and (pcF4p/pcM4p), respectively.

- Near borehole SD-12, properties for the gridblocks in grid columns q47, b93, b99, k61, k62 and k67, over grid layers of tsw38 (tswF8/tswM8), tsw39 (tswF9/tswM9), and ch1v (ch1Fv/ch1Mv) are replaced by (pcF38/pcM38), (pcF39/pcM39), and (pcF1z/pcM1z), respectively.

Fracture and matrix permeabilities of potential perched layers/zones, as identified above, are calibrated based on the three-dimensional model calibrated values and shown in Tables 6.2-2, 6.2-3, and 6.2-4. All properties except intrinsic permeabilities, van Genuchten's α and m parameters, and residual saturations for matrix blocks within perched zones are identical to parameters estimated from the current one-dimensional calibrations discussed in *Calibrated Unsaturated Zone Properties* (SNL 2007 [DIRS 179545]). The active-fracture parameter, γ, is set to zero for the perched zones, causing the fracture and matrix interface-area factor to be equivalent to liquid saturation (Liu et al. 1998 [DIRS 105729]). Tables 6.2-2, 6.2-3, 6.2-4, and 6.2-5 present the final four sets of calibrated rock properties at zones with perched water, with 10th, 30th, 50th, and 90th present-day infiltration scenarios, respectively. The modified "fracture" properties in the following three tables are close to those of the matrix, so that fractures in water perching layers are effectively removed.

In Tables 6.2-2 to 6.2-5, as well as those in Appendix B, the symbols and notations standing for parameters are defined as follows: k_M and k_F are intrinsic permeability of matrix and fracture systems; α_M and α_F are van Genuchten α parameters of the matrix and fracture systems; m_M and m_F are van Genuchten m parameters of the matrix and fracture systems; and γ is the AFM parameter.

Table 6.2-2. Calibrated Parameters of Perched Water Conceptual Model for the Present-Day, 10th Percentile Infiltration Scenario

Model Layer	k_M (m^2)	α_M (1/Pa)	m_M (−)	k_F (m^2)	α_F (1/Pa)	m_F (−)	γ (−)
pcM38/ pcF38	3.000×10^{-19}	1.878×10^{-6}	0.286	3.000×10^{-18}	1.878×10^{-6}	0.286	0.00
pcM39/ pcF39	6.200×10^{-18}	4.610×10^{-6}	0.059	6.200×10^{-17}	4.610×10^{-6}	0.059	0.00
pcM1z/ pcF1z	9.300×10^{-20}	2.120×10^{-7}	0.349	9.300×10^{-19}	2.120×10^{-7}	0.349	0.00
pcM2z/ pcF2z	2.400×10^{-18}	2.250×10^{-6}	0.257	2.400×10^{-17}	2.250×10^{-6}	0.257	0.00
pcM5z/ pcF5z	2.400×10^{-18}	2.250×10^{-6}	0.257	2.400×10^{-18}	2.250×10^{-6}	0.257	0.00
pcM6z/ pcF6z	1.100×10^{-19}	1.560×10^{-7}	0.499	1.100×10^{-19}	1.560×10^{-7}	0.499	0.00
pcM4p/ pcF4p	7.700×10^{-19}	6.310×10^{-6}	0.474	7.700×10^{-19}	6.310×10^{-6}	0.474	0.00

Output DTN: LB07043DCRXPRP.001.

Table 6.2-3. Calibrated Parameters of Perched Water Conceptual Model for the Present-Day, 30th Percentile Infiltration Scenario

Model Layer	k_M (m^2)	α_M (1/Pa)	m_M (–)	k_F (m^2)	α_F (1/Pa)	m_F (–)	γ (–)
pcM38/ pcF38	3.000×10^{-19}	3.105×10^{-6}	0.286	3.000×10^{-18}	3.105×10^{-6}	0.286	0.00
pcM39/ pcF39	6.200×10^{-18}	4.610×10^{-6}	0.059	6.200×10^{-17}	4.610×10^{-6}	0.059	0.00
pcM1z/ pcF1z	9.300×10^{-20}	2.120×10^{-7}	0.349	9.300×10^{-19}	2.120×10^{-7}	0.349	0.00
pcM2z/ pcF2z	2.400×10^{-18}	2.250×10^{-6}	0.257	2.400×10^{-17}	2.250×10^{-6}	0.257	0.00
pcM5z/ pcF5z	2.400×10^{-18}	2.250×10^{-6}	0.257	2.400×10^{-18}	2.250×10^{-6}	0.257	0.00
pcM6z/ pcF6z	1.100×10^{-19}	1.560×10^{-7}	0.499	1.100×10^{-19}	1.560×10^{-7}	0.499	0.00
pcM4p/ pcF4p	7.700×10^{-19}	6.310×10^{-7}	0.474	7.700×10^{-19}	6.310×10^{-7}	0.474	0.00

Output DTN: LB07043DCRXPRP.001.

Table 6.2-4. Calibrated Parameters of Perched Water Conceptual Model for the Present-Day, 50th Percentile Infiltration Scenario

Model Layer	k_M (m^2)	α_M (1/Pa)	m_M (–)	k_F (m^2)	α_F (1/Pa)	m_F (–)	γ (–)
pcM38/ pcF38	3.000×10^{-19}	3.691×10^{-6}	0.286	3.000×10^{-18}	3.691×10^{-6}	0.286	0.00
pcM39/ pcF39	6.200×10^{-18}	4.610×10^{-6}	0.059	6.200×10^{-17}	4.610×10^{-6}	0.059	0.00
pcM1z/ pcF1z	9.300×10^{-20}	2.120×10^{-7}	0.349	9.300×10^{-19}	2.120×10^{-7}	0.349	0.00
pcM2z/ pcF2z	2.400×10^{-18}	2.250×10^{-6}	0.257	2.400×10^{-17}	2.250×10^{-6}	0.257	0.00
pcM5z/ pcF5z	2.400×10^{-18}	2.250×10^{-6}	0.257	2.400×10^{-18}	2.250×10^{-6}	0.257	0.00
pcM6z/ pcF6z	1.100×10^{-19}	1.560×10^{-7}	0.499	1.100×10^{-19}	1.560×10^{-7}	0.499	0.00
pcM4p/ pcF4p	7.700×10^{-19}	6.545×10^{-6}	0.474	7.700×10^{-19}	6.545×10^{-6}	0.474	0.00

Output DTN: LB07043DCRXPRP.001.

Table 6.2-5. Calibrated Parameters of Perched Water Conceptual Model for the Present-Day, 90th Percentile Infiltration Scenario

Model Layer	k_M (m^2)	α_M (1/Pa)	m_M (–)	k_F (m^2)	α_F (1/Pa)	m_F (–)	γ (–)
pcM38/ pcF38	3.000×10^{-19}	4.777×10^{-6}	0.286	3.000×10^{-18}	4.777×10^{-6}	0.286	0.00
pcM39/ pcF39	6.200×10^{-18}	4.610×10^{-6}	0.059	6.200×10^{-17}	4.610×10^{-6}	0.059	0.00
pcM1z/ pcF1z	9.300×10^{-20}	2.120×10^{-7}	0.349	9.300×10^{-19}	2.120×10^{-7}	0.349	0.00
pcM2z/ pcF2z	2.400×10^{-18}	2.250×10^{-6}	0.257	2.400×10^{-17}	2.250×10^{-6}	0.257	0.00
pcM5z/ pcF5z	2.400×10^{-18}	2.250×10^{-6}	0.257	2.400×10^{-18}	2.250×10^{-6}	0.257	0.00
pcM6z/ pcF6z	1.100×10^{-19}	1.560×10^{-7}	0.499	1.100×10^{-19}	1.560×10^{-7}	0.499	0.00
pcM4p/ pcF4p	7.700×10^{-19}	6.310×10^{-6}	0.474	7.700×10^{-19}	6.310×10^{-6}	0.474	0.00

Output DTN: LB07043DCRXPRP.001.

The third and last parameter adjustment is the fracture permeability in the TCw and TSw units under the present-day, 10th and 30th percentile infiltration scenarios (see Section 6.4). The present-day, 10th and 30th percentile infiltration rates are used for gas flow calibration because the pneumatic tests were conducted in a small time scale of days to years at present-day conditions. This calibration, described in Section 6.4, was made from three-dimensional gas

Mass Balance and Solution Convergence: Table 6.2-7 shows the mass-balance results for the sixteen simulation scenarios. In Table 6.2-7, "inflow" is the total infiltration rate over the entire model top boundary, representing a net water recharge rate (water mass) into the system for the infiltration scenario simulated. "Outflow" is the cumulative total-flow rate out of the model and into the lower boundary representing the water table. Global mass-balance errors between inflow and outflow from the system, as shown in Table 6.2-7, are less than 0.013% for all 16 simulations, leading to the conclusion that steady-state solutions are obtained for all the simulations.

Table 6.2-7. Mass-Balance Results for Checking Steady State Status of Sixteen Flow Simulation Results

Simulation Scenarios	Inflow from Infiltration (kg/s)	Outflow to Water Table (kg/s)	Relative Error (%)
pd_10	3.821408495	3.8210676	0.0089
pd_30	10.05089517	10.0496168	0.0127
pd_50	15.50822442	15.5082076	0.0001
pd_90	33.81826331	33.8182842	0.0001
mo_10	8.511510348	8.5115148	0.0001
mo_30	16.28484915	16.2848381	0.0001
mo_50	19.41794042	19.4179219	0.0001
mo_90	92.51816511	92.5183180	0.0002
gt_10	13.93611829	13.9360979	0.0001
gt_30	25.82297803	25.8229675	0.0001
gt_50	32.81793890	32.8179286	0.0000
gt_90	58.95021503	58.9500578	0.0003
pkd_q1	21.33438025	21.3344012	0.0001
pkd_q2	36.61220864	36.6123755	0.0005
pkd_q3	43.78254941	43.7827807	0.0005
pkd_q4	61.67639555	61.6727082	0.0060

Output DTNs: LB06123DPDUZFF.001; LB07013DMOUZFF.001; LB07013DGTUZFF.001; LB0702UZP10KFF.002.

Model Calibrations and Results: As listed in Table 6.2-6, there are a total of 16 model scenarios, covering 16 infiltration rate distributions for four (present-day, monsoon, glacial transition, and post-10k-yr) climates. The four present-day cases (10th, 30th, 50th, and 90th percentiles) out of the 16 simulations are for model calibrations, and the other twelve scenarios are forward runs for providing UZ flow fields as well as sensitivity analyses. The four present-day simulations have been calibrated against the field-observed data of perched water. In addition, the observed matrix liquid saturations and water potentials (when available) are also used to examine these modeling results. A perched water body is defined as fully liquid saturated gridblocks with zero capillary pressure for calibration. The data sources used in the calibrations are listed in Section 4.1 and in Table 6.2-1. Only in situ measurements of water potentials are used in this analysis. In this section, the results of the four present-day simulations are presented and discussed in terms of: (1) comparisons with matrix liquid saturation, water potential, and perched water data; (2) examination of simulated perched water bodies; and (3) examination of simulated percolation flux and fracture–matrix flow components.

All 12 simulations for the present-day, monsoon, and glacial transition climates are checked against observed saturation, water potential, and perched water data. Only a few of these comparisons are shown here, and boreholes UZ-14 and SD-12 are selected to show the match between observed and modeled vertical-saturation profiles and perched water locations for four present-day climate simulations with perched water occurrence. Table C-1 lists the surface elevations and coordinates of selected boreholes for conversion from depth to elevation. Matches to other borehole data are similar. Most borehole observation data used in this section and the following sections are given relative to depth. In plots of this report, elevations are used to illustrate model results and comparisons. Appendix D provides more comparisons of the saturation and potential profiles of all boreholes evaluated by the model.

Matrix saturation and water potential data are not used in the GLUE analysis in Section 6.8, because, as shown below, simulated distributions for the matrix saturation and water potential are not very sensitive to the percolation flux in the unsaturated zone. Pneumatic pressure data are not considered, either, because the water percolation process does not significantly affect pneumatic signals in the unsaturated zone when fractures are very dry.

Comparisons with Liquid Saturation, Water Potential, and Perched Water Data: Measured matrix liquid saturation, water-saturation data and perched water elevations are compared against three-dimensional model results from the twelve simulations. Matrix liquid saturation, water potential, and perched water data used for comparisons are taken from nine boreholes (NRG-7a, SD-6, SD-7, SD-9, SD-12, UZ-14, UZ#16, WT-24, and G-2). The locations of these boreholes are shown in Figure 6.1-1.

The comparisons of simulated and observed matrix liquid saturations along the vertical column representing boreholes UZ-14 and SD-12 are shown, as examples, in Figures 6.2-2 and 6.2-3, from the UZ flow models with four present-day infiltration scenarios. Plots for seven other boreholes are documented in Appendix D-1. Figure 6.2-4 shows a comparison with water potentials for SD-12. In general, the modeled results from the twelve simulations with the UZ flow conceptual model are in reasonable agreement with the measured saturation and water-potential profiles, as shown in Figures 6.2-2, 6.2-3, and 6.2-4. It should be mentioned that there are some differences between simulated and observed saturation data, as shown in Figures 6.2-2, 6.2-3, and 6.2-4, which are primarily caused by formation heterogeneity and grid coarseness. In Figures 6.2-2 and 6.2-3, saturations simulated for the lower portion of the TSw with the pd_90 scenario are lower than the rest of the lower infiltration scenarios. This is because the simulations for each infiltration scenario use different parameter sets. Nevertheless, simulation results are still within ranges of measured saturation data.

Table 6.2-8. FEPs Addressed in This Report

FEP Number and FEP Name	FEP Description	Summary of Technical Basis and Approach for FEP Inclusion
1.2.02.01.0A Fractures	Groundwater flow in the Yucca Mountain region and transport of any released radionuclides may take place along fractures. The rate of flow and the extent of transport in fractures are influenced by characteristics such as orientation, aperture, asperity, fracture length, connectivity, and the nature of any linings or infills.	Fractures are included in process models for unsaturated zone flow and transport by using models based on the dual-permeability concept, with fractures represented by a distinct continuum. The fracture continuum models spatially average flow through discrete fractures. The fracture continuum interacts with the matrix continuum, which represents matrix blocks separated by the network of fractures. Fracture porosity, fracture spacing, and fracture volume fraction measured in the field and within different stratigraphic units determine geometrical parameters of fractures that are incorporated in the model.
1.2.02.02.0A Faults	Numerous faults of various sizes have been noted in the Yucca Mountain region, and specifically in the repository area. Faults may represent an alteration of the rock permeability and continuity of the rock mass, an alteration or short-circuiting of the flow paths and flow distributions close to the repository, and (or) unexpected pathways through the repository.	Stratigraphic displacement, dip-slip, strike-slip, and detachments due to faulting within the model domain are explicitly discretized in the site-scale unsaturated zone flow and transport models. Specific hydrogeologic properties are assigned to the fault zones, supported by measurements within fault zones or across faults. The net effect on flow is reflected in the unsaturated zone flow fields that include flow through faults.
1.3.01.00.0A Climate change	Climate change may affect the long-term performance of the repository. This includes the effects of long-term change in global climate (e.g., glacial–interglacial cycles) and shorter-term change in regional and local climate. Climate is typically characterized by temporal variations in precipitation and temperature.	Climate change is addressed in TSPA based on the record of climate changes in the past, which are used to predict the expected changes in climate for the future. Climate modeling is incorporated into TSPA through the unsaturated zone flow fields that use different surface water flux boundary condition maps corresponding to three different climates during the first 10,000 years. This is incorporated in TSPA through the unsaturated zone flow model output, which uses the results of the infiltration model to assign the water flux boundary conditions at the model's upper boundary. For the post-10,000-year period, the surface water flux boundary condition for the unsaturated zone flow model is assigned using the percolation flux distribution given in the proposed rule (70 Fed. Reg. 173).
1.3.07.02.0B Water table rise affects unsaturated zone	Climate change could produce increased infiltration, leading to a rise in the regional water table, possibly affecting radionuclide release from the repository by altering flow and transport pathways in the unsaturated zone. A regionally higher water table and change in unsaturated zone flow patterns might flood the repository.	The potential for water table rise caused by climate change is included in TSPA calculations using a water table rise model based on climate data, which allows the water table to change elevation instantaneously upon change in climate.
1.4.01.01.0A Climate modification increases recharge	Climate modification causes an increase in recharge in the Yucca Mountain region. Increased recharge might lead to increased flux through the repository, perched water, or water table rise.	The effects of climate changes on unsaturated zone flux through the repository are incorporated through explicit simulations of unsaturated zone flow fields corresponding to the four uncertainty cases for water flux at the upper boundary of the unsaturated zone flow model and three distinct climate states: present-day, monsoon, and glacial transition as well as the post-10,000-year period.

6.3 TEMPERATURE CALIBRATION

The percolation and moisture distributions under present-day conditions are used as initial conditions for performing thermal-hydrological studies of the unsaturated zone system, as well as repository performance studies under thermal loading conditions. The ambient geothermal and moisture conditions serve as the initial and boundary conditions of a thermal model (Wu et al. 2006 [DIRS 180274]). This section describes a three-dimensional ambient geothermal submodel of the UZ model developed to evaluate steady-state, ambient thermal, and moisture conditions of the unsaturated zone system with different infiltration rates for use in various scale TH modeling studies. Subsequent temperature calibration then provides an independent examination of percolation fluxes simulated by the UZ flow model. As discussed in Section 6.3.4, percolation flux (or infiltration rate) is one of the factors that control the ambient temperature distribution within the unsaturated zone (Bodvarsson et al. 2003 [DIRS 162477]). By matching borehole temperature measurements, the ambient TH model helps to constrain infiltration-rate ranges as well as fracture–matrix parameter values. Note that except for this section, the rest of the three-dimensional model development and calibration in this report deal with isothermal conditions. The three-dimensional calibrated isothermal unsaturated zone flow properties developed in Section 6.2 are used in the three-dimensional thermal model.

6.3.1 Three-Dimensional Thermal Model Grid

For thermal calibration as well as the gas flow calibration described in the next section, a three-dimensional grid (Figure 6.3-1), smaller than the TSPA-LA grid (Figure 6.1-1), is used (DTN: LB0303THERMESH.001 [DIRS 165168]). This grid is designed to reduce the computational burden needed in thermal modeling studies using a three-dimensional dual-permeability grid. The thermal model domain is selected to focus on geothermal conditions and thermal loading effects at and near the repository area. The model domain is considered to provide sufficient accuracy for such studies, because of the small thermal impact expected in the lateral directions from repository thermal loading.

This three-dimensional grid, featuring a smaller model domain than that of the UZ flow model (Figure 6.1-1), is referred to as the three-dimensional thermal model grid. As shown in the plan view of Figure 6.3-1, the thermal-model-grid domain covers approximately 20 km^2 of the area. Similar to the TSPA-LA grid of Figure 6.1-1, the thermal model grid (Figure 6.3-1) also uses a refined mesh in the vicinity of the repository and includes the locations of several boreholes used in temperature calibrations and analyses. In particular, the thermal model grid explicitly incorporates every repository drift by taking into account orientations, lengths, elevations, and spacings of the drifts. A grid spacing of 81 m is used in the direction perpendicular to drifts, such that each individual drift segment can be inserted into the three-dimensional thermal grid for thermal loading studies, such as in a previous report (BSC 2005 [DIRS 174101]; Wu et al. 2006 [DIRS 180274]). In the model, faults are also represented by vertical or inclined 30 m wide zones.

(DTNs: GS031208312232.008 [DIRS 178750], GS951108312232.008 [DIRS 106756], and GS950208312232.003 [DIRS 105572]), with several years of continuous temperature monitoring data. The surface temperatures, T_s, at any elevation, Z, are then computed using the routine toptemp_v0.f V1.0 (LBNL 2000 [DIRS 147030]), and are treated as constants according to the following equation (Wu et al. 1999 [DIRS 117161], Equation 4):

$$T_s = T_{ref} - \lambda[Z - Z_{ref}] \quad \text{(Eq. 6.3-1)}$$

where T_{ref} is mean surface temperature at reference elevation Z_{ref} and λ is the dry adiabatic atmospheric lapse rate in °C/m. A lapse rate of is 0.01°C/m was adopted from Driscoll (1986 [DIRS 116801], p. 50). In this formulation, the surface reference temperature used is 18.23°C at an elevation of 1,231.0 m, averaged using measured data from borehole NRG-6. The averaged temperature measurement of NRG-7a at an elevation of 1,282.2 m is 17.78°C. The calculated mean lapse rate, based on these field measurements, is 0.009°C/m, which is consistent with the value presented by Driscoll (1986 [DIRS 116801], p. 50). Because the lapse rate estimated in this report is based on a limited number of borehole temperature data, Driscoll's value, that may be more reliable, is adopted for the calculations.

Uncertainty in the predicted temperatures is mainly a result of uncertainty in the bottom boundary conditions and the thermal conductivity. The standard deviation for temperature at the ground surface is small (approximately ± 0.1°C). The temperature measurements at about 20 m below the ground surface are stable over time. Using the top boundary conditions from previous calculations should be adequate for the current ambient thermal simulation.

6.3.3 Bottom Boundary Temperature

The bottom temperature boundary condition was first estimated using the software routine of get_temp_v0.f V1.0 (2000 [DIRS 147027]) at a flat surface of an elevation of 730 m. Because the water table is no longer flat with the current UZ and TH models, the actual estimates of the water table or bottom-model-boundary temperatures were interpolated between the values at 730 m elevation and the model surface boundary. Nonqualified measured temperature profiles (Sass et al. 1988 [DIRS 100644]; DTN: GS950408318523.001 [DIRS 107244]) are qualified in Appendix I and used to confirm water table boundary temperature contours in DTN: LB0303THERMSIM.001 [DIRS 165167]. The initially estimated water table temperatures show a good match to the measurements through comparison with the qualified temperature data in boreholes NRG-6, NRG-7a, SD-12 UZ#4, UZ#5, and UZ-7A (DTNs: GS950208312232.003 [DIRS 105572], GS031208312232.005 [DIRS 179284], GS031208312232.004 [DIRS 182187], GS031208312232.007 [DIRS 178751], GS031208312232.006 [DIRS 182186], and GS031208312232.003 [DIRS 171287]).

Uncertainty in temperatures for defining the bottom temperature boundary conditions is relatively small. This is because a multiple-year temperature data set (qualified in Appendix I with Output DTN: LB0708WTTEMDAT) was used to derive the temperature distributions at the water table, the model bottom temperature boundary. The long-term variation of the measured temperatures is minor, with standard deviation < 0.1°C in 32 out of the 34 boreholes. Somewhat larger deviation over certain measurement periods was found in a couple of boreholes, with borehole NRG-7a having a maximum deviation of 0.24°C/yr, and borehole

NRG-6 of 0.58°C/yr (Appendix I, Table I-1). In addition, the data set also provides comparable temperature values when compared to the 6 qualified boreholes in the ambient thermal model. Specifically, their temperature differences obtained from borehole-location-wise proximity, are within 0.82°C, or less than 3.6% (Appendix I, Table I-3). Using the bottom temperature boundary conditions from these data is adequate for the current ambient thermal simulation.

6.3.4 Calibration of Ambient Temperatures

The temperature profiles or geothermal gradients in the unsaturated zone system are controlled by several factors, such as formation thermal conductivity and net infiltration rates, in addition to the regional weather conditions or surface temperatures. Measured thermal conductivities are relatively accurate for the different geological units at the site. Because of the fewer uncertainties involved in measured thermal conductivities related to simulated heat flow, temperature calibration may be conducted using either ambient infiltration, or model boundary temperatures, or both (Wu et al. 2006 [DIRS 180274]).

In this report, four ambient net infiltration rates for the present-day climate of 10th, 30th, 50th, and 90th percentile infiltration maps are used. The mean infiltration rates within the grid domain (Figure 6.3-1) are 2.88, 7.79, 11.65, and 27.42 mm/yr, respectively, for the four infiltration maps (output DTN: LB0701UZMTHCAL.001), which are averaged over a smaller model domain than the UZ flow model domain (Figure 6.1-1), resulting in a smaller mean infiltration value.

The ambient temperature condition was calibrated using the three-dimensional thermal model grid of Figure 6.3-1 (DTN: LB0303THERMESH.001 [DIRS 165168]), a dual-permeability mesh. The simulations were performed using TOUGH2 V1.6 (LBNL 2003 [DIRS 161491]) with the EOS3 module. In addition to the prescribed temperature conditions on the top and bottom boundaries, the infiltration was described using one of the four infiltration scenarios for present-day climate of 10th, 30th, 50th, and 90th percentile infiltration maps. The model incorporated the parameter set of Tables B-1, B-2, B-3, and B-4 (Output DTNs: LB07043DCRXPRP.001, LB0701UZMTHCAL.001), and the thermal properties (DTN: LB0210THRMLPRP.001 [DIRS 160799]). Incorporated thermal properties include effects of lithophysal cavities for TSw layers tsw33 and tsw 35. Simulations were run to steady state for comparison with measured borehole temperatures, because as shown below, the unsaturated zone is in thermal equilibrium with the present-day climatic conditions.

To evaluate the present conditions with respect to longer-term temporal variability in climate, first consider that the last significant change in climate occurred about 10,000 years ago. The 10th-percentile case from the infiltration model for present-day climate has an average flux rate of about 3 mm/yr over the UZ flow model domain. An average effective thermal diffusivity of about 4×10^{-7} m^2/s for the unsaturated zone at Yucca Mountain can be computed from the data given by Bodvarsson et al. (2003 [DIRS 162477], Table 2 and Equation 8b). For an average water content of the rock of about 0.15, this gives an advective distance of a thermal front of about 200 m and a diffusive distance of about 500 m over 10,000 years (based on the diffusion front length scale that is the square root of twice the diffusivity times the time). Furthermore, lateral thermal diffusion between flowing fractures separated by distances less than 100 m would require less than 500 years to approach thermal equilibrium. Therefore, the unsaturated zone is in

steady-state thermal equilibrium with present-day climate conditions. This conclusion is not

model (i.e., calibrated ambient temperature distribution) can be used to specify initial conditions for other mountain-scale TH simulations.

Wu et al. (1999 [DIRS 117161], Figure 12) identified that data sources were from 25 boreholes documented mainly in the report (Sass et al. (1988 [DIRS 100644]) and observed that, in general, the measured data matched reasonably with early three-dimensional model results (Bodvarsson et al. 1997 [DIRS 100103]; Ahlers et al. 1995 [DIRS 101180]). The majority of the early temperature data in *Temperature, Thermal Conductivity, and Heat Flow Near Yucca Mountain, Nevada: Some Tectonic and Hydrologic Implications* (Sass et al. 1988 [DIRS 100644]) are currently not qualified. In this report, six qualified data sets of temperature distributions along boreholes are shown to be consistent with the water table distribution developed from the more extensive data set, demonstrating the consistency of water temperature distribution with unsaturated processes. The same extensive data set is also the basis for saturated zone interpretation of Fridrich et al. (1994 [DIRS 100575], pp. 133 to 168). Fridrich et al. (1994 [DIRS 100575], p. 157) discussed the heat flow anomalies, upward and downward flows, and the uncertainty of ignoring unsaturated zone processes. Constantz et al. (2003 [DIRS 177344], pp. 20 to 22) used temperature profiles to estimate percolation rates for two boreholes (WT-2 and H-3) at the Yucca Mountain site through one-dimensional numerical models. They provided a detailed discussion on the relation between temperature gradient and fluid and heat flow processes at the site. They also investigated the effects of uncertainties in ground-surface temperatures and thermal conductivity on estimates of percolation rate. The infiltration rates for the location of boreholes WT-24 and H-3 of the 10th percentile present-day infiltration map are 2.36 and 6.25 mm/yr, respectively. The case 3 of Constantz et al. (2003 [DIRS 177344], p. 22), which determined parameters jointly at both boreholes and are closest to the three-dimensional model representation, estimated the range of percolation flux from 3.4 to 7.3 mm/yr for WT-24 and 5.5 to 13.3 mm/yr for H-3. The estimates in the current ambient thermal model are in the ranges computed by their approach. The uncertainties from temperature measurement have relatively less impact on the modeling results. The surface measurements are difficult to assess because of the variation in surface temperatures with time. However, temperatures become stable over time about 20-m below the surface, which constrains the surface temperatures. Based on the near-surface temperatures, the standard deviation in surface temperature is estimated to be about 0.1ºC. Water table temperatures are not as well constrained by the temperature data used for calibration of surface water flux because temperature measurements were not recorded near the water table in these boreholes. Based on other borehole temperature measurements in the region, the standard deviation in water temperature is estimated to be about 1ºC. Borehole temperature measurements are uncertain by as much as 0.5ºC (Sass et al. 1988, p. 85 and Figure 2-15), although the data suggest that such large uncertainties did not occur for the boreholes used for calibration. Temperature measurements at different times found variations less than 0.1ºC at depths below 20 m. The uncertainty in thermal conductivity is generally less than 15% (BSC 2004 [DIRS 169854], Table 6-7; BSC 2004 [DIRS 170033], Table 6-13).

The effects of thermal conductivity may be estimated from the analytical solution using a homogeneous thermal diffusivity of 4×10^{-7} m^2/s and considering 15% variations. This calculation uses a depth of 600 m and percolation flux rates of 10 mm/yr and 30 mm/yr. The temperature sensitivity is greatest at 300 m because of the fixed boundary temperatures at the surface and the water table. Using a water table temperature of 31ºC and a surface temperature of 17ºC, the temperature variations at 300 m depth caused by 15% variations in thermal diffusivity

system than one-dimensional or two-dimensional calibrations. This information is particularly useful for modeling studies of thermal loading, gas flow and transport of gaseous phase radionuclides for the site (Ahlers et al. 1999 [DIRS 109715]; Wu et al. 2006 [DIRS 180289]). The current model only investigates the 10% and 30% infiltration scenarios. The 50% and 90% infiltration scenarios are considered to be less realistic present-day infiltration maps than the 10% and 30%, based on geochemical and other evidences found at Yucca Mountain. Therefore, the parameters obtained from the calibration based on those 50% and 90% infiltration data would be of little significance in terms of reflecting the real parameters of the rocks at the site.

6.4.1 Calibration Approaches

The three-dimensional UZ models were manually calibrated against pneumatic pressure measurements at two representative boreholes, UZ-7a and SD-12. Among them, UZ-7a represents the boreholes located within major fault zones, whereas SD-12 represents the boreholes that are significantly distant from any major faults. Table 6.4-1 lists the sensors and their associated information of both boreholes.

Table 6.4-1. Observation Sensors and Associated Information of Boreholes UZ-7a and SD-12, used in the Pneumatic Calibration

Sensor Elevation (m)	Hosting Rock	File for Observation data	Date Range	Corresponding Observation Grid Cells
Borehole UZ-7a[1]				
1243.0	tcw12	Uz7a1343.prn	12/1/95 to 1/29/96	ANd70
1232.3	tcw13	Uz7a1337.prn	12/1/95 to 1/29/96	ANd76
1221.6	ptn24	Uz7a1331.prn	12/1/95 to 1/29/96	ANd84
1213.4	ptn26	Uz7a1325.prn	12/1/95 to 1/29/96	ANd86
1177.8	tsw32	Uz7a1319.prn	12/1/95 to 1/29/96	ANd92
Borehole USW SD-12[2]				
1258.5	tcw12	Sd12_214_PT1679.txt	12/1/95 to 1/29/96	ANA18
1232.0	ptn26	Sd12_301_PT1667.txt	12/1/95 to 1/29/96	ANA28
1217.1	tsw32	Sd12_350_PT1661.txt	12/1/95 to 1/29/96	ANA32
1001.3	tsw35	Sd12_1058_PT1619.txt	12/1/95 to 1/29/96	ANA50

Sources: DTNs: [1]LB0612MTSCHPFT.001 [DIRS 180296], [2]LB0612MTSCHP50.001 [DIRS 180294].

NOTE: The first 30 days of the data set were used for calibration, whereas the second 30 days of the data set were used for validation (see Section 7.4).

The parameter sets obtained from the one-dimensional/two-dimensional calibration (DTN: LB0612MTSCHPFT.001 [DIRS 180296]) were the basis (or starting point) of the three-dimensional calibration, which takes the following steps:

1. Calculate the three-dimensional steady state flow field of the UZ for the given infiltration scenario using EOS3 module of TOUGH2 V1.6 (2003 [DIRS 161491]).

2. Create the time-dependent gas-pressure boundary conditions at every top boundary cell (land surface cells) by scaling, using the routine TBgas3D V2.0 (2002 [DIRS 160107]), the observed atmospheric barometric pressure data (DTN: LB0302AMRU0035.001 [DIRS 162378]) with the steady-state gas pressures obtained in Step 1.

3. Simulate one-year, three-dimensional gas flow of the unsaturated zone (ignoring liquid flow) with response to the boundary conditions created in Step 2 and save the simulated pneumatic responses in the observation grid cells;

4. Visually compare the simulated pneumatic pressures with the observed data of the first 30 days (12/01/1996 to 12/30/1996) and determine if an acceptable match between the simulated and the observed data has been obtained;

5. If an acceptable match has not been obtained, modify the fracture permeability of the responsible layers and go to Step 1 to start another iteration of calibration. Otherwise, finish the calibration.

In addition, the numerical mesh and other conditions used in the three-dimensional modeling are described below:

The three-dimensional mesh used in this gas flow simulation is the same three-dimensional thermal grid mesh (Figure 6.3-1) used for the thermal simulation. (The mesh is described in Section 6.3 above). The grid domain covers approximately 20 km^2 of the area, which is smaller than the TSPA-LA grid (Figure 6.1-1). Similar to the TSPA-LA grid, this grid also uses a finer mesh in the vicinity of the repository area.

The bottom water table boundary is treated as a Dirichlet-type boundary. The gas pressure conditions at the bottom boundary are determined based on measured pressures for boreholes USW SD-7 and SD-12 (DTNs: LB991091233129.001 [DIRS 125868]; LB0303GASFLW3D.001 [DIRS 180351]). All lateral boundaries are treated as no-flow boundaries.

In the time-dependent gas-flow simulation (Step 3), the liquid phase flow was neglected to save simulation time without losing much gas-flow accuracy. The impact of liquid-phase flow on the gas flow system is small for gas-flow simulation results, mainly because of the very dry conditions found in the unsaturated zone. It was found that the single-phase (gas) and two-phase (water and gas) flow simulations produce almost identical results in calculated gas pressures. The gas-flow-only condition in the simulation is realized by forcing the relative-permeability of liquid phase to equal 0 (using the linear relative permeability function and choosing appropriate parameters).

6.4.2 Calibration of the UZ Model for the Scenario of the 10-Percentile Infiltration Map

This calibration starts with the one-dimensional/two-dimensional (fault zone) calibrated mountain-scale fracture permeability set, the matrix permeability, matrix van Genuchten alpha, fracture van Genuchten alpha, and active fracture model gamma (DTN: LB0612MTSCHPFT.001 [DIRS 180296]) corresponding to the 10-percentile infiltration map (DTN: SN0609T0502206.028 [DIRS 178753]). Following the steps described in Section 6.4.1, the fracture permeability of some geological layers needs to be adjusted (Table 6.4-2) to match the observed pneumatic data in borehole SD-12. The smaller fracture permeability in TSw units obtained in the three-dimensional calibration, compared with the one-dimensional/two-dimensional (fault zone) calibration results, reflects the significant lateral gas flow through the intensively fractured TSw units from the major faults to the

observation sensors in borehole SD-12. Such three-dimensional gas flow features cannot be captured by any one-dimensional model. As a result, the one-dimensional calibration has to raise the fracture permeability in the TSw unit artificially to compensate for the effects of missing the lateral gas flow in the model. On the other hand, the pneumatic responses to the surface-barometer pressure fluctuations in the fault zone are mainly (if not solely) controlled by the fast vertical gas flow within the zone, and the fracture permeability of normal rocks (outside of fault zones) has little effect on them. These features have already been captured by the parameters obtained from the two-dimensional (fault zone) calibration. Therefore, the match for borehole UZ-7a, which is located within the fault zone, is always good, as expected. Figures 6.4-1 and 6.4-2 show the calibrated model responses against the observed pneumatic pressure responses at several depths in boreholes UZ-7a and SD-12, respectively. Overall, the calibrated model reproduced the pattern variations observed in the pneumatic responses very well.

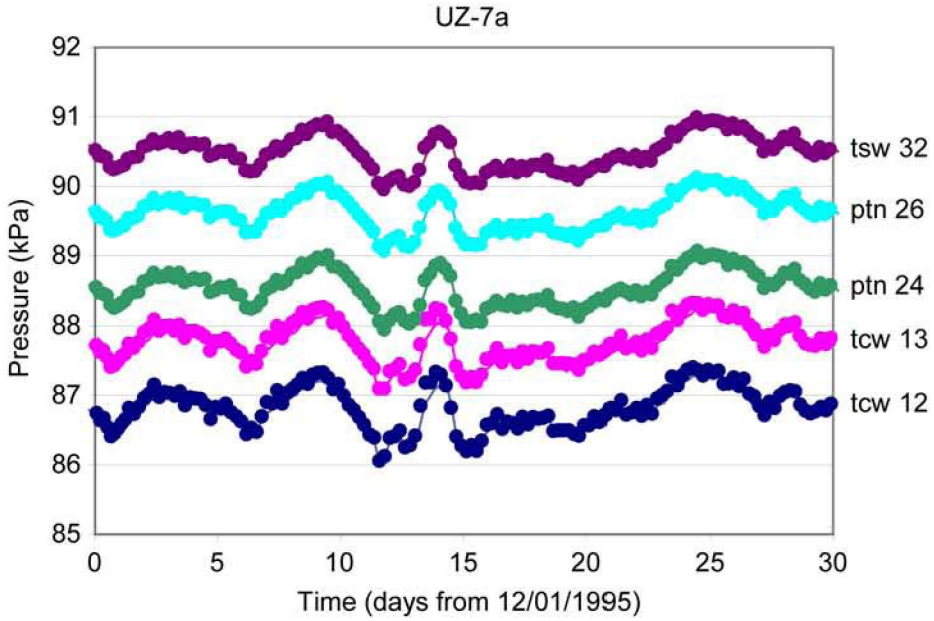

Output DTN: LB07043DGASCAL.001.

NOTE: The hydrogeologic units shown on the figure (e.g., tcw12) are determined from a comparison of the borehole location and measurement depth with the spatial data for the hydrogeolgic units available from the UZ model grid. Both observations and simulations have been vertically offset for clear display. Note the observed data from DTN: LB0612MTSCHPFT.001 [DIRS 180296].

Figure 6.4-1. Comparison of Simulated (solid line) and Observed (solid dots) Gas Pressures at Borehole UZ-7a during the First 30-Day Period

Table 6.4-2. Changes In Fracture Permeability Because of Three-dimensional Calibration (10% Scenario)

Rock	One-dimensional Calibrated Fracture Permeability (m^2)	Three-dimensional Calibrated Fracture Permeability (m^2)
tcw11	1.0000×10^{-12}	2.0000×10^{-12}
tsw31	8.1280×10^{-11}	4.0640×10^{-12}
tsw32	7.0790×10^{-11}	3.5395×10^{-12}
tsw33	7.7620×10^{-11}	3.8810×10^{-12}
tsw34	3.3100×10^{-11}	3.3110×10^{-12}
tsw35	9.1200×10^{-11}	9.1200×10^{-12}
tsw36	1.3490×10^{-10}	1.3490×10^{-11}
tsw37	1.3490×10^{-10}	1.3490×10^{-11}

Output DTN: LB07043DGASCAL.001.

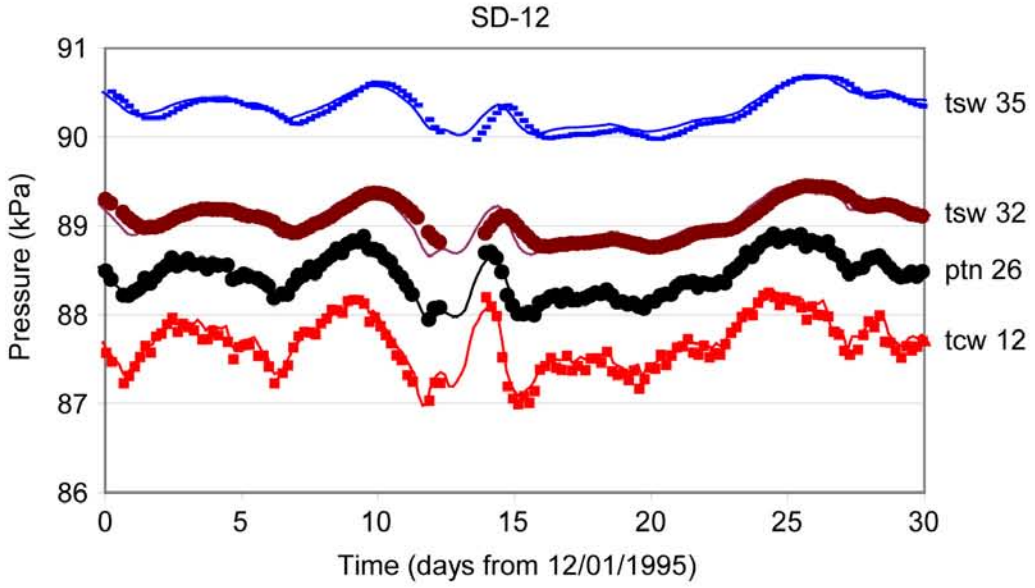

Output DTN: LB07043DGASCAL.001.

NOTE: The hydrogeologic units shown on the figure (e.g., tcw12) are determined from a comparison of the borehole location and measurement depth with the spatial data for the hydrogeolgic units available from the UZ model grid. Both observations and simulations have been vertically offset for clear display. Note the observed data from DTN: LB0612MTSCHPFT.001 [DIRS 180296].

Figure 6.4-2. Comparison of Simulated (solid line) and Observed (solid dots) Gas Pressures at Borehole SD-12 during the First 30-Day Period

6.4.3 Calibration of the UZ Model for 30-Percentile Infiltration Map

This calibration follows the same steps as used for the 10th-percentile case. The initial guess of the fracture permeability and other rock properties come from the one-dimensional/ two-dimensional (fault zone) calibrated mountain-scale fracture permeability set and the matrix permeability, matrix van Genuchten alpha, fracture van Genuchten alpha, and active fracture model gamma (DTN: LB0612MTSCHPFT.001 [DIRS 180296]) corresponding to the 30-percentile infiltration map (DTN: SN0609T0502206.028 [DIRS 178753]). Similar to the 10-percentile case, the match for borehole UZ-7a is always good, but the fracture permeability of some geological layers needs to be adjusted (Table 6.4-3) to match the observed pneumatic data in borehole SD-12. Similarly to the situation of the 10th-percentile infiltration case, the smaller fracture permeability in TSw units obtained in the three-dimensional calibration, compared with the one-dimensional / two-dimensional (fault zone) calibration results, reflects the significant lateral gas flow through the intensively fractured TSw units from the major faults to the observation sensors in borehole SD-12. Such three-dimensional gas flow features cannot be captured by any one-dimensional model. As a result, the one-dimensional calibration has to raise the fracture permeability in the TSw unit artificially to compensate the effects of missing the lateral gas-flow in the model. On the other hand, the pneumatic responses to the surface-barometer-pressure fluctuations in the fault zone are mainly (if not solely) controlled by the fast vertical gas flow within the zone and are virtually unaffected by the fracture permeability of normal rock (outside fault zones). These features have already been captured by the parameters obtained from the two-dimensional (fault zone) calibration. Therefore, the match for borehole UZ-7a, located within the fault zone, is always good, as expected. Figures 6.4-3 and 6.4-4 show the calibrated model responses against the observed pneumatic pressure responses at several depths in boreholes UZ-7a and SD-12, respectively. Note that the tcw11 is no longer in the change list for this 30th-percentile case. Overall, the calibrated model reproduced the pattern variations observed in the pneumatic responses very well (Figure 6.4-3 and Figure 6.4-4).

Table 6.4-3. Modifications to Fracture Permeability Resulting from Three-Dimensional Calibration (30% scenario)

Rock	One-dimensional Calibrated Fracture Permeability (m^2)	Three-dimensional Calibrated Fracture Permeability (m^2)
tsw31	8.1280×10^{-11}	1.6256×10^{-12}
tsw32	7.0790×10^{-11}	1.4158×10^{-12}
tsw33	7.7620×10^{-11}	1.5524×10^{-12}
tsw34	3.3110×10^{-11}	3.3110×10^{-12}
tsw35	9.1200×10^{-11}	9.1200×10^{-12}
tsw36	1.3490×10^{-10}	1.3490×10^{-11}
tsw37	1.3490×10^{-10}	1.3490×10^{-11}

Output DTN: LB07043DGASCAL.001.

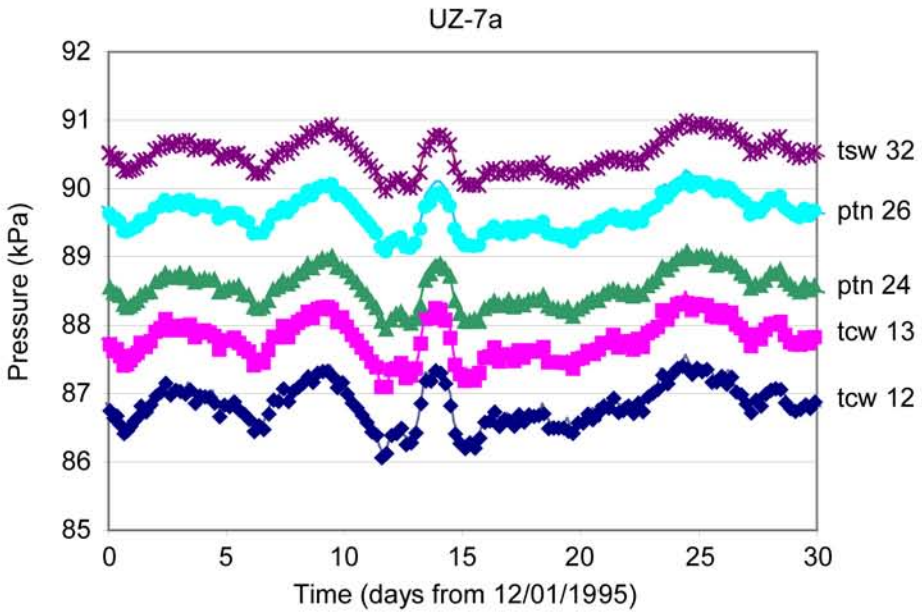

Output DTN: LB07043DGASCAL.001.

NOTE: The hydrogeologic units shown on the figure (e.g., tcw12) are determined from a comparison of the borehole location and measurement depth with the spatial data for the hydrogeolgic units available from the UZ model grid. Both observations and simulations have been vertically offset for clear display. The observed data is from DTN: LB0612MTSCHPFT.001 [DIRS 180296].

Figure 6.4-3. Comparison of Simulated (solid line) and Observed (solid dots) Gas Pressures at Borehole UZ-7a during the First 30-day Period

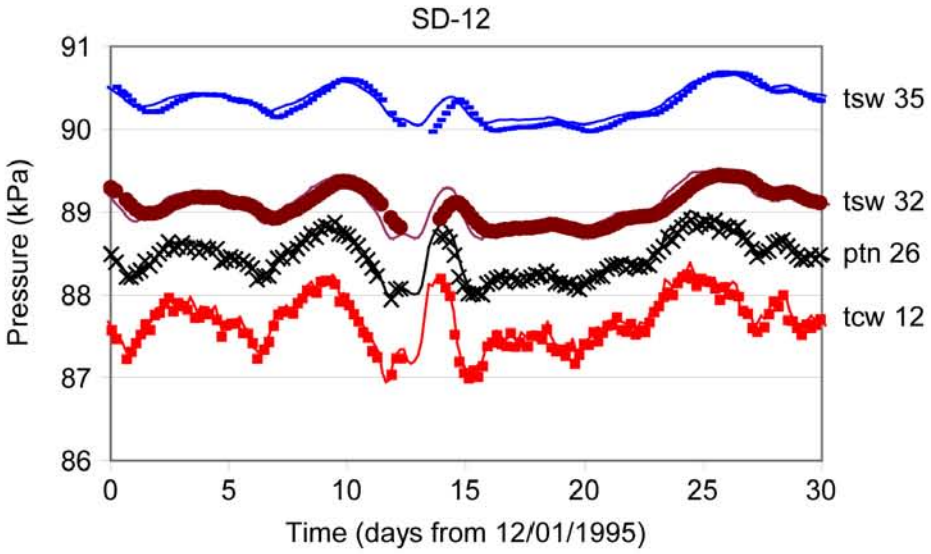

Output DTN: LB07043DGASCAL.001.

NOTE: The hydrogeologic units shown on the figure (e.g., tcw12) are determined from a comparison of the borehole location and measurement depth with the spatial data for the hydrogeolgic units available from the UZ model grid. Both observations and simulations have been vertically offset for clear display. The observed data is from DTN: LB0612MTSCHPFT.001 [DIRS 180296].

Figure 6.4-4. Comparison of Simulated (solid line) and Observed (solid dots) Gas Pressures at Borehole SD-12 during the First 30-day Period

6.5 ANALYSIS AND MODELING OF PORE-WATER CHLORIDE DATA

This study consists of modeling and analyzing geochemical data in the Yucca Mountain unsaturated zone. It utilizes geochemical models to evaluate the hydrological systems, through assessing spatial distribution of surface net infiltration and the impact of variations on its magnitude. It is part of the model calibration effort to support the conceptual model of UZ flow and to build confidence in the predictive capability of the model.

Geochemical data provide additional information by which to analyze the unsaturated zone system. Solutes can be transferred from the atmosphere to the ground surface by precipitation and dry deposition. The chemistry of rain water undergoes drastic changes as it comes in to contact with the earth surface. The distribution of chemical constituents within both liquid and solid phases of the unsaturated zone system depends on such factors as hydrological and geochemical processes of surface precipitation and evapotranspiration, the fracture–matrix interaction of flow and transport, large-scale mixing via lateral transport, and the history of climate changes and recharge. The premise for using chloride for the calibration is that chloride is a conservative species. Evaporation of water leaves chloride behind, and chloride does not interact with other minerals. Chloride in samples from Yucca Mountain has four main sources: (1) salts or fluids present in fractures; (2) salts or fluids present in intergranular pores; (3) isolated fluid inclusions within mineral grains; and (4) chemically bound chloride in hydrous minerals such as biotite and hornblende (Lu et al. 2003 [DIRS 168915]). Chloride from the above sources (3) and (4) is not believed to contribute to the pore-water chloride, because in those cases it is trapped within the mineral grain.

Chloride distribution in the unsaturated zone groundwater provides important information for UZ model calibration and validation. Pore-water chloride concentration data are used in this section to calibrate the UZ model and to bound the infiltration flux, flow pathways, and transport time. These concentration data are analyzed and modeled by three-dimensional chemical transport simulations, using a dual-permeability modeling approach. (UZ flow models of this chloride transport use the three-dimensional model property set in Appendix B). Percolation flux strongly depends on infiltration rates and their spatial distribution. The present-day infiltration rate, estimated across the study area, ranges from 3.03 to 26.78 mm/yr, averaged over the UZ model domain (output DTN: LB0706UZWATSAT.001; Table 6.1-2). The climate over the past 100,000 years has been used to estimate the possible range in infiltration rates over the next 10,000 years (Sonnenthal and Bodvarsson 1999 [DIRS 117127]).

The use of present-day flow field and steady-state simulations discounts the possibility of there being a residual impact resulting from higher infiltration rates during the Pleistocene Epoch. Precipitation last reached a maximum around 21 ka. Higher levels of precipitation (compared to the modern climate) lasted for at least another 10,000 years, and at 10,000 years before present may have been 50% higher than the modern precipitation rate (Tyler et al. 1996 DIRS [108774]). In transient simulations of postglacial change in infiltration and chloride fluxes, Sonnenthal and Bodvarsson (1999 [DIRS 117127], Sections 5.7 and 5.8) show that surface concentrations reached their modern values after 10,000 years of modern infiltration and chloride fluxes. Depths that have been reached by the present-day chloride-rich waters vary considerably. Under ridge tops and side slopes, modern waters reached the water table, whereas under regions of very low infiltration, the front of the chloride-rich plume has barely reached the PTn, leaving much of the underlying TSw unaffected. The residual impact of past climates with higher infiltration rates than present-day climate is a concern for the chloride model, because chloride mass from the previous 10,000 years and earlier remains to be washed out of the unsaturated zone. Consequently, the waters in the current unsaturated zone system are a mixture of two end members—very old water and recent infiltrated water. Given a linear mixing, current chloride concentration of pore water represents an intermediate value between the concentrations of the two end-members. Since a higher infiltration rate in the distant past corresponds to an end member with low pore-water concentration, the other end member must represent a pore-water concentration higher than current measurement values. In other words, current field-measured chloride concentration has been affected by old water residing in the unsaturated zone, leading to a lower concentration than the case would have without the residual old water. As a result, the infiltration rate calibrated using field-measured chloride data results in wetter climate—corresponding to a conservative, higher infiltration rate for the present-day climate.

6.5.1 Available Data

6.5.1.1 Pore-Water Chemical Concentration Data

Chloride transport processes were modeled as part of this model analysis. The chloride concentrations used in the modeling were measured from pore waters extracted from field samples, collected from a total of twelve surface-based boreholes, the ESF, and the ECRB. (The boreholes were SD-6, SD-7, SD-9, SD-12, NRG-6, NGR-7a, UZ-14, UZ#16, UZ-7a, WT-24, G-2, and UZ-N55. Data sources for each borehole are listed in Table 6.5-1.)

Table 6.5-1. Chloride Data Sources

Boreholes/Facilities	DTN
SD-6	GS981008312272.004 [DIRS 153677] A LA0002JF12213U.001 [DIRS 154760] B
SD-7	GS000608312271.001 [DIRS 153407] C GS970908312271.003 [DIRS 111467] D GS961108312271.002 [DIRS 121708] F GS981008312272.004 [DIRS 153677] A LA0002JF12213U.001 [DIRS 154760] B LAJF831222AQ98.011 [DIRS 145402] H
SD-9	GS970908312271.003 [DIRS 111467] D GS961108312271.002 [DIRS 121708] F LA0002JF12213U.001 [DIRS 154760] B LAJF831222AQ98.011 [DIRS 145402] H HGS020408312272.003 [DIRS 160899] O
SD-12	GS000608312271.001 [DIRS 153407] C GS970908312271.003 [DIRS 111467] D GS961108312271.002 [DIRS 121708] F GS981008312272.004 [DIRS 153677] A LA0002JF12213U.001 [DIRS 154760] B
NRG-6	GS010708312272.002 [DIRS 156375] I LA0002JF12213U.001 [DIRS 154760] B LAJF831222AQ98.011 [DIRS 145402] H
NRG-7a	GS961108312271.002 [DIRS 121708] F GS981008312272.004 [DIRS 153677] A GS010708312272.002 [DIRS 156375] I LA0002JF12213U.001 [DIRS 154760] B LAJF831222AQ98.011 [DIRS 145402] H GS020408312272.003 [DIRS 160899] O
UZ-14	GS010708312272.002 [DIRS 156375] I GS961108312271.002 [DIRS 121708] F GS990208312272.001 [DIRS 146134] J LA0002JF12213U.001 [DIRS 154760] B LAJF831222AQ98.011 [DIRS 145402] H
UZ#16	GS010708312272.002 [DIRS 156375] I GS990208312272.001 [DIRS 146134] J LA0002JF12213U.001 [DIRS 154760] B LAJF831222AQ98.011 [DIRS 145402] H
UZ-N55	LA0002JF12213U.001 [DIRS 154760] B GS010708312272.002 [DIRS 156375] I
UZ-7a	GS981008312272.004 [DIRS 153677] A LA0002JF12213U.001 [DIRS 154760] B
WT-24	GS981008312272.004 [DIRS 153677] A LA0002JF12213U.001 [DIRS 154760] B LAJF831222AQ98.011 [DIRS 145402] H
G-2	LAJF831222AQ98.011 [DIRS 145402] H
ECRB	LA9909JF831222.004 [DIRS 145598] K LA0002JF12213U.002 [DIRS 156281] L GS020408312272.003 [DIRS 160899] O

Table 6.5-1. Chloride Data Sources (Continued)

Boreholes/Facilities	DTN
ESF	GS961108312261.006 [DIRS 107293] M LA0002JF12213U.002 [DIRS 156281] L LA9909JF831222.010 [DIRS 122733] N

NOTE: Letters following the DIRS numbers are not a part of the DTN number. Each letter corresponds to the appearance of the same DTN.

6.5.1.2 Chloride Flux

Sources contributing to the chloride flux in recharge waters are precipitation, run-on, and runoff. The portion of these waters that form net infiltration is small. Infiltration rates for present-day climate scenarios are estimated to be in the range of 3.03 to 26.78 mm/yr, based on the average infiltration rates for the 10th and 90th percentile infiltration maps (Table 6.1-2). The present-day mean infiltration rate estimated from the chloride data is approximately 5 mm/yr, and the glacial maximum infiltration rate at 21,000 years ago was about 28 mm/yr (Sonnenthal and Bodvarsson 1999 [DIRS 117127], p. 148, Figure 23).

Four case studies corresponding to four present-day climate scenarios were chosen. They represent the 10th, 30th, 50th, and 90th percentile infiltration maps. Their mean fluxes are listed in Table 6.5-2, calculated from four infiltration maps (DTN: SN0609T0502206.028 [DIRS 178753]). Also listed in the table are the notations for these infiltration scenarios, which are consistent with the notations used in the flow models (Section 6.2). The chloride transport model uses the same flow model as the notation indicates. Chloride recharge fluxes to these transport models are calculated accordingly for these climate scenarios.

Chloride recharge sources into the saturated zone include dissolved material in rain, particulates in snow, and a contribution from windblown dust (Tyler et al. 1996 [DIRS 108774]). Also, precipitate on land surfaces would experience physical processes such as evaporation, which leaves behind Cl^- in the remaining water. The chloride mass flux to the chloride transport model depends on the amount of water flux and its chloride concentration. In the model, fluxes are considered to be precipitation, runon, and runoff. Thus, the water fluxes contributing to chloride recharge can be calculated using the following equation:

$$F = F_{prec} + F_{runon} - F_{runoff} \quad \text{(Eq. 6.5-1)}$$

where F is the net flux contributing to the chloride in the recharging water (defined as net recharge in Table 6.5-2, independent of the net infiltration of Table 6.1-2), F_{prec} is the precipitation flux, F_{runon} is the runon flux, and F_{runoff} is the runoff flux. For input to the TOUGH2 calculation the net recharge flux in mm/yr is converted to equivalent mass flux (kg/s). Calculating each term for F is carried out using the routine infil2grid V1.7 (2002 [DIRS 154793]) and the precipitation, runoff and runon data for the present-day climate (DTN: SN0609T0502206.028 [DIRS 178753]). Chloride flux is then calculated using the following formula:

$$F_{Cl} = C_{Cl,p} \times 10^{-6} (F_{prec} + F_{runon} - F_{runoff}) \qquad \text{(Eq. 6.5-2)}$$

where F_{Cl} is chloride flux (kg/s), F_{prec} is precipitation flux (kg/s), F_{runon} is run-on (kg/s), and F_{runoff} is runoff flux (kg/s). $C_{Cl,p}$ is chloride concentration in precipitation (mg/(kg water). (Note that actual calculations and procedures using this equation in preparing input files for chloride simulations are summarized in Appendix D2).

Table 6.5-2. Present-Day Chloride Recharge Fluxes and Precipitation, Runon, and Runoff Rates for Different Scenarios (Averaged over Model Domain)

Scenario Notations [a]	Scenarios	Precipitation (mm/yr)	Runon (mm/yr)	Runoff (mm/yr)	Net Recharge Used in Calculation of Chloride Flux [b] (mm/yr)
pd_10	10th Percentile Infiltration Map	163.44	277.00	279.03	161.41
pd_30	30th Percentile Infiltration Map	153.89	600.21	606.09	148.01
pd_50	50th Percentile Infiltration Map	189.68	995.78	1005.62	179.84
pd_90	90th Percentile Infiltration Map	147.05	862.39	871.02	138.43

Source: [a]Fluxes calculated as described in Appendix D, Section D2, data from Output DTN: LB0706UZWATSAT.001]

NOTE: [b]Net water flux contributing to the chloride recharge is calculated by Equation 6.5-1.

Surface chloride concentrations are discussed by Sonnenthal and Bodvarsson (1999 [DIRS 117127], pp. 113 to 114). The range of 0.55 to 0.73 mg/L was considered to bound the average value. Triay et al. (1996 [DIRS 101014]) obtained a mean chloride concentration in precipitation of 0.55 mg/L, which is probably close to the minimum value expected. A similar value was obtained by combining a mean annual precipitation of about 170 mm/yr with a present-day chloride surface flux of 106 mg/(m^2-yr) yielding a mean chloride concentration of about 0.62 mg/L (Fabryka-Martin et al. 1997 [DIRS 100144]), which includes a windblown dust component. The contribution from windblown dust may be 33% of the total chloride flux in the Great Basin of Nevada and Utah (Tyler et al. 1996 [DIRS 108774]). Even though the contribution from windblown dust is considered in the flux, as part of the measured precipitation, the upper limit of concentration can be bounded by adding 33% more chloride to the 0.55 mg/L concentration to yield a maximum of about 0.73 mg/L. The upper limit is less well defined than the lower limit, which is more easily set from the concentrations in precipitation. Clearly, variation in this 0.73 mg/L chloride concentration before evapotranspiration is much less than the over an order-of-magnitude range in estimates of infiltration rate, and therefore the surface chloride concentration is a moderately well-constrained boundary value for modeling studies (Sonnenthal and Bodvarsson (1999 [DIRS 117127], pp. 113 to 114). A value of 0.55 mg/L (Sonnenthal and Bodvarsson 1999 [DIRS 117127]; Triay et al. 1996 [DIRS 101014]) is used in the present simulations, and applied to all infiltrating water in the form of precipitation, run-on, and runoff (Sonnenthal and Bodvarsson 1999 [DIRS 117127], p. 148). The concentration of recharge water is factored into the above equation as a linear coefficient in the chloride flux

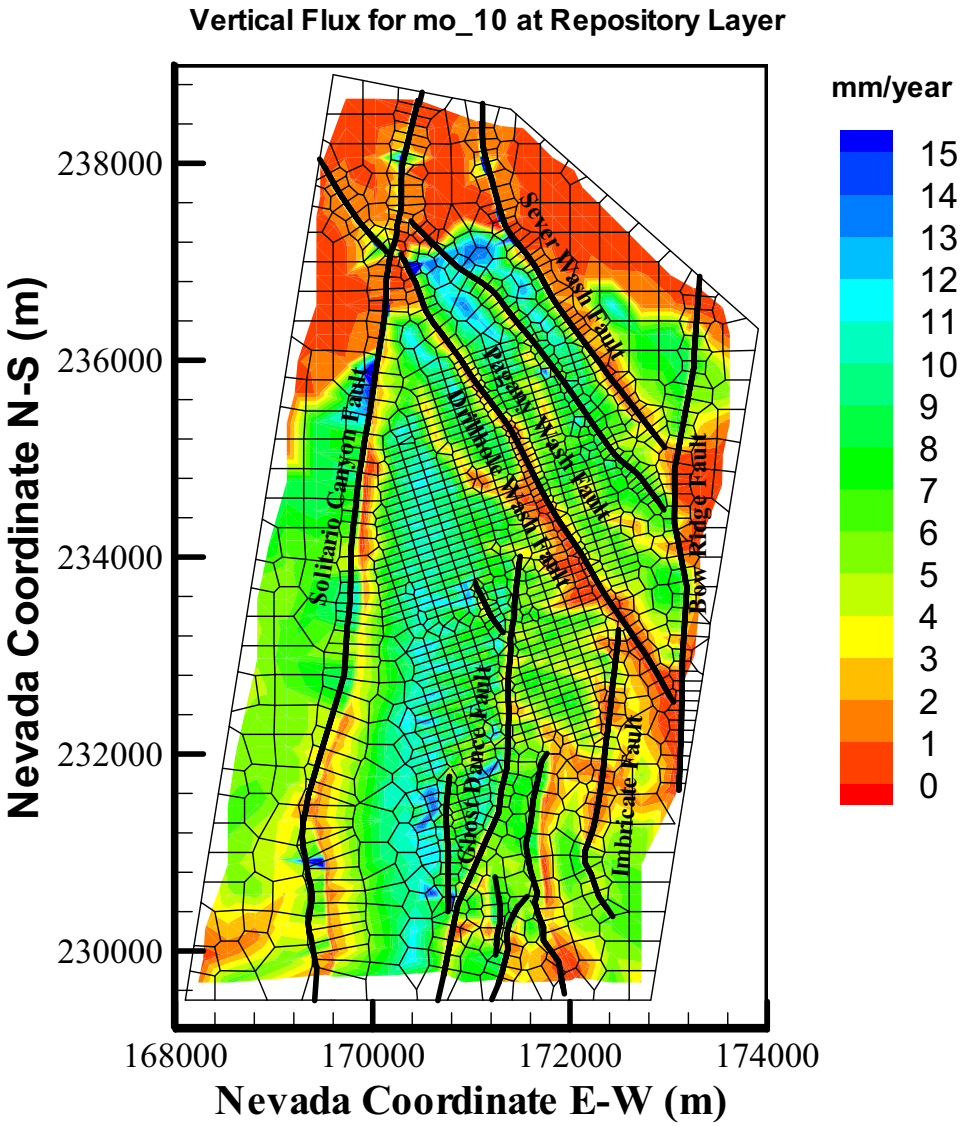

Output DTN: LB07013DMOUZFF.001.

Figure 6.6-2. Simulated Percolation Fluxes at the Repository Horizon under the Monsoon, 10th Percentile Infiltration Scenario

6.6.2.3 Matrix, Fracture, and Fault Flow Components

Tables 6.6-1, 6.6-2, and 6.6-3 list percentages of fracture-matrix flow components for non-fault zones and fault flow over the entire model domain and within the repository footprint at the three horizons of the TCw/PTn interface, the repository layer, and the water table. (In these 3 tables as well as in the rest of the documentation, the accuracy in the value of parameters is one less than the significant digits, as given, because the last significant digits are rounded.) Fracture and matrix percentages are computed for the non-fault zones only (i.e., excluding fault flow), whereas fault flow percentages represent total vertical fracture-matrix flux through fault blocks over the entire model layer or the smaller region of the repository footprint at the three horizons. The three percentages sum to 100%. (Procedures for calculating the percentages are explained in Appendix E.) These statistics are calculated from vertical flow along each grid column, using the sixteen flow fields.

Statistical data as shown in Tables 6.6-1 and 6.6-2 indicate that fracture flow is dominant at both the top of the PTn unit and the repository horizons. At the repository level, fracture flow consists of about 60% to 80% of the total percolation fluxes over the entire model layer, and is mostly higher than 90% within the repository footprint. On the other hand, fault flow increases with depth. Over the entire model layer, fault flow at the TCw/PTn interface is about 1% to ~2%, increasing to 12% to 32% at the repository horizon, and reaching 44% to 65% at the water table (Table 6.6-3). In comparison, fault flow over the smaller area, within the repository footprint, is low, at about 1%, at the TCw/PTN interface and repository horizon, but then increases to 16%–-37% at the bottom boundary, the water table. Comparison of fault flow percentages at the TCw/PTn interface, the repository horizon, and the water table in Tables 6.6-1, 6.6-2, and 6.6-3 indicates that flow focusing into faults occurs mainly through the PTn unit and through the lower hydrogeological CHn unit.

Table 6.6-1. Comparison of the Water Flux through Matrix, Fractures of Non-fault Zones, and Faults as a Percentage of the Total Flux over the Entire Model Domain and within the Repository Footprint at the TCw/PTn Interface for the 16 Flow Fields

Simulation Designation	Flux at TCw/PTn Interface over Entire Model Domain (%)			Flux at TCw/PTn Interface within Repository Footprint (%)		
	Fracture	Matrix	Fault	Fracture	Matrix	Fault
pd_10	98.66	0.04	1.31	99.01	0.04	0.95
pd_30	98.33	0.05	1.62	98.76	0.04	1.20
pd_50	98.54	0.03	1.43	98.81	0.03	1.16
pd_90	98.34	0.05	1.61	98.64	0.04	1.32
mo_10	98.06	0.06	1.87	98.60	0.06	1.35
mo_30	98.13	0.07	1.80	98.61	0.06	1.33
mo_50	98.33	0.06	1.61	98.72	0.05	1.22
mo_90	98.03	0.04	1.93	98.55	0.03	1.42
gt_10	98.30	0.10	1.59	98.69	0.10	1.21
gt_30	98.11	0.11	1.78	98.59	0.10	1.32
gt_50	98.08	0.07	1.84	98.59	0.07	1.34
gt_90	97.99	0.09	1.91	98.50	0.08	1.41
pkd_q1	98.10	0.03	1.87	98.61	0.02	1.37

Table 6.6-1. Comparison of the Water Flux through Matrix, Fractures of Non–fault Zones, and Faults as a Percentage of the Total Flux over the Entire Model Domain and within the Repository Footprint at the TCw/PTn Interface for the 16 Flow Fields (Continued)

Simulation Designation	Flux at TCw/PTn Interface over Entire Model Domain (%)			Flux at TCw/PTn Interface within Repository Footprint (%)		
	Fracture	Matrix	Fault	Fracture	Matrix	Fault
pkd_q2	98.54	0.03	1.43	98.82	0.03	1.16
pkd_q3	98.38	0.03	1.59	98.68	0.02	1.30
pkd_q4	98.02	0.06	1.93	98.53	1.42	1.42

Output DTNs: LB06123DPDUZFF.001; LB07013DMOUZFF.001; LB07013DGTUZFF.001; LB0702UZP10KFF.002; LB0705FLOWCOMP.001.

PTn=Paintbrush nonwelded hydrogeologic unit; TCw=Tiva Canyon welded hydrogeologic unit.

Table 6.6-2. Comparison of the Water Flux through Matrix, Fractures of Non-fault Zones, and Faults as a Percentage of the Total Flux over the Entire Model Domain and within the Repository Footprint at the Repository Level for the 16 Flow Fields

Simulation Designation	Flux at Repository Horizon over Entire Model Domain (%)			Flux at Repository Horizon within Repository Footprint (%)		
	Fracture	Matrix	Fault	Fracture	Matrix	Fault
pd_10	58.42	9.71	31.87	94.20	5.16	0.65
pd_30	67.14	7.90	24.95	95.96	2.73	1.31
pd_50	64.74	7.51	27.75	96.68	2.03	1.28
pd_90	74.04	6.69	19.27	97.76	1.24	1.00
mo_10	71.64	13.26	15.10	91.14	8.00	0.86
mo_30	73.34	9.35	17.31	94.54	4.04	1.42
mo_50	68.18	8.13	23.70	95.11	3.55	1.34
mo_90	79.63	6.33	14.04	97.89	1.03	1.08
gt_10	64.63	17.49	17.88	86.90	12.31	0.79
gt_30	71.33	10.27	18.40	93.50	5.05	1.45
gt_50	71.29	9.12	19.59	94.14	4.43	1.42
gt_90	78.97	7.43	13.60	96.95	2.06	0.99
Pkd_q1	79.14	9.02	11.84	95.79	3.32	0.89
Pkd_q2	65.34	7.24	27.42	96.88	1.84	1.29
pkd_q3	72.36	6.93	20.71	97.09	1.49	1.42
pkd_q4	79.40	6.71	13.89	97.58	1.37	1.05

Output DTNs: LB06123DPDUZFF.001; LB07013DMOUZFF.001; LB07013DGTUZFF.001; LB0702UZP10KFF.002; LB0705FLOWCOMP.001.

Table 6.6-3. Comparison of the Water Flux through Matrix, Fractures of Non-fault Zones, and Faults as a Percentage of the Total Flux over the Entire Model Domain and within the Repository Footprint at the Water Table for the 16 Flow Fields

Simulation Designation	Flux at Water Table over Entire Model Domain (%)			Flux at Water Table within Repository Footprint (%)		
	Fracture	Matrix	Fault	Fracture	Matrix	Fault
pd_10	20.24	14.40	65.36	54.21	23.53	22.26
pd_30	25.56	12.78	61.66	50.58	16.50	32.92
pd_50	22.35	12.72	64.92	47.26	15.70	37.04
pd_90	28.72	7.09	64.19	57.97	5.95	36.08
mo_10	29.13	21.71	49.16	52.90	26.63	20.47
mo_30	31.25	14.83	53.91	51.38	15.93	32.69
mo_50	25.99	15.39	58.62	48.80	17.10	34.10
mo_90	29.17	8.17	62.66	58.42	5.94	35.64
gt_10	30.35	25.98	43.68	51.55	32.52	15.93
gt_30	34.57	15.44	49.99	52.30	16.85	30.85
gt_50	28.42	17.01	54.56	49.21	17.60	33.19
gt_90	31.31	10.58	58.11	57.61	7.71	34.68
pkd_q1	26.18	18.84	54.98	56.95	19.96	23.09
pkd_q2	22.84	11.93	65.23	50.42	16.87	32.70
pkd_q3	23.50	14.01	62.50	47.89	15.10	37.01
pkd_q4	29.88	8.95	61.17	58.55	6.26	35.18

Output DTNs: LB06123DPDUZFF.001; LB07013DMOUZFF.001; LB07013DGTUZFF.001; LB0702UZP10KFF.002; LB0705FLOWCOMP.001.

6.6.2.4 Distributions of Percolation Fluxes within the Repository Footprint

Percolation fluxes at the repository horizon and within the repository footprint can be further analyzed using a frequency distribution plot. This plot displays the averaged percentage of the repository area subject to a particular percolation rate. Note that the normalized flux rates are determined by normalizing an infiltration value with respect to the averaged infiltration rate for the scenario. For example, "1" stands for the normalized flux rate corresponds to 3.03, 6.74, 11.03, and 16.89 mm/yr (Tables 6.1-2 and 6.1-3), respectively, for the four 10th percentile infiltration scenarios. The information, as shown in Figures 6.6-9, 6.6-10, 6.6-11, and 6.6-12 (see Appendix E for calculation details), is important to drift-scale modeling studies of flow and transport at drifts and flow-redistributing phenomena through the TSw. Figures 6.6-9 to 6.6-12 show the frequency distribution of normalized percolation flux within the repository horizon for the four 10th percentile infiltration rates of the four climates.

Figures 6.6-9 to 6.6-12 indicate that the highest flux frequencies, occurring at 14% to 24%, have normalized fluxes of about 1.2 to 1.5, except for the case of the glacial transition 10th percentile infiltration (gt_10), which has the highest frequency flux at the lowest range of normalized fluxes. In general, the areas with normalized percolation fluxes greater than 3 are very small, taking up less than 1% of the total repository area.

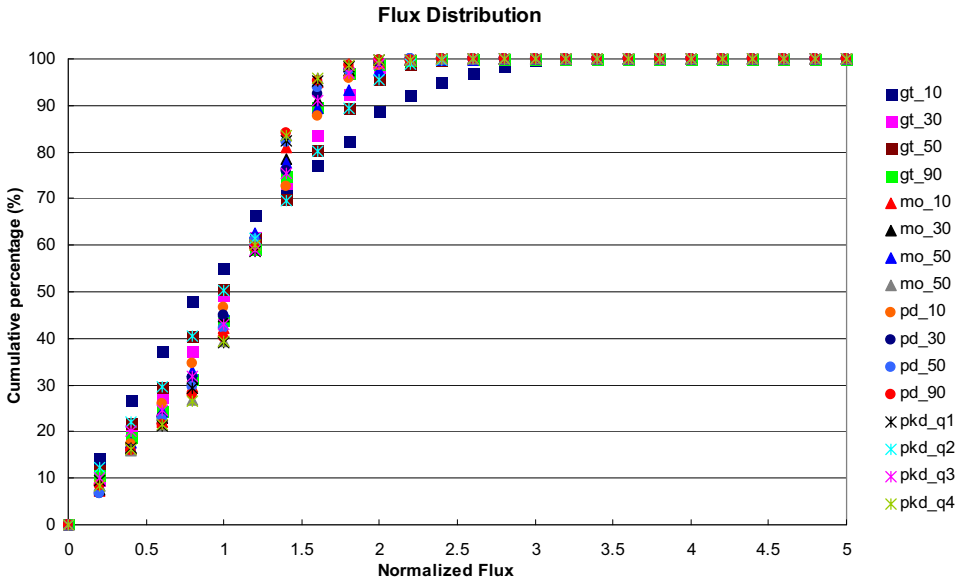

Output DTNs: LB06123DPDUZFF.001; LB07013DMOUZFF.001; LB07013DGTUZFF.001; LB0702UZP10KFF.002.

Figure 6.6-13. Cumulative Flux Distribution and Range as Functions of Normalized Percolation Flux within the Repository from the 16 Flow Fields of Four Climates

6.7 TRACER TRANSPORT TIMES

This section summarizes simulated tracer transport using the 16 UZ flow fields. The results present an evaluation of tracer or radionuclide transport processes from the repository to the water table (saturated zone) within the mountain, including the effects of different infiltration scenarios, advection, diffusion, and adsorption. Tracer-transport studies described in this section provide insight into UZ flow patterns, groundwater travel times, and tracer transport processes.

6.7.1 Methodology and Transport Parameters

Simulation results and analyses in this section are based on transport studies of conservative and reactive tracers, using the T2R3D V1.4 code (1999 [DIRS 146654]). The dual-permeability modeling approach with the three-dimensional TSPA-LA grid (Figure 6.1-1), as discussed in Section 6.1.1, is used in the transport simulations. In the tracer transport modeling, the 16 steady-state, three-dimensional flow fields of Section 6.6 are directly used as input to the T2R3D code for modeling transport from the repository to the water table.

To assess tracer transport times from the repository to the water table, tracers are treated as conservative (nonadsorbing) and reactive (adsorbing) components transported through the unsaturated zone. In both cases, hydrodynamic/mechanical dispersion through the fracture–matrix system is ignored, because sensitivity studies indicate that mechanical dispersion has an insignificant effect on the cumulative breakthrough curves of tracers at the water table (Wu et al. 2002 [DIRS 160195]). A constant molecular diffusion coefficient of 3.2×10^{-11} m^2/s is used for matrix diffusion of the conservative component, and 1.6×10^{-10} m^2/s is used for the

reactive component. Note that the non-reactive component is used to represent a radionuclide, which typically has a small diffusion coefficient due to heavy molecular weight and large size. The range of matrix diffusion coefficients is close to the values of typical diffusion coefficients for ions, anions and cations. For example, the diffusion coefficients of ions typically range from 3.0×10^{-10} to 20.0×10^{-10} m^2/s (Langmuir 1997 [DIRS 100051], p. 65), which summarizes that those of anions ($4.14 \times 10^{-10} – 52.7 \times 10^{-10}$ m^2/s) and cations ($1.53 \times 10^{-10} – 93.1 \times 10^{-10}$ m^2/s) (Lerman 1979 [DIRS 182304], Section 3.2, Table 3.1).

The two diffusion coefficients are multiplied by porosity and tortuosity in the simulation to account for various units. In the case of a reactive or adsorbing tracer, several K_d values are used, as given in Table 6.7-1, for different units. These values were selected to approximate those for neptunium (^{237}Np) transport (DTNs: LA0010JC831341.001 [DIRS 162476]; LA0010JC831341.002 [DIRS 153321]; LA0010JC831341.003 [DIRS 153322]; LA0010JC831341.004 [DIRS 153323]; LA0010JC831341.005 [DIRS 153320]; LA0010JC831341.006 [DIRS 153318]; LA0010JC831341.007 [DIRS 153319]). For a conservative tracer, K_d is set to zero. These molecular diffusion coefficients and K_d values are selected to represent technetium and neptunium. Model parameters such as porosity and rock grain density were taken from the matrix and thermal properties (DTNs: LB0207REVUZPRP.002 [DIRS 159672]; LB0210THRMLPRP.001 [DIRS 160799]).

Transport simulations were conducted for 1,000,000 years using 16 infiltration rates of four climates. At the start of each simulation, an initial, constant concentration source was instantaneously released from the fracture continuum gridblocks representing the repository.

Table 6.7-1. K_d Values Used for Reactive Tracer Transport in Different Hydrogeologic Units

Hydrogeologic Unit	K_d (cc/g)
Zeolitic matrix in CHn	4.0
Vitric matrix in CHn	1.0
Matrix in TSw	1.0
Fault matrix in CHn	1.0
Fractures and the matrix in the rest of units	0.0

Sources: DTNs:
LA0010JC831341.001 [DIRS 162476], LA0010JC831341.002 [DIRS 153321], LA0010JC831341.003 [DIRS 153322], LA0010JC831341.004 [DIRS 153323], LA0010JC831341.005 [DIRS 153320], LA0010JC831341.006 [DIRS 153318], and LA0010JC831341.007 [DIRS 153319].
CHn = Calico Hills nonwelded hydrogeologic unit; TSw = Topopah Spring welded hydrogeologic unit.

6.7.2 Simulation Scenarios

For each flow simulation, as listed in Table 6.2-6, there are two transport runs, one for conservative (tc_*) and one for reactive (np_*) tracer transport. Table 6.7-2 summarize a total of 16 × 2 tracer-fracture-release simulation scenarios, corresponding to the 16 UZ flow fields for the 16 infiltration maps of four climates, respectively.

transport times with different infiltration rates and types of tracers considered in the 32 simulations (listed in Table 6.7-2).

As indicated by Figures 6.7-1 and 6.7-2, the predominant factors in controlling tracer transport are (1) surface-infiltration rates or net water recharge and (2) adsorption effects (i.e., whether the tracer is conservative or reactive). Statistics of tracer transport times for 10% and 50% mass breakthrough at the water table for the 32 simulation scenarios are given in Table 6.7-3. Figure 6.7-3 correlates average infiltration rates and tracer transport times at 50% mass breakthrough for the 32 simulation scenarios. Figures 6.7-1, 6.7-2, 6.7-3, and the statistical data of Table 6.7-3 show the following:

- Tracer transport times vary inversely to the average surface infiltration (net water recharge) rate over the model domain (Figure 6.7-3). When the average infiltration rate increases from 3 to 70 mm/yr, average tracer transport (50% breakthrough) times decrease by more than two orders of magnitude for both adsorbing and nonadsorbing species.

- Nonadsorbing tracers migrate (from the repository to the water table) one to two orders of magnitude faster than an adsorbing tracer under the same infiltration condition (Figure 6.7-3).

6.8.3 Temperature and Chloride Data

In the Yucca Mountain unsaturated zone, the temperature profiles or geothermal gradients of the unsaturated zone system are controlled by several factors, such as formation thermal conductivity and net infiltration rates, in addition to the regional weather conditions or surface temperatures. Because of the small impact of uncertainties in measured thermal conductivities on simulated heat flow, the temperature profile can be used to constrain infiltration maps and determine weighting factors. There are total of five boreholes containing qualified temperature data: NRG-6, NRG-7a, SD-12, UZ#5, and UZ-7a. The borehole locations can be found in Figure 6.1-1. Simulated temperature distributions at these five boreholes were generated from the four infiltration maps, as described in Section 6.3 (Output DTN: LB0701UZMTHCAL.001). Near the ground surface in five of the boreholes, observed temperatures show significant seasonal variations. However, these seasonal changes in surface temperature have little impact on steady-state heat flow or temperature profiles in the deeper (more than 20 m) unsaturated zone . In this study, only measurements 40 m below ground surface were considered, resulting in a total of 50 temperature data points for comparison.

In addition to limited temperature measurements, natural chemical tracers can also be used to examine infiltration history. Chloride is considered a nearly ideal natural tracer for the study of water movement in the liquid phase in geological systems. Its measurements are available at two horizontal tunnels, the ECRB and ESF, and twelve vertical boreholes: G-2, NRG-6, NGR-7a, SD-12, SD-6, SD-7, SD-9, UZ-14, UZ-16, UZ-7a, UZ-N55, and WT-24. Again, a map showing the tunnel and borehole locations can be found in Figure 6.1-1. These measurements are compared with the chloride concentration outputs from the UZ chloride submodel. The simulations using the four infiltration maps are shown in Section 6.5, along with the simulated results (chloride concentrations) (Output DTN: LB0701UZMCLCAL.001). Because of the large spatial variations in chloride concentration, the comparison between the simulated and measured concentrations is done in log space. For simplicity, in this section, “the residual of chloride data” refers to the difference between the logarithm of the measured chloride concentration and the logarithm of the simulated chloride concentration.

For both data sets, because the numerical gridblock centers do not necessarily coincide with measurement points, linear interpolation is used to obtain the simulated temperatures at measurement locations.

6.8.4 UZ Flow Weighting Factors Definition/Description

The UZ flow scenarios correspond to selected present-day 10th, 30th, 50th, and 90th percentile infiltration scenarios generated by the infiltration model (DTN: SN0609T0502206.028 [DIRS 178753]). The UZ flow weighting factors (Output DTN: LB0701PAWFINFM.001, *factors.doc*) describe the probability of occurrence for each of the four infiltration scenarios, and therefore, the sum of the four weighting factors is one. The same weighting factors are expected to be used in all four climate states (present-day, monsoon, glacial transition, and post-10,000 years). The justification is given in Section 6.8.8.

2. Beven and Binley (1992 [DIRS 179079], Equation 5) provided a likelihood measure as follows:

$$L_i = \{\sum_{j=1}^{N_i} \frac{W_j}{(y_{ij} - O_j)^2}\}^N \quad \text{(Eq. 6.8-3)}$$

where W_j is the weight for observation j such that $\sum W_j = 1$. The same weight is used for all groups of observations. N is a parameter (called shape factor) chosen by the user. If *N=0*, all the infiltration maps will have the same weight, and if $N \to \infty$, the single best simulation will have a rescaled likelihood value of 1, and all others 0. In this study, likelihood values are calculated using *N=1* and *N=0.5*, based on the following considerations: (1) N = 1 has been frequently used in the literature as reviewed by Beven et al. (2000 [DIRS 179825], Table 1), and (2) the use of N = 0.5 allows for evaluating the sensitivity of the likelihood-function value to changes in N within a certain range. Note that if *N=0*, all the infiltration maps will have the same weight. Similarly if $N \to \infty$, the best simulation will single out a rescaled likelihood value of 1, and all others 0. (As shown below, a smaller N value will result in a larger weighting factor value for an infiltration map with a higher average infiltration rate, which is conservative.)

3. The third category of likelihood measures is (Beven and Binley 1992 [DIRS 179079], Eq. 6):

$$L_i = 1/(\prod_{j=1}^{K_t} (y_{ij} - O_j)^2) \quad \text{(Eq. 6.8-4)}$$

This is a pseudo-maximum likelihood function, which is similar to maximum likelihood because in its formulation more observation data (either data points or data types) will accentuate the better simulations, leading to greater reduction of uncertainty. This function can be an alternative when measurement errors are not available.

4. The fourth category uses fuzzy measures as likelihood measures. Although there are different ways of choosing fuzzy membership functions (Beven 2006 [DIRS 179081]), Equation 6.8-5 expresses the most commonly used triangular membership function as (Franks and Beven 1997 [DIRS 179084], Eq. 8):

$$f_{ij} = 1 - \frac{|y_{ij} - O_j|}{\varepsilon} \quad \text{(Eq. 6.8-5)}$$

where ε is called acceptable error. In this case, a maximum absolute residual (the term "residual" refers to the difference between the observed (O) and simulated values (y)) from all observation locations out of the four infiltration maps is taken as ε. Then, membership values at different observation points are combined using an arithmetic mean (Zak et al. 1997 [DIRS 179088]).

For the above measures, the final likelihood values are normalized as shown in Equation 6.8-6, so that the sum of the likelihood values for the four infiltration maps is one:

$$L_{i\_normalized} = L_i \Big/ \sum_{i=1}^{4} L_i \qquad \text{(Eq. 6.8-6)}$$

Two types of data reflecting infiltration history are available: thermal data (temperature) and chloride concentration. The likelihood functions based on each type are calculated separately, and combined by multiplying the normalized likelihood value together, as shown in Equation 6.8-7:

$$L_i = L_i^t \bullet L_i^c \qquad \text{(Eq. 6.8-7)}$$

where L_i^c is the likelihood value calculated using chloride data, and L_i^t is the likelihood value calculated using temperature data. This treatment for different types of data ensures that the two kinds of data can be considered one at a time without affecting the final results (as shown below).

Measured chloride data are available for both boreholes (vertical) and tunnels (horizontal). The map indicating the locations of these boreholes and tunnels can be found in Figure 6.1-1. Note that the amount of information (i.e., infiltration history) contained in a certain number of observations from a tunnel is greater than the same number of observations from a borehole, due to greater horizontal area covered in a tunnel. To consider the effect, chloride data is placed into three groups, with two groups representing the two horizontal tunnels and one group representing all the area covered by boreholes. The average absolute residual (or residual squares) from each borehole is used (in the borehole group) to represent the contribution from the given borehole. Then, the further average of squared average-residuals (or average of residual squares) for all the individual boreholes within the borehole group is used for the likelihood value calculation. This treatment is to ensure that the likelihood calculation is not biased to boreholes with more data points, considering that each borehole represents roughly the same amount of horizontal area intercepting infiltration and should be treated equally in evaluating the infiltration maps. For the other two groups, the average of squared average-residual (or average of residual squares) is directly used for likelihood-value calculations. For likelihood measure Category 1, the average of residual squares is used. For likelihood-measure Categories 2 and 3, both the average of absolute residuals and average of residual squares are used to evaluate effects of different averaging schemes. For likelihood-measure Category 4, the average of fuzzy membership is used. To be consistent with the treatment of chloride data, the averaged residuals (or average of residual squares) for the individual borehole data are also used for temperature likelihood calculations.

As shown in Equation 6.8-7, the calculation of likelihood functions based on each type is calculated separately, and then combined by multiplying the normalized likelihood value together. An alternative way to consider the two types of data is to consider one at a time, for example:

1. Update the weights using likelihood values calculated by chloride data (L_i^c), then the posterior weights P_i^1 (after considering chloride data) is (Makowski et al. 2002 [DIRS 179044]):

$$P_i^1 = \frac{W_i L_i^c}{\sum W_i L_i^c} \quad \text{(Eq. 6.8-8)}$$

Table 6.8-1. Calculated Weighting Factors Using Both Chloride Data and Temperature Data

Summary of Final Weights From All The Methods				
Infiltration map	**10%**	**30%**	**50%**	**90%**
S1	100%	0%	0%	0%
s2_a1_N=1	59%	21%	17%	3%
s2_a1_N=0.5	40%	24%	26%	11%
s2_a2_N=1	47%	24%	25%	4%
s2_a2_N=0.5	34%	24%	30%	12%
s3_a1	97%	3%	0%	0%
s3_a2	94%	6%	1%	0%
s4_sum	26%	24%	32%	18%
Average weighting factors	62%	16%	16%	6%

Output DTN: LB0701PAWFINFM.001, *factors.doc*.

Not only are the likelihood values, L_i^t and L_i^c, measures of matches between simulated results and observed data in the unsaturated zone, but also the prior weightings W_i (given in 6.8.5.1 Step 1) determine P_i. As shown in Table 6.8-1, the weighting factors are sensitive to the choice of likelihood measures, and the final weighting factors passed to TSPA for the four selected infiltration maps are determined as the arithmetic mean of the weightings P_i using the previously discussed methods (Equation 6.8-1).

Figure 6.8-2 shows the final likelihood of each infiltration map. Four bars represent the four infiltration maps. The weights for each map using an individual likelihood value correspond to the y-axis value for that individual likelihood function times its prior weights. The mean infiltration rate for the 10th, 30th, 50th and 90th percentile infiltration map can be found in Table 6.1-2. Note that the weighting factors are subject to uncertainty because of the uncertainties in defining likelihood functions. The downstream users of the weighting factors should consider both the mean values and the uncertainties of these factors (Table 6.8-1). Specifically, TSPA calculations need to consider both the mean values for the weighting factors and the results of individual likelihood functions.

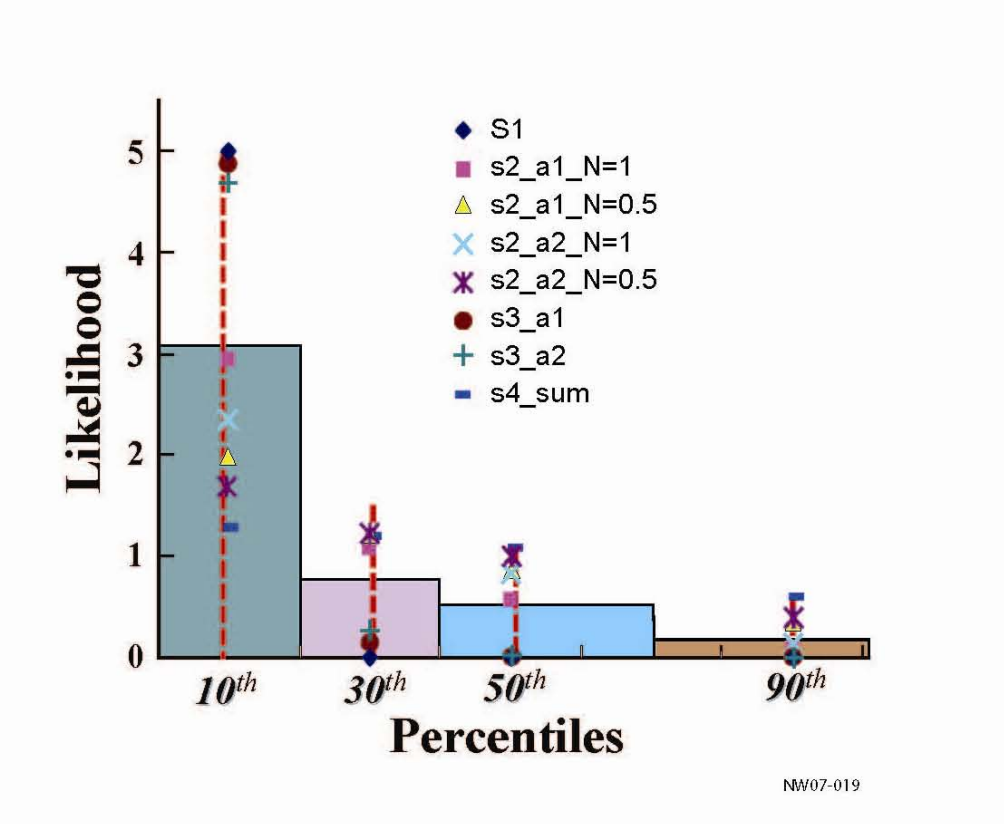

Output DTN: LB0701PAWFINFM.001.

NOTE: Shaded areas represent weighting factors and individual points represent likelihood values resulting from different calculation schemes.

Figure 6.8-2. Posterior Weighting Factors for Infiltration Map

6.8.6 Sensitivity Analysis for UZ Flow Weighting Factors

A number of sensitivity studies are performed to ensure that the results of likelihood value calculation are reasonable and robust.

6.8.6.1 Effects of Measurement Error for Temperature Data

The measurement errors (characterized by standard deviations) are used for evaluating the likelihood function given in Equation 6.8-2. For temperature measurement, the standard deviations representing measurement errors are on the order of 10^{-4}°C to ~ 10^{-3}°C (DTNs: GS031208312232.005 [DIRS 179284]; GS950208312232.003 [DIRS 105572]). A sensitivity analysis was performed for likelihood function 1 using a uniform standard deviation (0.1°C) for measurement errors to evaluate the effects of these deviations within a certain range for all the temperature observations. The resultant weighting factor values for the likelihood function are 1, 0, 0, and 0 for the 10th, 30th, 50th, and 90th percentile maps, respectively (Output DTN: LB0704UZWFINFM.001, file: *Cal_t1_sensitivity.xls*). That these are the same as those listed in Table 6.8-1 indicates that the variation of measurement errors within a reasonable range does not change the calculation results based on the first likelihood function.

7. VALIDATION

Validation activities for the UZ flow model and submodels were planned in *Technical Work Plan for: Unsaturated Zone Flow, Drift Seepage and Unsaturated Zone Transport Modeling, REV 04* (BSC 2006 [DIRS 177465], Section 2.2.1.1). The model validation approach for the UZ site-scale flow model is presented in *Technical Work Plan for Technical Work Plan for: Unsaturated Zone Flow, Drift Seepage and Unsaturated Zone Transport Modeling* (BSC 2006 [DIRS 177465], Section 2.2.1.1), which states that the UZ site-scale flow model requires Level I validation. The validation plan was developed under the BSC procedures in effect at the time. The BSC Level I validation is equivalent to Level I validation as described in SCI-PRO-002. The Level I validation includes the six steps of confidence building during model development as described in SCI-PRO-002 and at least one postdevelopment activities as described in SCI-PRO-006, Section 6.3.2. This model validation section deviates from the TWP (BSC 2006 [DIRS 177465], Section 2.2.1.1.2), in that temperature and chloride data are not used for validation. This is because the temperature and chloride data have been used to calibrate the flow weighting factors representing the effects of infiltration uncertainty discussed in Section 6.8. A second deviation includes the Alcove 8–Niche 3 flow and transport test data as one additional validation effort. The model validation efforts of this section include confidence building during model development and corroboration with experimental data. The additional validation activities presented in this section are corroboration with information published in refereed journals and literature, analysis of model uncertainties, and corroboration with natural analogues. The models will be accepted as valid for their purposes through confidence building during model development of Section 7.1, as well as through postdevelopment validation efforts of corroboration with experimental data in Sections 7.2 to 7.8, according to the following criteria (BSC 2006 [DIRS 177465], Section 2.2.1.1.2):

- The water-potential data measured from ECRB are used for validation by comparing with simulation results of the UZ flow model. The criterion for the validation is that simulated water-potential values are within the range of measurements along the ECRB tunnel. Demonstration that this criterion has been met is shown in Section 7.2.

- WT-24 perched water elevation data is used to validate the UZ flow model. The criterion for the validation is that simulated perched water elevation matches the observed value within 10 m). Demonstration that this criterion has been met is shown in Section 7.3.

- The gas-flow model was calibrated against the first 30 days of pneumatic data for borehole SD-12 (Section 6.4). Pneumatic data measured in SD-12 (for the second 30 days) and UZ-7a (for the second 30 days) are used for validation of the UZ flow model. The criterion for the validation is that simulated gas pressures and their patterns of variations consistently compare closely with the observed values. That is, the simulations will consistently reproduce increases and decreases resulting from changes in barometric pressure at the ground surface. Demonstration that this criterion has been met is shown in Section 7.4.

- Carbon-14 data from gas samples provide approximate C-14 residence times for pore water. The residence times can be interpreted as tracer transport time from the ground surface to where the gas samples were collected, based on the current conceptual model for UZ flow and transport. These data are used to validate the UZ flow model. The criterion for the validation is that simulated tracer transport times (i.e., the integral breakthrough curve at the sample-collection locations for a pulse input at the ground surface or the time for first moment of concentration) are within the range of times estimated from data in the TSw unit. Demonstration that this criterion has been met is shown in Section 7.5.

- Borehole and ECRB strontium concentrations are used to check the UZ flow model results using the strontium modeling analysis. The criterion for validation is qualitative agreement between the simulated strontium concentrations and the average of the observations at the same elevation, and agreement with the vertical trends. Demonstration that this criterion has been met is shown in Section 7.6.

- The calcite model is used to validate the UZ flow model with the abundance data of calcite. The calcite model is validated by comparing one-dimensional simulation results with measurements. The criterion is that the simulated volume fraction of calcite coating for each UZ model layer falls within the range of measurements for that layer. According to the TWP (BSC 2006 [DIRS 177465], Section 1, #1), the need of model validation runs are not expected for the calcite model results, because the uncertainty is already captured in the model runs. Demonstration that this criterion has been met is shown in Section 7.7. The current calcite model has not changed from the previous *UZ Flow Models and Submodels* (BSC 2004 [DIRS 169861], Section 7.9).

- A deviation from the work plan outlined in the TWP (BSC 2006 [DIRS 177465], Section 2.2.1.1) lies in the use of the Alcove 8–Niche 3 flow and transport test data. The original plan calls for the incorporation of the data to support the development of an enhancement factor to matrix diffusion in the unsaturated zone radionuclide transport model and the UZ transport abstraction model. This plan has not been implemented, and the resulting estimate of transport times through the unsaturated zone is conservative as explained in *Radionuclide Transport Models Under Ambient Conditions* (SNL 2007 [DIRS 177396], Section 6). Therefore, the information from the Alcove 8–Niche 3 fault test is used below to support the post-development validation of the site-scale UZ flow model. The same model validation criteria as described in the previous report (BSC 2004 [DIRS 169861], Section 7) are used for this model validation exercise (i.e., the criterion for validation is that the predicted results for the time to reach a given concentration of a conservative tracer are within a factor of 5 of the observed times, or that explanations can be found for why the observed and simulated results deviate significantly). Demonstration that this criterion was met is shown in Section 7.8. This validation exercise has not changed from the previous report (BSC 2004 [DIRS 169861], Section 7.6).

For the validation activities of this section, none of the corroborative data sets selected for use in model validation case used in model calibration and development of Section 6. In addition, there were no other similar data sets available for model validation activities. Note that model validation efforts, presented in this section, are carried out mostly by using the present-day, 10th and/or 30th percentile infiltration rates. This is because the present-day 10th and 30th percentiles are considered more realistic representations of the present-day conditions (Section 6.2).

Confidence Buidling with Information Published in Refereed Journals and Literature. In addition to the model validation activities described in the TWP, journal publications are used to provide confidence for model validation. Some methods listed here, including temperature and chloride modeling, are no longer conducted for validation (corroboration), but rather are part of the calibration or model development process. Three-dimensional unsaturated zone numerical models have been developed to simulate flow and distribution of moisture, gas, and heat at Yucca Mountain (Wu et al. 1999 [DIRS 117161]; Wu et al. 2004 [DIRS 173953]). Flow and transport processes within the unsaturated zone were characterized under current and future climates (Wu et al. 2002 [DIRS 160195]). Studies of capillary barriers in the unsaturated rock of Yucca Mountain have also been published (Wu et al. 2002 [DIRS 161058]). The perched water phenomena in the Yucca Mountain unsaturated zone have been investigated (Wu et al. 1999 [DIRS 117167]). Subsurface gas pressure variations have been used to determine the pneumatic diffusivity of important geological features (Ahlers et al. 1999 [DIRS 109715]; Wu et al. 2006 [DIRS 180289]). Subsurface borehole temperature data were used to estimate percolation flux (Bodvarsson et al. 2003 [DIRS 162477]). Chloride measurements were used to calculate infiltration rates along the ESF (Fabryka-Martin et al. 1998 [DIRS 146355]). Chloride data, in conjunction with hydrostructural and hydrogeological features, were also used to constrain infiltration rates (Liu et al. 2003 [DIRS 162478]). In addition, chloride and strontium geochemistry were investigated using three-dimensional modeling for insights into the hydrology of the unsaturated zone (Sonnenthal and Bodvarsson 1999 [DIRS 117127]). In particular, these published journal papers presented examples of using hydrologic, temperature, pneumatic and geochemical isotopic data to calibrate and validate the UZ flow model.

Analysis of Model Uncertainty. As discussed in Section 6.10, there are a number of uncertainties associated with the UZ flow model, including data, model, and climate uncertainties. The existence of these uncertainties stems from uncertainties in parameter and field data measurements, estimates of present-day and future climates, hydrogeological conceptual models and modeling approaches, and scale-dependent heterogeneity, and model input parameters. These data- and model- related uncertainties have been discussed, investigated or evaluated in this report using field observation data, modeling sensitivity analyses, model calibration, natural analogue information, and other arguments in Sections 6.2 through 6.9 and this section. These uncertainties are reasonably captured by simulation results using four different parameter sets and 16 infiltration maps, as discussed in Section 6.10. The effects of parameter and data uncertainties on UZ flow model results are generally encompassed by the model results for the 16 three-dimensional flow fields. Systematic sensitivity analyses of the UZ flow model results (to model input parameters) were carried out to assess uncertainties associated with parameters and models (BSC 2005 [DIRS 174116]; Zhang et al. 2006 [DIRS 180287]). In addition, the uncertainty of flow and radionuclide transport in the Yucca Mountain unsaturated zone was investigated using a Monte Carlo method with matrix

permeability, porosity, and sorption coefficient treated as random variables (Ye et al. 2006 [DIRS 180272]).

Corroboration with Natural Analogues. In addition, the key flow and transport processes pertaining to the unsaturated zone at Yucca Mountain have been investigated through natural analogues (BSC 2004 [DIRS 169218]). These natural analogue investigations contained both literature studies and analyses. One of the important case studies was the unsaturated zone flow and tracer tests at the Idaho National Engineering and Environmental Laboratory's Radioactive Waste Management Complex (BSC 2004 [DIRS 169218], Section 9.3). The field tests at the site provided calibrations of numerical models with needed in situ measured data. A consistent set of parameters was obtained from calibrating the model using the dual-permeability approach to multiple hydrographs (water potential as a function of time) from transient ponded infiltration tests. The studies demonstrated that conceptual models and large-scale, volume-averaged numerical modeling approaches used for the UZ flow model at Yucca Mountain can be applied with confidence (BSC 2004 [DIRS 169218], Section 9.3.7). The model validation effort of this section is intended to further build confidence in the UZ flow model and submodels with regard to their ability to predict flow and transport processes in the Yucca Mountain unsaturated zone system. In particular, these model validation efforts further confirm that using uniform hydrogeologic parameter values across the lateral extent of most hydrostratigraphic units in the UZ flow model provides reasonable approximations and simulation results, because of the model's capability for matching different types of data from boreholes that are a considerable distance apart.

7.1 CONFIDENCE BUILDING DURING MODEL DEVELOPMENT

To establish the scientific basis and the accuracy of intended use, SCI-PRO-006 and SCI-PRO-002 require documentation of decisions or activities that are implemented to generate confidence in the model during model development, including the following:

(1) Evaluate and select input parameters and/or data that are adequate for the model's intended use [SCI-PRO-002, Attachment 3, Level I (1)].

The selection of input parameters and/or input data for the UZ flow model and its submodels is discussed and presented in Sections 4.1, 6.1–6.5, and Appendix B. Model calibration results in Section 6 show that these selected input parameter values or input data are reasonable for simulating flow and transport processes in the Yucca Mountain unsaturated zone.

(2) Formulate defensible assumptions and simplifications that are adequate for the model's intended use [SCI-PRO-002, Attachment 3, Level I (2)].

As discussed in Sections 5 and 6.1.2, the development of the UZ flow model and its submodels is based on assumptions and simplifications that are accepted in the scientific community, which are supported by many scientific journal publications, as discussed above.

(3) Ensure consistency with physical principles, such as conservation of mass, energy, and momentum, to an appropriate degree commensurate with the model's intended use [SCI-PRO-002 Attachment 3, Level I (3)].

host rock are listed in Table 6.4-1. The criterion for the validation is that simulated gas pressures and their pattern variations are consistent with the observed values. That is, the simulations will consistently reproduce increases and decreases resulting from changes in barometric pressure at the ground surface.

7.4.1 Validation of the UZ Model for the Scenario of the 10th-Percentile Infiltration Map

Simulated results are compared with field-measured values of the 30-day validation period for the 10th percentile infiltration scenario (Figures 7.4-1 and 7.4-2) and the 30th percentile infiltration scenario (Figures 7.4-3 and 7.4-4), respectively. Overall, good agreement between the predicted gas pressures and observed data were found in both scenarios. The good match builds confidence that the calibrated properties are appropriate for gas flow simulations in either case. Comparisons between simulated and observed gas pressures at different locations of the two boreholes, shown in the two figures, prove that simulated gas pressures and their patterns of variations are consistent with observed values. In particular, the simulations consistently reproduce increases and decreases resulting from changes in barometric pressure at the ground surface. This satisfies the validation criterion for this case.

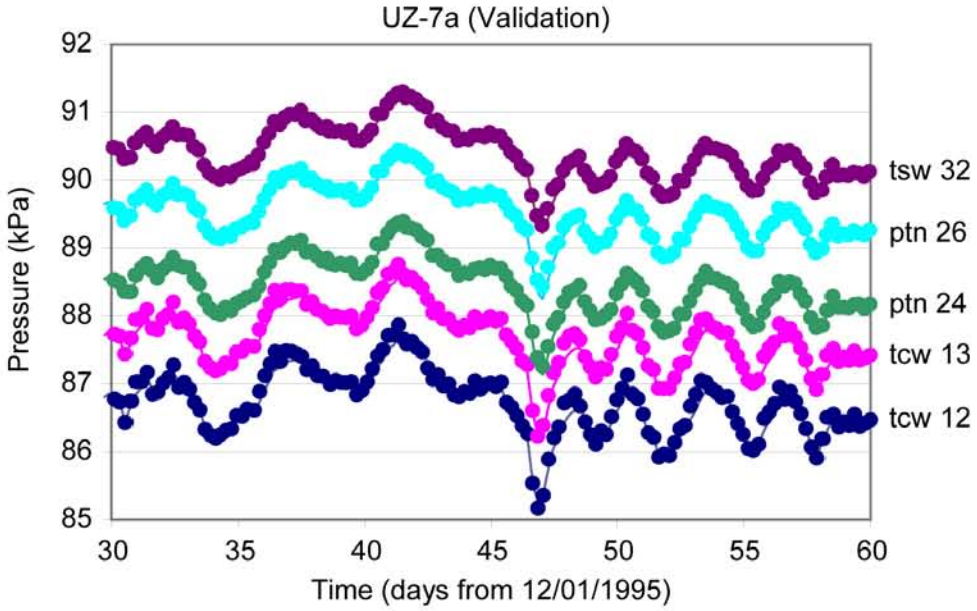

Source: DTN: LB0612MTSCHPFT.001 [DIRS 180296].

Output DTN: LB07043DGASCAL.001.

NOTE: The hydrogeologic units shown on the figure (e.g., tcw12) are determined from a comparison of the borehole location and measurement depth with the spatial data for the hydrogeolgic units available from the UZ model grid. Both observations and simulations have been vertically offset for clear display.

Figure 7.4-1. Comparison of Predicted (solid line) and Observed (solid dots) Gas Pressures at Borehole UZ-7a During the Second 30-day Period for the 10th Percentile Infiltration Scenario

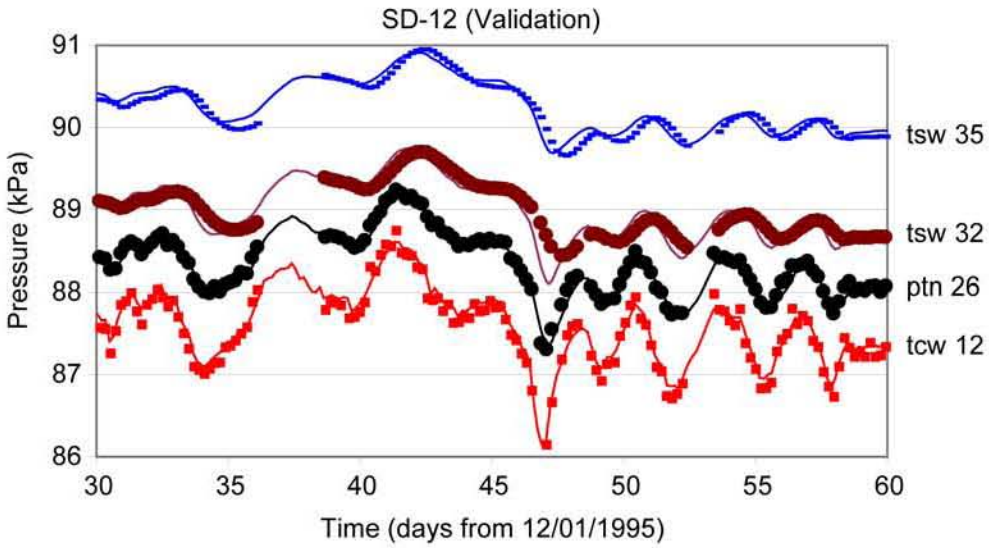

Source: DTN: LB0612MTSCHPFT.001 [DIRS 180296].

Output DTN: LB07043DGASCAL.001.

NOTE: The hydrogeologic units shown on the figure (e.g., tcw12) are determined from a comparison of the borehole location and measurement depth with the spatial data for the hydrogeolgic units available from the UZ model grid. Both observations and simulations have been vertically offset for clear display.

Figure 7.4-2. Comparison of Predicted (solid line) and Observed (solid dots) Gas Pressures at Borehole SD-12 During the Second 30-day Period for the 10th Percentile Infiltration Scenario

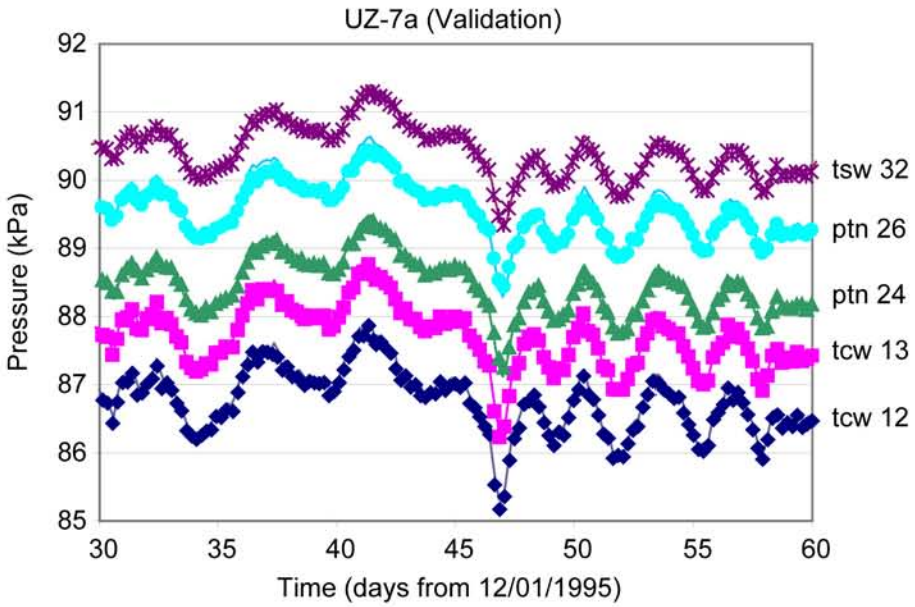

Source: DTN: LB0612MTSCHPFT.001 [DIRS 180296].

Output DTN: LB07043DGASCAL.001.

NOTE: The hydrogeologic units shown on the figure (e.g., tcw12) are determined from a comparison of the borehole location and measurement depth with the spatial data for the hydrogeolgic units available from the UZ model grid. Both observations and simulations have been vertically offset for clear display.

Figure 7.4-3. Comparison of Predicted (solid line) and Observed (solid dots or symbols) Gas Pressures at Borehole UZ-7a During the Second 30-day Period for the 30th Percentile Infiltration Scenario

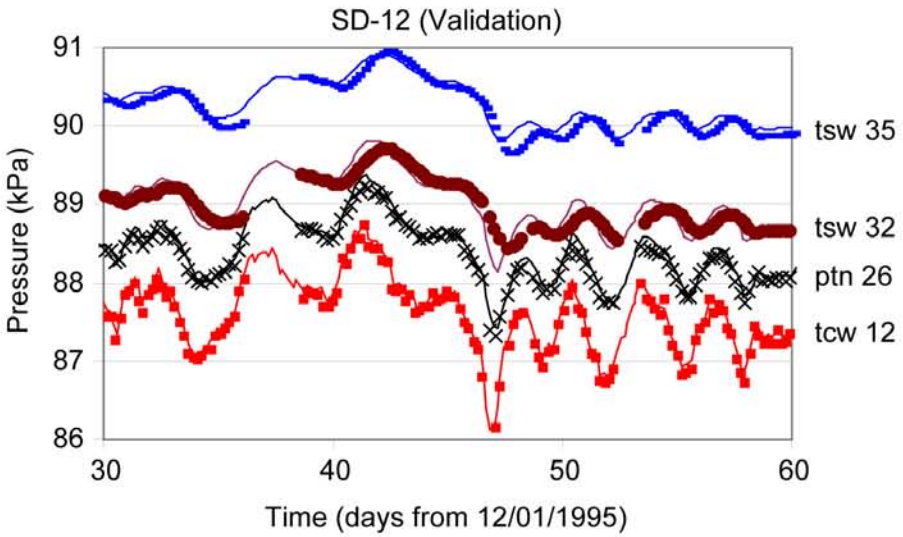

Source: DTN: LB0612MTSCHPFT.001 [DIRS 180296].

Output DTN: LB07043DGASCAL.001.

NOTE: The hydrogeologic units shown on the figure (e.g., tcw12) are determined from a comparison of the borehole location and measurement depth with the spatial data for the hydrogeolgic units available from the UZ model grid. Both observations and simulations have been vertically offset for clear display.

Figure 7.4-4. Comparison of Predicted (solid line) and Observed (solid dots or symbols) Gas Pressures at Borehole SD-12 During the Second 30-day Period for the 30th Percentile Infiltration Scenario

7.5 MODEL VALIDATION WITH ^{14}C DATA

This section describes the simulation of the solute travel times using the calibrated UZ flow models, and the comparison of the simulated travel times to the measured ^{14}C ages for borehole UZ-1 and SD-12, for validation of the UZ flow models. The criterion for the validation is that the simulated travel times for TSw units fall within the range of the measured ^{14}C ages for the TSw units.

7.5.1 Methodology

In a flow system, at a given location and time, the solute residence time (travel time) is determined within the whole system by the applicable transport processes, such as advection, diffusion and hydrodynamic dispersion. The actual residence time can be determined using a number of methods, including measuring a radioactive isotope activity and then calculating the residence time based on the decay rate. Residence time can also be simulated using a flow and conservative tracer transport model of the system (Goode 1996 [DIRS 162573]). The degree to which the model-simulated residence times fall within the range of the measured residence times can be used for validating the flow and transport model. The Yucca Mountain unsaturated zone is considered to be a quasi-steady-state flow system (Section 5). An appropriate solute residence time to use is the mean transport time required for the solute to move from the ground surface to the sample location in the subsurface system. The mean solute residence time can be considered to be constant at each location in this quasi-steady-state flow system, but spatially variable. When a tracer pulse is injected into the system through the ground surface, the tracer

to its half-life duration, which is on the same order of magnitude as the travel times in the unsaturated zone, and its detectable abundance. Gas samples were collected from different kinds of boreholes, including open and instrumented surface-based boreholes. Data from the latter boreholes (USW SD-12 and USW UZ-1) are regarded as more reliable indicators of solute travel time for the in situ matrix pore water (BSC 2004 [DIRS 169734], Section 5.2.2.5.4). Thus, the measured ^{14}C ages (BSC 2004 [DIRS 169734], Section 5.2.2.5.4) data from these two boreholes are used for validating the UZ flow model.

Gas-phase ^{14}C ages (Output DTN: LB0704C14FFVAL.001 for the conversion of ^{14}C activity into ages, and DTNs: GS961108312271.002 [DIRS 121708] for the ^{14}C activity of borehole USW SD-12, and MO0012CARB1314.000 [DIRS 153398] for the ^{14}C activity of borehole USW UZ-1) are interpreted to be representative of solute travel times for the *in-situ* matrix pore water. The rationale for this interpretation is provided by Yang (2002 [DIRS 160839], Section 4.1.2). The interpretation is based on the rapid exchange of gas-phase CO_2 (reaching equilibrium in hours to days) with dissolved CO_2 and HCO_3^- in pore water. Furthermore, the amount of carbon in an aqueous-phase reservoir is greater by orders of magnitude than carbon in the CO_2 gas-phase reservoir. Consequently, the aqueous phase will dominate the gaseous phase when exchange occurs, indicating the reasonableness of the interpretation (Yang 2002 [DIRS 160839], Section 4.1.2). The continuous calcite precipitation in the unsaturated zone removes carbon from groundwater. Although ^{14}C behaves a little differently from total carbon, the effect on the carbon isotopic fraction is minor, and the calcite precipitation is considered to have an insignificant impact on the ^{14}C activity in the groundwater and gas (Codell and Murphy 1992 [DIRS 100719]). Therefore, the measured gas-phase ^{14}C age is considered as representative data for the solute travel times of the matrix pore water of the Yucca Mountain unsaturated zone in the following model validation effort. Obviously, one necessary condition of this interpretation must be satisfied (i.e., there is no significant vertical gas flow through the borehole). This interpretation becomes limited if there is significant vertical gas flow through the borehole, because such flow would disturb the ^{14}C abundance distribution throughout the borehole. In fact, because the boreholes (USW SD-12 and USW UZ-1) were closed, disturbation from the atmosphere can be neglected (unless leakage of atmospheric CO_2 into the borehole occurs), vertical gas flow in these two boreholes is not likely significant, and the ^{14}C abundance is not significantly disturbed.

7.5.3 Model Discussion

Two three-dimensional transport simulations were performed using T2R3D V1.4 (LBNL 1999 [DIRS 146654]). The three-dimensional flow fields of two infiltration scenarios, 10th percentile and 30th percentile, from UZ flow models (Output DTN: LB06123DPDUZFF.001) were respectively used to simulate the solute travel times in the entire model domain. The numerical grid used in this transport simulation is the same as that used in the flow simulation (Figure 6.1-1). As discussed in Section 6.7, hydrodynamic dispersion was ignored because of low water percolation fluxes. Thus, the ^{14}C transport is carried out primarily by advective and diffusive processes. An effective-diffusion-coefficient value of 1.97×10^{-10} m^2/s was used, equal to the average value of measured coefficients for tritiated water through Yucca Mountain tuffs (DTN: LA000000000034.002 [DIRS 148603]).

In this model, a tracer source was introduced as a pulse on the ground surface through fractures, and the tracer concentration in rock matrix was observed in the entire domain over the whole simulation period (10^6 years). The simulated solute travel time of the matrix pore water, at a specific location, was then calculated using Equation 7.5-1 for each representative gridblock of borehole UZ-1 and SD-12. Then, the simulated solute travel times were compared to the measured ^{14}C ages. The simulated solute travel times of the matrix pore water for boreholes UZ-1 and SD-12 were plotted and compared, respectively, to the available measured ^{14}C age data in Figures 7.5-1 for UZ-1 and 7.5-2 for SD-12.

Figure 7.5-1 shows that the simulated solute travel times for the matrix porewater of borehole UZ-1 with the three-dimensional UZ model and the 10th percentile infiltration map are much larger than the measured ^{14}C ages, while the simulated ages with the 30th percentile infiltration map are closer to the measurements and fall within the range of measurements for TSw units. There are larger uncertainties in the measured data of the shallow layers (i.e. PTn units), resulting from the disturbance caused by possible leakage of the atmospheric CO_2 into the borehole. Figure 7.5-2 shows that the simulated solute travel times for the matrix pore water of borehole SD-12 with the three-dimensional UZ model and the 30th percentile infiltration map falls within the range of the measured ^{14}C ages for TSw units, while the simulated solute travel times with the 10th percentile infiltration map are larger than the measurements. These results reflect the spatial uncertainties of the infiltration maps as discussed in *Simulation of Net Infiltration for Present-Day and Potential Future Climates* (SNL 2007 [DIRS 174294], Section 6.6.1.1) and are consistent with the study results that more weight should be given to the infiltration maps with percentiles lower than 50th (Section 6.8).

Table 7.5-1. Infiltration Rates of the Representative Gridblock of Borehole UZ-1 and SD-12

	Local infiltration rates(mm/yr)		Domain-average infiltration rates (mm/yr)	
Boreholes	10%	30%	10%	30%
UZ-1	0.0	0.38	3.03	7.96
SD-12	0.8	2.17	3.03	7.96

Source: Output DTN: LB06123DPDUZFF.001, *PD_10.dat* and *PD_30.dat* (domain average infiltration rates in mm/yr and location infiltration rates in kg/s), also see Table 6.1-2.

Output DTN: LB0704C14FFVAL.001 (*infiltration.xls*, converted local infiltration rates in mm/yr).

* "Local infiltration" is the infiltration at the representative gridblock in the infiltration map. The "Domain-average infiltration" is the average infiltration rate of the whole model domain of the corresponding percentile.

As mentioned in Table 7.5-1, the infiltration map shows that the local infiltration rate of the representative gridblock for borehole UZ-1 is 0.0 mm/yr (10th percentile), compared to the domain average of 3.03 mm/yr. The fact that the calculated solute travel times of this borehole with the 10th percentile infiltration map are much larger than the measured ^{14}C ages (Figure 7.5-1) may primarily be a result of the too-low local infiltration rate (compared to the actual infiltration rate). The second possible reason of this deviation is the horizontal heterogeneity in the rock hydraulic properties (permeability and porosity), which is not considered in the model. The other possible reason is the scale-dependency of the effective matrix diffusion coefficient (BSC 2004 [DIRS 170035], Section 6.2.2), which is not considered

in the model. A larger effective matrix diffusion coefficient is expected to give a smaller travel time in the rock matrix.

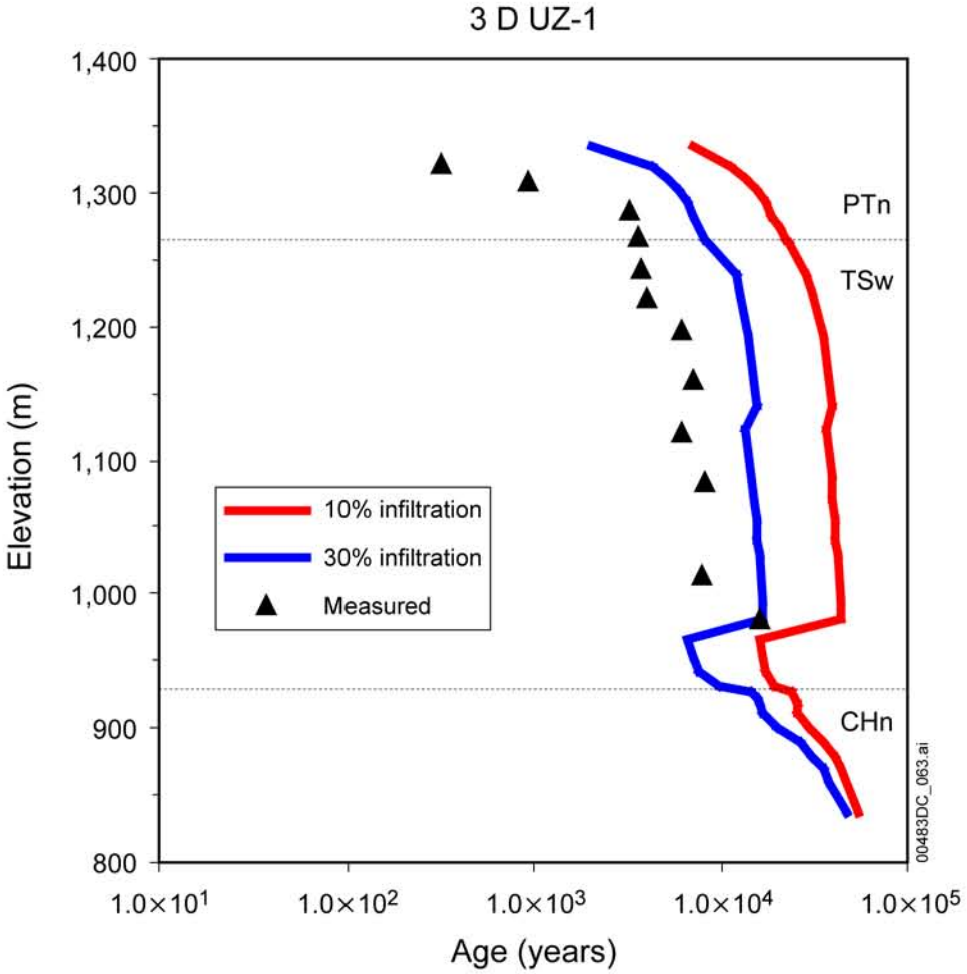

Sources: DTNs: MO0012CARB1314.000 [DIRS 153398] (Measured ^{14}C activities); MO0012MWDGFM02.002 [DIRS 153777] (borehole collar elevation and lithological layer interface elevation); LB06123DPDUZFF.001 (flow fields of 10% and 30% infiltration rate).

Output DTN: LB0704C14FFVAL.001, LB0707C14FFVAL.001, *Ages.xls* (simulated matrix porewater age, and measured ^{14}C ages converted from the measured ^{14}C activities).

Figure 7.5-1. Simulated Solute Travel Time of the Matrix Pore Water with Three-dimensional Simulation for Borehole UZ-1 Compared to the Measured ^{14}C Age

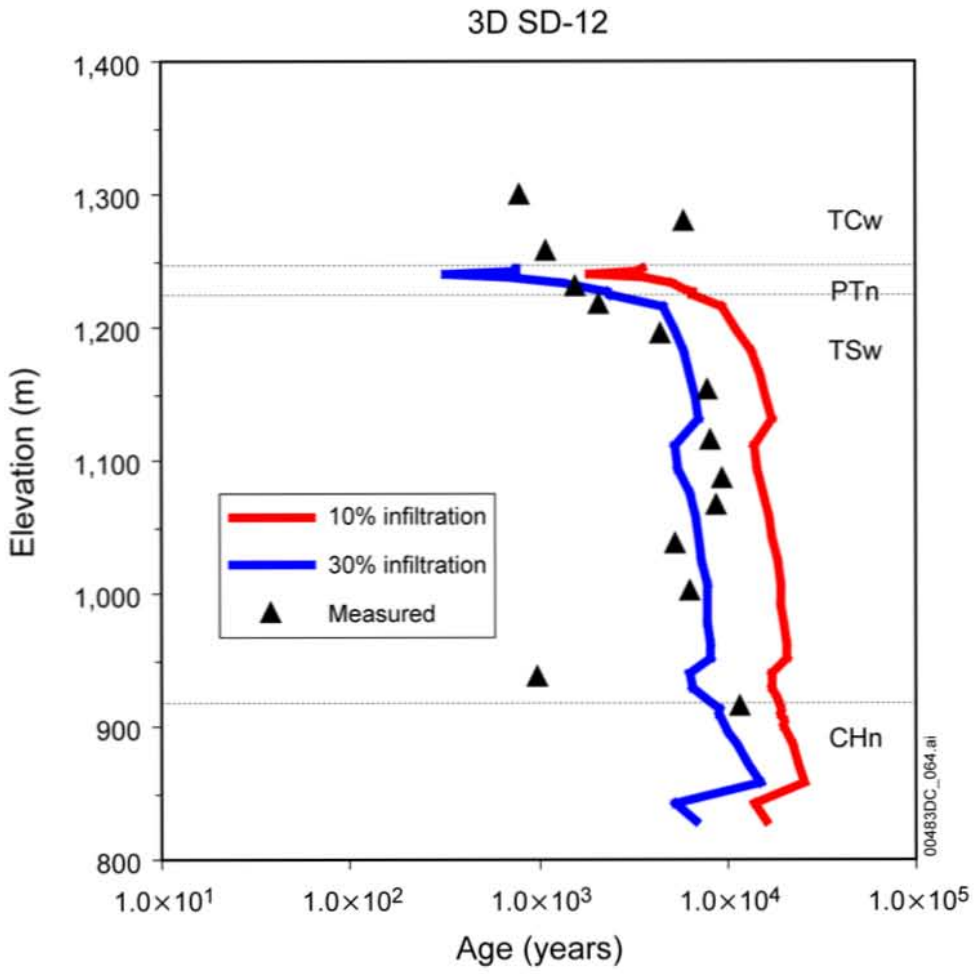

Sources: DTNs: GS961108312271.002 [DIRS 121708] (measured ^{14}C activities); MO0012MWDGFM02.002 [DIRS 153777] (borehole collar elevation and lithological layer interface elevation); Output DTN: LB06123DPDUZFF.001 (flow fields of 10% and 30% infiltration rate).

Output DTNs: LB0704C14FFVAL.001, LB0707C14FFVAL.001, *Ages.xls* (simulated matrix porewater age, and measured ^{14}C ages converted from the measured ^{14}C activities).

NOTE: Only one sample is plotted for each depth if there are multiple samples for one location.

Figure 7.5-2. Simulated Solute Travel Time of the Matrix Pore Water with Three-dimensional Simulation for Borehole SD-12 Compared to the Measured ^{14}C Age

To investigate how uncertainty in the infiltration maps affects the simulated solute travel times, a one-dimensional model was constructed for these two boreholes using the domain-average infiltration rate (10th and 30th percentile, respectively, Table 7.5-1) as an order of magnitude analysis. In comparison, the one-dimensional model reduces the uncertainties associated with spatial variation of surface infiltration rates and lateral flow with a three-dimensional model. Therefore, the one-dimensional model results are considered to be appropriate to examine the sensitivity of model simulated mean travel time to infiltration rates. The domain-average infiltration rates are higher than the respective local infiltration rate given in the 10th and 30th percentile infiltration map. The same tracer simulations described above were repeated using one-dimensional columns extracted from the three-dimensional model at locations representing SD-12 and UZ-1, and the domain-average infiltration rate (Table 7.5-1). A grid mesh of the one-dimensional simulations was made from the extracted representative gridblocks and the

connections of borehole UZ-1 and SD-12, from the three-dimensional grid mesh. Steady-state flow fields for UZ-1 and SD-12 with the domain-average infiltration rate of the 10th and 30th percentile were respectively performed using the EOS9 module of TOUGH2 V1.6 (2003 [DIRS 161491]). These steady-state flow fields (*flow9.dat* files) were then used to simulate the tracer transport processes through the representative one-dimensional columns of UZ-1 and SD-12, using T2R3D V1.4 (1999 [DIRS 146654]). The same methodology was used for tracer transport simulations and the conversion of the solute travel times of the matrix pore water from the simulated tracer concentration breakthrough, as described earlier for the three-dimensional simulations in this section. The simulated solute travel times of the pore water are plotted and compared to the measured ^{14}C age on Figure 7.5-3 (UZ-1) and Figure 7.5-4 (SD-12).

Figure 7.5-3 shows that the simulated solute travel times of borehole UZ-1 with the 30th percentile domain-average infiltration match better than that from the three-dimensional simulation (with the very low local infiltration rates), and the simulated solute travel times with the 10th percentile infiltration are also close to the measurements, but not as good as that for the 30th percentile infiltration. This finding implies that an infiltration rate between the 10th and 30th percentile domain-average infiltration will make a better fit to the measured ^{14}C ages for this borehole. Figure 7.5-4 shows that the simulated solute travel times of borehole SD-12 with the 30th percentile domain-average infiltration match the measurements well, and the results with the 10th percentile domain-average infiltration fall out of range of the measurements for TSw units. These results indicate that the simulated solute travel time is sensitive to the infiltration rate, and subject to the spatial uncertainties in the infiltration maps.

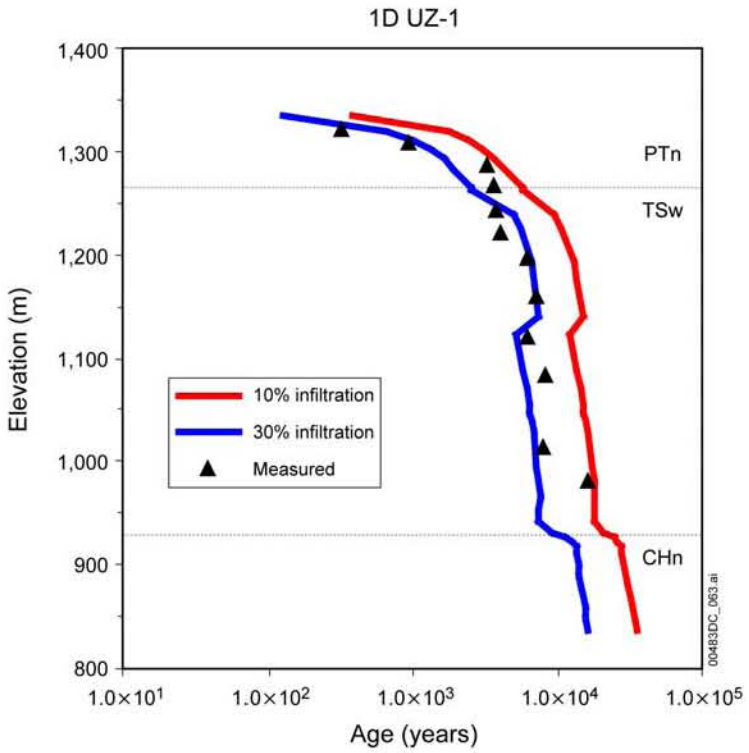

Sources: DTNs: MO0012CARB1314.000 [DIRS 153398] (Measured ^{14}C activity); MO0012MWDGFM02.002 [DIRS 153777] (borehole collar elevation and lithological layer interface elevation); Output DTN LB06123DPDUZFF.001 (flow fields of 10% and 30% infiltration rate).

Output DTN: LB0704C14FFVAL.001, LB0707C14FFVAL.001, *Ages.xls* (simulated matrix porewater age, and measured ^{14}C ages converted from the measured ^{14}C activities).

Figure 7.5-3. Simulated Solute Travel Time of the Matrix Pore Water with One-dimensional Simulation for Borehole UZ-1 Compared to the Measured ^{14}C Age

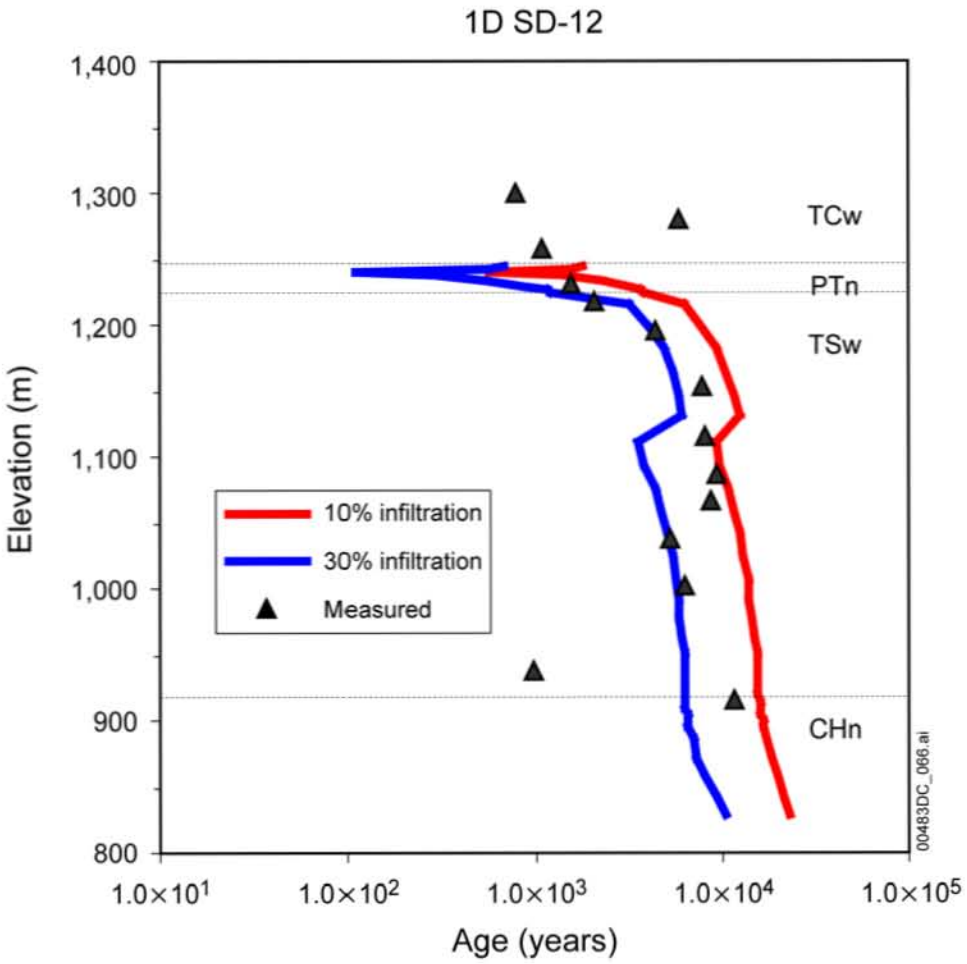

Sources: DTNs: GS961108312271.002 [DIRS 121708] (measured ^{14}C activities); MO0012MWDGFM02.002 [DIRS 153777] (borehole collar elevation and lithological layer interface elevation); Output DTN LB06123DPDUZFF.001 (flow fields of 10% and 30% infiltration rate).

Output DTN: LB0704C14FFVAL.001, LB0707C14FFVAL.001, *Ages.xls* (simulated matrix porewater age, and measured ^{14}C ages converted from the measured ^{14}C activities).

NOTE: Only one sample is plotted for each depth if there are multiple samples for one location.

Figure 7.5-4. Simulated Solute Travel Time of the Matrix Pore Water with One-dimensional Simulation for Borehole SD-12 Compared to the Measured ^{14}C Age

7.5.4 Summary

The solute travel times were simulated using a transport model based on the calibrated groundwater flow fields for the unsaturated zone, and using the 10th and the 30th percentile infiltration maps. The measured gas-phase ^{14}C ages from two instrumented boreholes (UZ-1 and SD-12) have been justified to be representative of the solute travel time for the matrix pore water. Data uncertainties were also discussed. Good matches between the calculated solute travel times and the measured ^{14}C ages was attained for borehole SD-12 with the three-dimensional UZ model and using the 30th percentile infiltration map, and an acceptable match was obtained for borehole UZ-1 using the 30th percentile infiltration map. These results reflect the spatial uncertainties in the infiltration maps as discussed in *Simulation of Net Infiltration for Present-Day and Potential Future Climates* (SNL 2007 [DIRS 174294], Section 6.6.1.1) and are

3. sr_high3_pd_30: High $C_{Sr,eff}$ (14.8 µg/liter) for present-day (pd) 30th percentile infiltration and precipitation rates. $K_{d,Sr}$ = 1.0 m^3/kg.

4. sr_high3_pd_30: High $C_{Sr,eff}$ (14.8 µg/liter) for present-day (pd) 30th percentile infiltration and precipitation rates. $K_{d,Sr}$ = 2.0 m^3/kg.

5. sr_mid2_pd_10: Lower $C_{Sr,eff}$ (5.8 µg/liter) for present-day (pd) 10th percentile infiltration and precipitation rates. $K_{d,Sr}$ = 1.0 m^3/kg.

6. sr_mid2_pd_30: Lower $C_{Sr,eff}$ (5.8 µg/liter) for present-day (pd) 30th percentile infiltration and precipitation rates. $K_{d,Sr}$ = 1.0 m^3/kg.

Inputs and outputs for the three-dimensional model simulations have been submitted to the TDMS under DTN: LB0705UZSRTRAN.001.

Modeled strontium concentrations are compared to measured values for pore salts extracted (by leaching) from two surface-based boreholes (SD-9 and SD-12; DTN: GS990308315215.004 [DIRS 145711]), perched waters, and pore waters obtained by ultracentrifugation of core samples from the ECRB and for SD-9 (DTN: GS020408312272.003 [DIRS 160899]). Comparison of concentrations determined by ultracentrifuge and by water leaches on the same samples have shown that the ultracentrifuge concentrations are higher and probably closer to the true pore water concentrations (see Figure 7.6-1a for SD-9 samples).

Comparisons of measured and modeled strontium concentrations as a function of elevation for the surface-based boreholes (SD-9 and SD-12) are shown in Figure 7.6-1(a and b). Measured concentrations in the unsaturated zone above the perched water show a range of concentrations from about 0.1 to 3 mg/L in nonzeolitic and down to about 0.005 mg/L in zeolitic. Moderately large variations exist in the measured strontium concentrations as a function of depth in the unsaturated zone above the zeolitic horizons. The high concentration, 30th percentile precipitation/infiltration and the lower (mid2) 10th percentile simulation results are closest to the measured data in boreholes SD-9 and SD-12. Looking more closely at the profiles, the near-surface data is closer to the 10th percentile precipitation/infiltration, and the deeper data (above the perched water) is closer the 30th percentile simulations at the lower effective concentration. This may be a result of climate changes where deeper waters reflect a higher proportion of older potential Pleistocene-age water (Sonnenthal and Bodvarsson 1999 [DIRS 117127]).

The sharp reduction in strontium concentrations in the perched water bodies, and in the zeolitic units below, is consistent with ion exchange in zeolitic rocks, since the decrease is much greater than the equivalent drop in chloride concentrations. Where perched water samples were collected in SD-9, the model results show a strong decrease, but not as small a value as those measured in zeolitic rocks. An increase in $K_{d,Sr}$ of a factor of 2 does not make a significant difference in the results. Owing to the initialization of the pore water in the zeolitic rocks to the saturated zone value, which is higher than those measured in the perched water in SD-9, the concentrations never drop below this value, and therefore do not match the perched water or zeolitic pore waters in SD-12. Changing the initialization to a much lower value would result in a much better match,

but could not be independently supported by any measured data. In SD-12, the measured and modeled

7.7 CALCITE MODEL

7.7.1 Introduction

According to the TWP (BSC 2006 [DIRS 177465], Section 1), the model validation runs do not need updating from the previous work, because the infiltration rates used in calcite modeling still bound the new base-case infiltration rates. As shown in Table 6.1-2, the average rate over the model domain for the present-day 10th percentile infiltration with the UZ model grid is 3.03 mm/yr (the base-case infiltration scenario). For the WT-24 location that was used for calcite analysis, the new base-case infiltration rate is 9.25 mm/yr. These infiltration rates in the current flow model fall into the range from 2 to 20 mm/yr used in the previous calcite modeling. Therefore, Section 7.7 is basically a reproduction of Section 7.9 of the previous report (BSC 2004 [DIRS 169861]). The current content has some revisions: (1) inclusion of a commentary by Dublyansky and Smirnov (2005 [DIRS 180650]) on the journal publication of this calcite model by Xu et al. (2003 [DIRS 162124]), and the reply to the commentary paper by Sonnenthal et al. (2005 [DIRS 180639]) (see the end of this section, and Section 7.7.5.1), and (2) some clarifications for technical reviews. The conclusions of the current report have not changed from the previous report (BSC 2004 [DIRS 169861]).

The percolation flux in the unsaturated zone is an important parameter because it controls seepage into drifts that may contact waste packages. As shown in Section 6.6, it depends strongly on the infiltration flux, which is a boundary condition of the UZ flow model. Observations of precipitated calcite in the unsaturated zone constrain the infiltration flux. Therefore, comparing observed hydrogenic calcite deposits to simulations increased confidence in the model's ability to capture this boundary condition. Because direct measurements of infiltration flux are not possible, this confirmation of the boundary condition generally builds confidence in the UZ flow model. Hydrogenic calcite deposits in fractures and lithophysal cavities at Yucca Mountain have been studied to estimate past percolation fluxes (Carlos et al. 1995 [DIRS 162118]; Marshall et al. 1998 [DIRS 107415]; BSC 2004 [DIRS 169734], Section 7.7.1).

One objective of these previous studies was to investigate the relationship between percolation flux and measured calcite abundances. The U.S. Geological Survey (USGS) determined calcite abundances from a deep surface-based borehole (WT-24) (DTN: GS021008315215.007 [DIRS 162127]). Geochronology work performed by the USGS (Neymark et al. 2001 [DIRS 156889]) indicates that this calcite formed over approximately 10 million years. Hydrogenic mineral coatings in the unsaturated zone are nonuniformly distributed and located almost entirely on fracture footwalls and cavity floors—in contrast to saturated environments, in which vein and cavity deposits usually coat all surfaces.

A one-dimensional model column corresponding to the location of a deep borehole (WT-24) was chosen for modeling calcite deposition because measured calcite abundances (DTN: GS021008315215.007 [DIRS 162127]) were available for comparison. Here, the results of a reactive transport numerical model for calcite deposition under different infiltration conditions are presented. The setup and results of the problem are cited from the report by Xu et al. (2003 [DIRS 162124]). The reactive transport model used here considers the following essential factors affecting calcite precipitation: (1) infiltration, (2) the ambient geothermal

gradient, (3) gaseous CO_2 diffusive transport and partitioning in liquid and gas phases, (4) fracture–matrix interaction for water flow and chemical constituents (dual permeability), and (5) water–rock interaction. Any water–rock interaction effects (e.g., pH modification) also affect the calcite solubility, hence, its abundance in each rock unit. The dual permeability model allows us to address not only the abundances of calcite with depth, but also its relative abundance in fractures and in the rock matrix as a function of the hydrological/geochemical processes in each medium, as well as the interaction of water flowing between fractures and matrix.

Dublyansky and Smirnov (2005 [DIRS 180650]) wrote a comment paper on the journal article by Xu et al. (2003 [DIRS 162124]), which questioned inappropriate thermal boundary conditions for simulations used. The comment paper contended that the calcite was formed by upwelling hydrothermal waters and that the original journal article considered a constant ambient geothermal gradient for the approximately 10 million-year period, rather than a higher gradient which has been inferred from fluid inclusions. In reply to the commentary paper, Sonnenthal et al. (2005 [DIRS 162127]) performed a simulation with variable bottom boundary temperatures approximating those measured in fluid inclusions. The results of this simulation is discussed later in Section 7.7.5.1.

It should be pointed out that the one-dimensional calcite data modeling and analysis do not have to do with the direct validation of the three-dimensional flow model, but this model may provide some additional evidence for the validation at a location. A steady-state one-dimensional flow field was used for the analysis, because here the primary interest is long-term calcite deposition within the TSw unit, in which flow is primarily one-dimensional vertical gravity-driven.

7.7.2 Calcite Precipitation Mechanisms

Along with wind-blown dust, precipitation carries much of the calcium to the surface (Vaniman et al. 2001 [DIRS 157427]). In the soil zone, strong evapotranspiration, along with some water–rock interaction and root-zone biological processes, leads to saturation with respect to calcite. The depth to reach calcite equilibrium depends on climate and infiltration variations over time, episodic water flow, and near-surface biogeochemical conditions. During more typical smaller infiltration events, calcite may reach equilibrium close to the surface. However, large infiltration pulses of calcite-undersaturated water can dissolve near-surface calcite and reach equilibrium at a greater depth. This model validation activity concerns calcite deposition in a deep geological unit, the TSw, where the repository is located. Uncertainty in the infiltrating water composition near the surface is, thus, insignificant because calcite reaches saturation well above this unit. In addition, the constant infiltration rate and steady-state water flow conditions over geological time used in the simulations are also justified by evidence that the rate of calcite growth in the unsaturated zone has remained approximately constant over at least the past 8 million years (Paces et al. 1998 [DIRS 107408]).

The primary driving force for calcite precipitation from percolating waters in the unsaturated zone is its decreasing solubility with increasing temperature; calcite precipitates as water flows downward because of the geothermal gradient. Therefore, consideration of the ambient geothermal gradient is very important for calcite precipitation. The temperature distribution is a function of the crustal heat flow and the effect of infiltration. The modeled temperature

distributions in borehole WT-24 are discussed later in Section 7.7.5.2. Pore waters extracted from Yucca Mountain rock matrix collected from deep locations are close to equilibrium with respect to calcite (BSC 2004 [DIRS 169734], Section 7.7.1), and no measurements of aqueous concentrations are available from fractures because they generally have low liquid saturations.

The calcium concentration and CO_2 partial pressure in percolating water is a major factor controlling the abundances of calcite and its stability. This is a result of the decreasing solubility of CO_2 gas in water with increasing temperature, which in turn causes the following degassing process: $HCO_3^- + H^+ \rightarrow CO_2$ (g) + H_2O. Gaseous CO_2 is also redistributed by gas-phase diffusive transport. Degassing increases the pH, and then contributes to calcite precipitation: $Ca^{2+} + HCO_3^- \rightarrow CaCO_3$ (calcite) + H^+. Water and gas flow between fractures and the adjacent matrix governs the resulting calcite distribution within each medium. Calcite precipitation is also affected by other factors, such as the dissolution and precipitation of aluminosilicate minerals (mainly through modifying the pH and the CO_2 partial pressure).

7.7.3 Reactive-Transport Model

Modeling of calcite deposition in the Yucca Mountain unsaturated zone was performed using the reactive transport computer code TOUGHREACT (Xu and Pruess 1998 [DIRS 117170]; 2001 [DIRS 156280]). (This version of the code has not been qualified under LP-SI.11Q-BSC, *Software* Management, but its use for corroboration is appropriate). The code uses a sequential iteration approach similar to the report by Yeh and Tripathi (1991 [DIRS 162125]), Walter et al. (1994 [DIRS 162122]), and Xu et al. (1999 [DIRS 162123]), which solves the transport and reaction equations separately. Flow and transport are based on space discretization by means of integral finite differences. An implicit time-weighting scheme is used for individual components of the model: flow, transport, and kinetic geochemical reaction. The chemical transport equations are solved independently for each component, whereas the reaction equations are solved on a gridblock basis using Newton-Raphson iteration. Full details of the code are given in reports by Xu and Pruess (1998 [DIRS 117170]; 2001 [DIRS 156280]).

In the model, advective and diffusive transport of aqueous chemical species is considered in the liquid phase. Molecular diffusive transport of gaseous species (CO_2) is considered in the gas phase. Aqueous chemical complexation and gas dissolution/exsolution are accounted for under local equilibrium, whereas mineral dissolution/precipitation can proceed at equilibrium and/or can be kinetically controlled. Gas species in the chemical computations are assumed to behave as ideal gases (i.e., fugacity equals partial pressure). Temperature effects are considered for geochemical reaction calculations, because equilibrium and kinetic data are functions of temperature.

Changes in porosity and permeability from mineral dissolution and precipitation on water flow are not considered for the present modeling. In fact, these changes are very small. Figure 7.7-3 shows that observed calcite precipitation in TSw unit is less than 1%. These effects have not appeared to close up any fracture in the deep system. By neglecting porosity and permeability change, modelers obtain quasi-steady flow conditions. This makes it possible to consider geochemistry in great detail for a simulation period of 10 million years.

A dual permeability approach, in which fractures and matrix are treated as two separate continua, was employed for water flow and chemical transport in the unsaturated fractured tuff. In this approach, interflow (water and chemicals) is allowed between fractures and the adjacent matrix, and global flow occurs within both fracture and matrix continua. The AFM developed by Liu et al. (1998 [DIRS 105729]) was used to describe fracture–matrix interaction and preferential liquid flow in fractures.

7.7.4 Hydrogeological and Geochemical Conditions

7.7.4.1 Hydrogeological Conditions

As discussed in the geological model of Section 6.1, the Yucca Mountain unsaturated zone consists of layers of welded and nonwelded volcanic tuffs. The welded and nonwelded tuffs have vastly different hydrological properties. Welded units are characterized by relatively low porosity, low matrix permeability, and high fracture density, whereas the nonwelded tuffs have higher matrix porosity and permeability, and lower fracture density (Liu et al. 1998 [DIRS 105729]). Montazer and Wilson (1984 [DIRS 100161]) developed a conceptual model for the Yucca Mountain unsaturated zone that identified five main hydrogeological units based on the degree of welding and on the associated relationships to fracture intensity. This model has formed the basis for modeling flow in the Yucca Mountain UZ. Table 7.7-1 describes three of the five units, each of which is further divided into a number of model layers with different hydrogeological and geochemical properties (SNL 2007 [DIRS 179545]; SNL 2007 [DIRS 177404]). The CHn unit is comprised of zeolitic and vitric nonwelded tuffs underlying the basal vitrophyre of the Topopah Spring Tuff. Below the CHn are the Crater Flat undifferentiated units, consisting of the lower Bullfrog and Tram Tuffs of the Crater Flat Group. The hydrogeological units below the TSw were not considered in geochemical transport simulations, so details regarding these units are not given in Table 7.7-1. The primary interest is in calcite deposition within the TSw unit, where the repository is located (tsw4 and tsw5 model layers in Table 7.7-1). The exclusion of the underlying hydrogeological units does not affect the results in the TSw unit because flow is predominantly gravity driven, and upward chemical diffusion is subordinate to downward advective transport. Note also that the previous set of porosity and permeability values (Table 7.7-1) used in calcite modeling are different from the current flow model. As mentioned before, a one-dimensional steady-state flow field was used for the calcite modeling—the amount of calcite precipitation mainly depends on infiltration rate and then the percolation flux. Therefore, effects of different porosity and permeability on calcite precipitation in TSw should be small.

Table 7.7-1. Hydrogeologic Units, Model Layers, and Hydrogeological Properties for the Yucca Mountain UZ Flow and Transport Model, as Given by the Calibrated Properties Model

Hydrogeologic Unit	Description	Model Layer	Fracture		Matrix	
			Permeability (m^2)	Porosity	Permeability (m^2)	Porosity
TCw: Tiva Canyon Welded unit	Moderately to densely welded portions of the Tiva Canyon Tuff of the Paintbrush Group	tcw1	2.41×10^{-12}	3.7×10^{-2}	3.86×10^{-15}	0.253
		tcw2	1.00×10^{-10}	2.6×10^{-2}	2.74×10^{-19}	0.082
		tcw3	5.42×10^{-12}	1.9×10^{-2}	9.23×10^{-17}	0.203

Table 7.7-1. Hydrogeologic Units, Model Layers, and Hydrogeological Properties for the Yucca Mountain UZ Flow and Transport Model, as Given by the Calibrated Properties Model (Continued)

Hydrogeologic Unit	Description	Model Layer	Fracture		Matrix	
			Permeability (m^2)	Porosity	Permeability (m^2)	Porosity
PTn: Paintbrush Nonwelded unit	Variably welded Paintbrush Tuff and its associated bedded tuffs, including those located at the bottom of the Tiva Canyon and top of the Topopah Spring Tuffs	ptn1	1.86×10^{-12}	1.4×10^{-2}	9.90×10^{-13}	0.387
		ptn2	2.00×10^{-11}	1.5×10^{-2}	2.65×10^{-12}	0.439
		ptn3	2.60×10^{-13}	3.2×10^{-3}	1.23×10^{-13}	0.254
		ptn4	4.67×10^{-13}	1.5×10^{-2}	7.86×10^{-14}	0.411
		ptn5	7.03×10^{-13}	7.9×10^{-3}	7.00×10^{-14}	0.499
		ptn6	4.44×10^{-13}	4.6×10^{-3}	2.21×10^{-13}	0.492

7.7.6 Concluding Remarks

Modeling calcite deposition provides additional evidence for validation of the UZ model. For the mean infiltration rate (2–5.92 mm/yr), simulations in Figure 7.7-3 are within the range of data for each unit (except at the PTn-TSw contact) for the more realistic extended-case geochemical system. The contact between the two units is where lateral flow may occur, which is not included in the one-dimensional model. The comparison in Figure 7.7-3 indicates that the validation criterion is met. This is because the acceptance criterion is applied only to the mean infiltration rate, which s the expected rate, and the other rates, representing extremes, would not be expected to simulate actual mean behavior. In addition, the validation is focused on the extended-case geochemical system. The excursion in the model results at the PTn-TSw contact is not important because it is an artifact of the lack of lateral flow in the one-dimensional model and would not occur in the three-dimensional UZ flow model.

Over a range of 2 to 20 mm/yr infiltration rates, the simulated calcite abundances generally fall within the range of calcite observed in the field, which satisfies the validation criterion. The simulated calcite distributions capture the USGS–measured data from the WT-24 well cuttings (DTN: GS021008315215.007 [DIRS 162127]). The 20-mm/yr infiltration rate may be the upper bound for WT-24 location, whereas the infiltration rate (2 to 5.92 mm/yr) used for the flow model gives the closest match to the data. The observed calcite precipitation for the top of TSw occurs mostly in the fractures, which is also captured. The modeling results can provide useful insight into process mechanisms such as fracture–matrix interaction, as well as conditions and parameters controlling calcite deposition. The modeled calcite abundances generally increase with increasing infiltration rate, but become less sensitive to infiltration at higher rates as a result of changes to the geothermal gradient. Therefore, between a 5.92 and 20 mm/yr infiltration rate, the amount of calcite increases only slightly in the TSw.

The calcite measurements may provide insight into the long-term average infiltration over the lifetime of Yucca Mountain. The findings imply that perhaps lower rates are more consistent with calcite data. That is, glacial transition values in the 2 to 6 mm/yr range, with correspondingly lower present-day values, are consistent with these data. This information suggests lower long-term average rates for the site.

One-dimensional simulation is appropriate because both flow and geothermal gradient are primarily vertical. The current observed calcite is formed cumulatively over about 10 million years. A number of uncertainties are involved in the numerical simulation results, the most influential of which are variations in geothermal gradient and infiltration over time. Differences between one-dimensional and three-dimensional flow are much less than the differences in geothermal gradient and infiltration over 10 million years. Agreement between simulated and measured calcite abundance could work to establish the validity of the flow field and infiltration rates used in the UZ flow model. No significant lateral flow (above TSw and within the TSw unit) was predicted in both the previous flow model and current flow model at the WT-24 location. Therefore, the calcite analysis conclusion based on the previous flow model is still valid for the current flow model.

Finally, in reply to a commentary paper by Dublyansky and Smirnov (2005 [DIRS 180650]), Sonnenthal et al. (2005 [DIRS 180639]) preformed a simulation with variable bottom boundary temperatures approximating those measured in fluid inclusions. The results of this simulation show slightly greater abundances of calcite compared to the ambient temperature simulation, yet show similar trends with depth. The new results are within the spread of the measured calcite abundances, and therefore the variable geothermal gradient did not change the conclusions of the first paper. Thus, the results with variable temperature boundary do not change the conclusions made above.

7.8 MODELING ANALYSIS OF ALCOVE 8/NICHE 3 FAULT TESTS

This section simulates in situ field tests of artificial infiltration along a fault at Alcove 8/Niche 3. The fault tests caused localized saturated conditions below the test spot in an otherwise UZ. Under this field condition, test data are compared to results of simulations using the same conceptual model, methodology, and modeling approach as those used in the UZ flow model. This modeling activity presents a different case of validation for the UZ flow model. The results will build confidence in the UZ flow model from a different perspective (in terms of different-scale model results and field conditions).

This modeling analysis uses both model calibration and prediction. Comparisons between simulated and observed data are useful for evaluating the validity of the methodology used in the UZ flow model for capturing UZ flow and transport processes. The criterion for validation is that the predicted results for the time required for a conservative tracer to reach a given concentration (e.g., peak concentration) are within a factor of five of the observed time. As demonstrated in Section 7.8.3.2 below (the discussion of modeling results), the criterion is met. This modeling activity is adopted from the previous version of *UZ Flow Models and Submodels* (BSC 2004 [DIRS 169861], Section 7.6).

7.8.1 Field Observations

Infiltration rate, seepage rate, and tracer concentration data from the fault test are used to corroborate model simulations. The fault test used water and two liquid tracers. The test was carried out in the upper lithophysal and middle nonlithophysal subunits in the Yucca Mountain UZ. These geological subunits correspond to model layers tsw33 and tsw34, respectively, in the UZ model. The tsw33 has some lithophysal cavities that may intersect fractures. Liquid water, first without and then with tracers, was released at the floor of an alcove along the fault (about 5 m long (DTN: GS020508312242.001 [DIRS 162129]) within tsw33. Seepage from the fault into a niche and tracer concentrations of seeping liquid were monitored as functions of time. The niche is located within tsw34, about 20 m below the floor of the alcove; the interface between tsw33 and tsw34 is about 15 m below the floor of the alcove (DTN: LB0301N3SURDAT.001 [DIRS 162130]).

A pressure head of 2 cm was maintained at the infiltration plot along the fault at the alcove. The plot consists of four trenches that have different infiltration rates as a result of subsurface heterogeneity along the fault. Figure 7.8-1 shows the total infiltration rate as a function of time (DTNs: GS020508312242.001 [DIRS 162129] and GS020908312242.002 [DIRS 162141]). For simplicity, this model considers the uniformly distributed infiltration rate along the infiltration

plot to be consistent with the uniform property distribution in the UZ model. One consideration in the modeling study is to evaluate approaches used in the site-scale model. Considerable

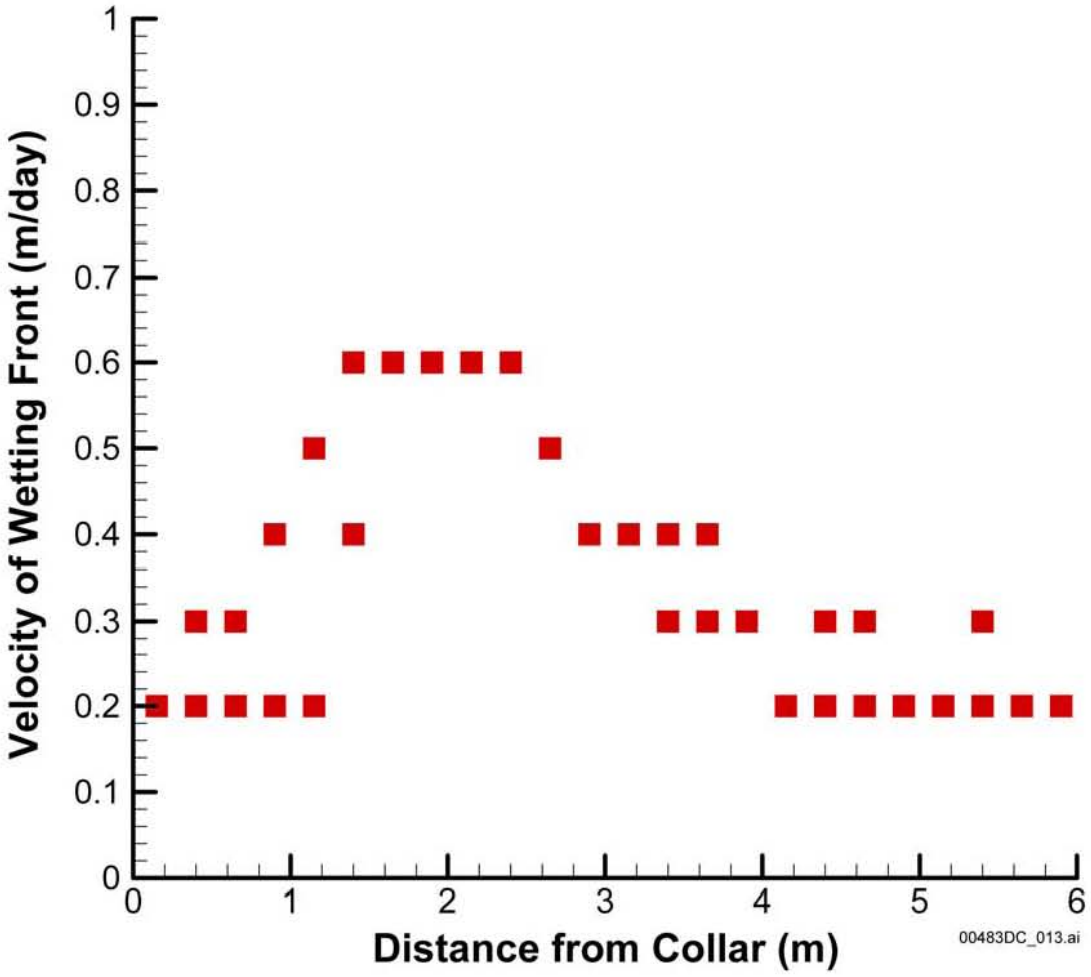

Source: DTN: LB0303A8N3LIQR.001 [DIRS 162570].

NOTE: Observation boreholes are approximately perpendicular to the fault. The distance from a borehole collar to the fault is about 2 m.

Figure 7.8-3. Water Travel Velocity Data for Boreholes 9 and 10

After 209 days, two tracers with different molecular diffusion coefficients, bromine and pentafluorobenzoic acid, were introduced into infiltrating water at the infiltration plot. Tracer concentrations in three of the trays (at the niche) capturing seeping water from the fault were measured (DTN: LB0303A8N3LIQR.001 [DIRS 162570]). Seepage rates corresponding to these three trays were not measured during the period of tracer concentration measurement. In this study, a flux-averaged breakthrough curve (concentration as a function of time) from these trays was used to represent the average breakthrough curve for all trays at the niche where seepage was captured. A constant flux value for each of the three trays was used for calculating the flux-averaged breakthrough curve shown in Figure 7.8-4. The constant flux values for the three trays were determined as the averaged value over 56 days before tracers were introduced. This flux-averaged breakthrough curve was compared with simulation results.

(1980 [DIRS 100610]) parameters (for matrix, fractures, and the fault), and the parameter of the AFM, γ, for fractures (DTNs: LB997141233129.001 [DIRS 104055]; LB980901233124.101 [DIRS 136593]; LB990861233129.001 [DIRS 110226]; and LB990501233129.001 [DIRS 106787]). Because fracture van Genuchten parameters for tsw33 and tsw34 are similar (Table 7.8.1), a simple average of these parameters was used as the corresponding parameters for the fault. The averaged k/ϕ (where k is fracture permeability and ϕ is the corresponding fracture porosity) was calculated as fault permeability. Note that because there is no matrix in the fault in the model (or $\phi = 1$), the weighted k/ϕ (rather than weighted k) is employed for estimating fault permeability. The aperture of the fault was estimated as the average of fracture apertures of the two subunits. Note that the AFM was developed for fracture networks rather than for a single fracture. Consequently, the AFM does not apply to the fault here. In fact, most of the parameter values mentioned above and given in Table 7.8-1 are not site specific for the fault test site. These values were used as initial guesses for model calibration against the seepage rate and water-travel-velocity data observed from the fault test. Note that not all site-specific parameters are available and the initial guess of some values were necessary. This is because the initial guess does not significantly affect the final calibrated values. To reduce the number of variables in model calibration (or inverse modeling), parameters expected to significantly affect simulated tracer transport time and seepage rate were varied in the calibration, while other parameters were kept unchanged. The varied parameters were fracture and fault permeabilities, fracture porosity, fault aperture, and fracture and fault van Genuchten α values.

Table 7.8-1. Uncalibrated Rock Properties

Rock property	Fault [e]	tsw33		tsw34	
		Fracture	Matrix	Fracture	Matrix
Permeability (m^2)	4.34×10^{-11}	5.5×10^{-13} [c]	3.08×10^{-17} [a]	0.35×10^{-13}	4.07×10^{-18} [a]
Porosity	1.00	6.6×10^{-3} [d]	0.154 [a]	10^{-2} [d]	0.11 [a]
Fracture frequency (m^{-1})		1.03 [e]		1.5 [e]	
Fracture aperture (m)	1.12×10^{-3}	1.49×10^{-3} [e]		1.14×10^{-3} [e]	
Active fracture model parameter γ	0.0	0.41 [a]		0.41 [a]	
van Genuchten α (Pa^{-1})	1.0×10^{-3}	11.46×10^{-3} [a]	2.13×10^{-5} [a]	5.16×10^{-4} [a]	3.86×10^{-6} [a]
van Genuchten m	0.608	0.608 [a]	0.298 [a]	0.608 [a]	0.291 [a]

Sources: [a] DTN: LB997141233129.001 [DIRS 104055].
[b] DTN: LB980901233124.101 [DIRS 136593].
[c] DTN: LB990861233129.001 [DIRS 110226].
[d] DTN: LB990501233129.001 [DIRS 106787].
[e] BSC 2004 [DIRS 169861], Table 7.6-1.

Infiltration-seepage processes in the fault and the surrounding fractured rock were determined by several mechanisms. Liquid water applied at the alcove floor (Figure 7.8-5) flowed first into the fault and then into fractured networks connected to the fault. Matrix imbibition occurred at interfaces between fractures and the matrix, and between the fault and the matrix. When water arrived at the intersection between the fault and the niche, it might not have immediately seeped into the niche until the capillary pressure became zero because of capillary barrier effects (Philip et al. 1989 [DIRS 105743]; Birkholzer et al. 1999 [DIRS 105170]). Such effects can divert flow away from the opening, resulting in only a portion of the water arriving at the niche ceiling actually seeping into the niche. Tracer transport time was determined by fracture porosity, fault aperture, and the matrix imbibition process.

fracture porosity of tsw33 (Table 7.8-3). While the actual width of the fault zone is unknown, the estimated equivalent fault aperture (3 cm) is used. The estimated fracture porosity is consistent with those estimated from water release tests performed in the same geological unit (BSC 2004 [DIRS 170004], Section 6.11.3.2).

Table 7.8-3. Rock Properties Calibrated from Both Seepage Rate and Water Travel Velocity Data (Run #2)

Rock property	Fault	tsw33	tsw34
Fracture Permeability (m^2)	1.12×10^{-10}	1.23×10^{-12}	5.01×10^{-13}
Fracture Porosity		0.066	
Fracture aperture (m)	0.03		
Fracture van Genuchten α (Pa^{-1})	1.24×10^{-3}	2.19×10^{-3}	1.09×10^{-3}

Source: Output DTN: LB0303A8N3MDLG.001 [DIRS 162773], file *Irun4Ni.par*.

NOTE: All other rock properties are the same as those in Table 7.8.1. Rock names "tswF3", "NetF3," and "NetF4" in file *Irun1i.par* correspond to "Fault", "tsw33," and "tsw34", respectively, in this table.

Figure 7.8-7 shows a comparison among calculated water travel velocities from two calibration runs and the velocity data observed from the fault test. The simulated water travel velocities from Run #2 are much closer to the observed data than those from Run #1 (especially near the fault). However, the water travel velocities away from the fault are still overestimated. One possible explanation is that matrix imbibition from fractures above the niche were underestimated because the dual-continuum approach considerably underestimates the pressure gradient near a fracture matrix interface during transient flow conditions (Pruess and Narasimhan 1985 [DIRS 101707]). While this problem can be resolved with the MINC model of the report by Pruess and Narasimhan (1985 [DIRS 101707]), the computational intensity of the inverse model problem under consideration would be significantly increased. Note that a model calibration involves a great number of forward simulation runs. Considering (1) that the transient flow effects would be considerably reduced later in the test, and (2) that the focus here is on flow and transport within and near faults, simulated flow field and calibrated rock properties from Run #2 were used for simulating tracer transport at the test site. Figure 7.8-8 also shows a comparison between simulated seepage rates as a function of time (Run #2) and field observations. The match is reasonable. Figure 7.8-8 matches both wetting-front velocity and seepage-rate, and it is, therefore, considered a better calibration than Figure 7.8-6, which only matches the seepage rate data. Note that to give a reasonable prediction of solute transport, the water flow must be correctly modeled.

8.7 TRACER TRANSPORT TIMES

A total of 32 tracer transport simulations were carried out to obtain insight into the impacts of infiltration rates, UZ flow model conceptual models, and retardation effects on tracer migration from the repository to the water table (Section 6.7). The 16 UZ flow fields were incorporated into these 32 transport runs. For each flow field, there were two tracer transport runs, one for conservative (or nonadsorbing) and the other for reactive (or adsorbing) tracer transport, with tracer release from repository fracture blocks. These tracer-transport studies indicate that there exists a wide range of tracer transport times associated with different infiltration rates and the type of tracers. The most important factors for tracer-transport times are found to be: (1) surface net infiltration rates, and (2) adsorption effects.

Statistics of tracer transport times at 10% and 50% mass breakthrough at the water table from the 32 simulations show that tracer-transport times vary inversely to the average surface infiltration (net water recharge) rate over the model domain. When the average infiltration rate increases from 3 to 70 mm/yr, average tracer transport (50% mass breakthrough) times decrease by more than two orders of magnitude for adsorbing and nonadsorbing species. Nonadsorbing tracers migrate (from the repository to the water table) one to two orders of magnitude faster than an adsorbing tracer under the same infiltration condition.

8.8 UZ FLOW WEIGHTING FACTORS

A generalized likelihood uncertainty estimation (GLUE) methodology was used to determine the weighting factors (Section 6.8). The generation of the UZ flow weighting factors accounts for prior information available from the infiltration model for the probability of infiltration maps, as well as matches between UZ flow model results (distributions of temperature and chloride concentration) and corresponding field data. Such weighting factors were derived from infiltration and UZ flow model results for present-day conditions.

8.9 ANALYZING TRANSIENT-PULSE INFILTRATION

How episodic surface infiltration affects deep percolation was investigated by examining variations in percolation fluxes at the bottom of the PTn versus time, using two one-dimensional column models (Section 6.9). Results from the two column models show that surface infiltration pulses can be effectively smoothed temporally once traveling to the bottom of the PTn unit. In general, after rapid changes during the first several hundred years of pulse infiltration, the percolation fluxes at the bottom of the PTn gradually approach the average value of net infiltration.

8.10 MODEL VALIDATION

Model validation efforts have been documented in this report (Section 7). Validation activities for the UZ flow model mainly include corroboration with experimental data and modeling studies, using the following corroboration with experimental data: (1) ECRB observation data; (2) WT-24 perched water data; (3) gas flow data from boreholes SD-12 and UZ-7a; and (4) borehole-measured ^{14}C data and Alcove 8—Niche 3 flow and transport data. In addition, validation efforts are also made for the strontium model and calcite model, using field-observed data from surface-based boreholes or from the ESF.

In these validation examples, the simulation results of the UZ flow model and submodels are shown to be able to match different types of available observation data, such as water potentials, perched water locations, tracer and geochemical concentrations, and pneumatic pressures. The criteria of the model validation of the TWP (BSC 2006 [DIRS 177465]) are, in general, satisfied. These efforts have provided validation of the UZ flow model and its submodels for their accuracy and reliability in describing hydrological, thermal, and chemical conditions, and predicting flow and transport processes in the unsaturated zone system of Yucca Mountain.

8.11 LIMITATIONS

The UZ flow model and submodels are appropriate tools for characterizing flow and transport processes in the Yucca Mountain unsaturated zone. The accuracy and reliability of the UZ flow model predictions are dependent on the accuracy of estimated model properties, other types of input data, and hydrogeological conceptual models. These models are limited mainly by the current understanding of Yucca Mountain system, including the geological and conceptual models, the volume-average modeling approach, and the available field and laboratory data.

Past site investigations have shown that large variabilities exists in the flow and transport parameters over the spatial and temporal scales of the mountain. Even though considerable progress has been made in this area, uncertainty associated with the UZ flow model input parameters exists. The major uncertainties in the UZ model parameters are: (1) the accuracy of estimated current, past, and future net infiltration rates over the mountain; (2) quantitative descriptions of the heterogeneity of welded and nonwelded tuffs, their flow properties, and detailed spatial distributions within Yucca Mountain, especially below the repository; (3) fracture properties in zeolitic units and faults from field studies; (4) evidence of lateral diversion caused by zeolites in the CHn units and within the PTn units; and (5) transport properties (e.g., adsorption or K_d coefficients in different rock types, matrix molecular diffusion coefficients in different units for different radionuclides, dispersivities in fracture and matrix systems). These uncertainties exist, but they have been addressed with the modeling studies in this report. In particular, most uncertainties are captured within the range of flow fields generated.

8.12 HOW ACCEPTANCE CRITERIA ARE ADDRESSED

The following information describes how this analysis addresses the acceptance criteria in *Yucca Mountain Review Plan, Final Report* (NRC 2003 [DIRS 163274], Section 2.2.1.3.6.3). Only those acceptance criteria that are applicable to this report (Section 4.2) are discussed. In most cases, the applicable acceptance criteria are not addressed solely by this report; rather, the acceptance criteria are fully addressed when this report is considered in conjunction with other analysis and model reports that describe flow in the unsaturated zone. Where a subcriterion includes several components, only some of those components may be addressed. How these components are addressed is summarized below.

To examine these relationships more closely, cumulative distributions from the previous and current models, for percolation in the host rock within the repository footprint, are compared in Figures H-1 through H-3 for the present-day, monsoon, and glacial transition climate states. Percolation flux in the host rock is a result from the UZ flow model and is selected for comparison here (rather than net infiltration at the ground surface) because it is used directly as a boundary condition for drift-scale coupled process models (e.g., multiscale model) and for the drift seepage abstraction in TSPA. In addition, percolation flux at the repository horizon is an important determinant of radionuclide mobility in the UZ transport abstraction.

These percolation data were developed by sorting the percolation flux values at the repository horizon in the 560 columns of the UZ flow model grid for both the previous (INFIL based; BSC 2004 [DIRS 170007]) and current (MASSIF based; SNL 2007 [DIRS 174294]) versions of the model. The 560 columns include the contingency area (SNL 2007 [DIRS 181383], Section 6.2.12[a]) that was not included in previous representations of the repository footprint. The distributions (Figures H-1 through H-3) preserve the full uncertainty and variability of the UZ flow model, and represent the same spatial domain.

Statistical approaches are used to compare the previous and current percolation fields (Tables H-2 and H-3): (1) compare mean values for the previous model, for the three climate states, with mean values for the current 10th, 30th, and 50th percentile fields (Table H-2); and (2) compare the ranges of spatial variation for the previous model with the same ranges for the current model (Table H-3). As noted above, the 90th percentile field from the current model is exceptional, but this field is assigned a relatively low weight in TSPA. A set of composite-weighted flux values is used for each climate state (Table H-2) that combines the averages of 10th, 30th, 50th, and 90th percentile fields from the current model, using the same sampling weights used in TSPA. These weights are combined in Table H-2 with flux values from different sources (as indicated) to develop composite-weighted values for the present-day, monsoon, and glacial transition climate states that can be readily compared to supplement the impact evaluation for Group 3 products. These modal values reasonably represent flux conditions likely to be assigned in TSPA to particular waste package locations in the repository. They are useful for evaluating the sensitivity of near-field behaviors such as thermally driven coupled processes, that do not depend on the far-field distribution of percolation flux.

For the previous model (BSC 2004, [DIRS 170007]), the overall spatial variation of percolation flux at the repository horizon within the repository footprint ranged from zero (discounting small negative values) to 294 mm/yr, whereas the current model (SNL 2007 [DIRS 174294]) ranges from 0.15 to 136 mm/yr (Table H-3). Current data for the 10th, 30th, and 50th percentile fields are mostly encompassed by the previous data for the “low” and “high” uncertainty states. Extreme values from the previous data (>95th percentile for the Mean and High uncertainty states) bracket all the current data (including the 90th percentile field). While these comparisons are only statistical, they show that application of the current values in TSPA falls mostly within the range of uncertainty and variability that existed when the Group 2 and Group 3 products were developed.

An important aspect of Figures H-1 through H-3 is that the differences between previous and current model results, for the comparisons described above, are typically smaller than the differences between the uncertainty states for either the previous or current data (Table H-3).

Table H-2. Average Flux Values for Comparison of Previous and Current Model Results

All fluxes in mm/yr	Present- Day	Monsoonal	Glacial-Transition	Weights	
Current Models for Infiltration and UZ Flow, Percolation Flux at PTn-TSw Interface					
Quantile	**Avg. Flux in Footprint [a]**				
0.1	4.1	7.8	12.2	0.6191	Weights: Table 6.8-1 of Section 6 (average values) Fluxes: SNL 2007 [DIRS 181383], Table 6.2-5[a].
0.3	10.2	16.1	26.3	0.1568	
0.5	14.6	19.5	36.2	0.1645	
0.9	34.1	92.4	69.7	0.0596	
Weighted	**8.6**	**16.1**	**21.8**	1.0000	
Previous Models for Infiltration and UZ Flow, Infiltration Flux at Ground Surface					
Case	**Avg. Flux in Footprint [a]**				
Lower	0.25	4.20	1.92	0.24	Fluxes and weights: BSC 2003 [DIRS 165991], Tables 6-4 and 6-7 (not including contingency area).
Mean	4.20	11.86	18.57	0.41	
Upper	10.80	19.53	35.23	0.35	
Weighted	**5.6**	**12.7**	**20.4**	1.00	
Previous Models for Infiltration and UZ Flow, Percolation Flux at PTn-TSw Interface					
Case	**Avg. Flux in Repository Footprint [a]**				
Lower	0.40	4.30	1.90	0.24	Fluxes: SNL 2007 [DIRS 181244], Table 6.6-11 Weights: BSC 2003 [DIRS 165991], Table 6-7
Mean	3.80	11.70	17.90	0.41	
Upper	11.10	20.30	35.10	0.35	
Weighted	**5.5**	**12.9**	**20.1**	1.00	
Drift-Scale Coupled Processes (DST and TH Seepage) Models (MDL-NBS-HS-000015 Rev. 02, Section 4.1.1.4)					
Values Used	6.0	16.0	25.0		Base values shown; model also includes sensitivity runs that multiply these values by factors of up to 100 (BSC 2005 [DIRS 172232], Section 6.2.1.4).
Drift-Scale THM Model (MDL-NBS-HS-000017 Rev. 01; Section 4.1.1.2)					
Values Used	6.0	16.0	25.0		
Mountain-Scale Coupled Processes (TH/THC/THM) Models (MDL-NBS-HS-000007 Rev. 03)					
Values Used	3.6	10.4	16.1	Average over three-dimensional TH model domain (Table 6.1-2)	
Values Used	5.8	17	28.8	Average over two-dimensional TH and THM model profiles (Section 6.1.4 and Table 6.5.6-1)	
Values Used	8.7	32.3	101.6	Average over segment of two-dimensional TH profile used for THC (Section 6.4.2.3)	
Ventilation Model and Analysis Report (ANL-EBS-MD-000030 Rev. 04, Section 6.9.1)					
Value Used	15.71	From mean flux field at location selected for sensitivity analysis.			

NOTE: [a] Refers to the 560-column footprint including the contingency area, for the previous and current data.